
The dynamics of starting gas-particle jets: a volcanic scenario

Valeria Cigala



München 2017

The dynamics of starting gas-particle jets: a volcanic scenario

Valeria Cigala

Dissertation zur Erlangung des Doktorgrades
an der Fakultät für Geowissenschaften
der Ludwig-Maximilians-Universität
München

vorgelegt von
Valeria Cigala
aus Gallarate, IT

München, 13. September 2017

Erstgutachter:	Prof. Dr. Donald B. Dingwell
Zweitgutachter:	Dr. Jacopo Taddeucci
Tag der mündlichen Prüfung:	20.12.2017

“Così adesso sono arrivato al mare.

Il mare.

Finisce, anche lui, come tutto il resto, ma vedete, anche qui è un po' come per i tramonti, il difficile è isolare l'idea, voglio dire, riassumere chilometri e chilometri di scogliere, rive, spiagge, in un'unica immagine, in un concetto che sia la fine del mare, qualcosa che si possa scrivere in poche righe...”

Alessandro Baricco

Kurzfassung

Explosive Vulkanausbrüche stellen eine reelle Bedrohung für einen signifikanten Prozentsatz der Weltbevölkerung sowie wichtige Infrastrukturanlagen dar. Während des Magmenaufstiegs entgasen volatile Phasen und bilden Blasen. In diesen kann sich ein hoher Überdruck aufbauen und stellt die treibende Kraft dar, die das Magma sehr effizient fragmentieren kann. Die der Fragmentation zu Grunde liegenden Mechanismen sind sehr komplex und mannigfaltig. Allen explosiven Ausbrüchen gemein ist, dass die potentielle Energie (Gasüberdruck in Blasen) bei der Magmenfragmentation nur zu einem Teil aufgebraucht wird. Die verbleibende Energie wird in kinetische Energie umgewandelt und führt zur Beschleunigung und Auswurf von Pyroklasten und Nebengesteinsbruchstücken in die Atmosphäre. Auswurfrate, Geschwindigkeit sowie Flugkurven dieser Partikel hängen stark von den anfänglich im Vulkan herrschenden Bedingungen ab, wie z.B. Magmenzusammensetzung, Gasüberdruck, Länge des Conduits, Geometrie des Vulkankraters etc.

Wenn möglich helfen direkte Beobachtungen an aktiven Vulkanen, die Art und Weise des Auswurfs von Pyroklasten zu beschreiben, um dadurch die „Startbedingungen“ des Ausbruchs einzugrenzen. Hochgeschwindigkeits- und Infrarotvideos des Auswurfs, seismische und akustische Aufnahmen sowie petrografische und geochemische Untersuchungen tragen dazu bei, explosive Ausbrüche besser zu verstehen. Es bleibt jedoch nach wie vor nur unter einer Reihe von Annahmen möglich, direkte Beobachtungen von explosive Vulkanausbrüchen und die zugrundeliegenden Rahmenbedingungen zu korrelieren und damit zu bestimmen. Aus diesem Zweck werden empirische Studien wie skalierte Laborexperimente herangezogen um Beobachtungen bekannten Rahmenbedingungen zuordnen zu können. Generell kann jedoch keine dieser Studien die natürliche Komplexität widerspiegeln. Die dadurch bestehende Vereinfachung erlaubt jedoch, den Einfluss einzelner Parameter auf das Verhalten isoliert zu betrachten sowie das eventuelle Wechselspiel festzustellen. Letztendlich hofft man, charakteristische Verhaltensmuster zu erkennen und zu quantifizieren und dadurch die zugrundeliegenden Bedingungen zu bestimmen. Außerdem können Laborstudien wichtige und in der Natur bis dato nicht bestimmbare Parameter ermitteln.

Im Rahmen der vorliegenden Arbeit habe ich schnelle Dekompressionsexperimente mit Lockerproben durchgeführt und damit „starting jets“ aus Gas und Partikeln erzeugt. Zu diesem Zweck verwendete ich zwei unterschiedliche experimentelle Apparaturen, die „Fragmentationsbombe“ an der LMU München sowie den „jet

burster“ am INGV in Rom, Italien. Dadurch war es mir möglich, den Einfluss der folgenden experimentellen Rahmenbedingungen auf das Auswurfverhalten zu ermitteln: 1) Kratergeometrie, 2) Conduitlänge, 3) Menge und Größe der Partikel, 4) Temperatur, und 5) Überdruck. Insbesondere untersuchte ich Partikelgeschwindigkeit und –flugbahn. Darüber hinaus konnte ich qualitative Aussagen zu Fragmentation, Auswurfrate und elektrischen Auf- sowie Entladungen treffen. Alle Experimente wurden mit einer Hochgeschwindigkeitskamera aufgezeichnet und erlaubte dadurch, die dynamischen Entwicklungen zu beschreiben. In den “jet buster” Experimenten wurden mit Hilfe von zusätzlich angebrachten piezoelektrischen Sensoren mikroseismische Signale aufgezeichnet und erlaubten dadurch eine Charakterisierung der Gasausbreitung.

Beide experimentellen Ansätze sind komplementär. Die Fragmentationsbombe besteht „im Kern“ aus einem metallischen Stoßrohr (24 cm lang), welches eine Kombination aus hohem Überdruck (bis 150 bar) und hoher Temperatur (bis 500°C) erlaubt. Die Partikel wurden in der Druckkammer, dem Stoßrohr, unter Überdruck gesetzt. Bei schneller Druckentlastung werden die Partikel aus dem Stoßrohr beschleunigt und am „Vent“ beobachtet. Der “jet buster” dagegen ist im Wesentlichen eine 3 m lange, transparente Plexiglasröhre (PMMA), die es zulässt, die Fortpflanzung von Gasdruckwellen zu beobachten. In diesem Fall betrug der Überdruck nicht mehr als 2 bar und die Probe ruhte anfänglich (bei atmosphärischen Bedingungen) auf einem feinen Metallgitter oberhalb der Druckkammer.

Experimente mit der Fragmentationsbombe zeigen unterschiedliche Korrelationen der PartikelAuswurfgeschwindigkeit mit den folgenden Rahmenbedingungen (Reihenfolge in abnehmender Wichtigkeit): 1) Conduitlänge (negativ); 2) Probenmenge (positiv); 3) Öffnungswinkel der Kratergeometrie (positiv, maximal für 15°; 4) Temperatur (positiv), und 5) Partikelgröße (negativ). Die zeitliche Entwicklung der PartikelAuswurfgeschwindigkeit ist immer nicht-linear und am stärksten beeinträchtigt von Probenmenge und Conduitlänge. Der maximale Öffnungswinkel des Gasjets (vor dem Auswurf der ersten Partikel) zeigt – in abnehmender Wichtigkeit – folgende Korrelation: 1) Öffnungswinkel der Kratergeometrie (negativ); 2) Temperatur (negativ); 3) Conduitlänge (positiv); 4) Probengröße (positiv), und 5) Probenmenge (negativ). Der Öffnungswinkel des anfänglichen Gasjets zeigt eine Kurvenform, die in Versuchen mit Aufbau “setup 1” am stärksten ausgeprägt ist, da in diesem Fall der zeitliche Unterschied zwischen Gasausstoß und dem Auswurf der ersten Partikel maximal ist. Dies ist der wichtigste beeinflussende Parameter. Der initiale Gasöffnungswinkel zeigte folgende Abhängigkeiten: 1) Probenmenge (positive), 2) Partikelgröße (negative); 3) Kratergeometrie (negative); 4) Conduitlänge

(positiv), und 5) Temperatur (negativ). Die zeitliche Veränderung des Öffnungswinkels des Gasjets ist stark von Probenmenge und Conduitlänge abhängig. Die Analyse der Videos lässt eine Bestimmung der zeitlich stark schwankenden Auswurfmengen (MER) zu. Der höchste gemessene Wert betrug 26kg/s für Experimente mit setup 2, 7 kg/s für setup 3 und 4.6 kg/s für setup 1. Diese zeitliche Abnahme korreliert mit der Abnahme der PartikelAuswurfgeschwindigkeit. Darüber hinaus konnten in vielen Experimenten mm- bis cm-lange Blitzentladungen beobachtet werden. Hier zeigte sich eine positive Korrelation mit Probenmenge sowie eine negative Korrelation mit Conduitlänge, Temperatur, Probengröße sowie Öffnungswinkel der Kratergeometrie.

Im "jet buster" habe ich Experimente mit und ohne Partikel durchgeführt. Dadurch konnte ich die elastische Reaktion des Gesamtsystems der Jetdynamik gegenüberstellen. In Experimenten „ohne Partikel“ wurde durch die Zugabe einer Mindermenge von Kaolinpulver erreicht, dass die Gasdruckwelle sichtbar wurde. Die anfänglich bis zu 500 m/s schnelle Gasdruckwelle verlangsamte sich am oberen Ende der Röhre auf 150 m/s, begleitet von der Ausbildung eines Vortexrings. Die beschleunigten Partikel erreichten ihre maximale Geschwindigkeit in einer Höhe von 40 und 100 cm oberhalb ihrer Startposition. Wie in der Fragmentationsbombe so zeigt sich auch hier eine negative Korrelation von maximaler Austrittsgeschwindigkeit und Partikelgröße und die zeitliche Entwicklung der maximalen Austrittsgeschwindigkeit zeigt einen nicht-linearen Verlauf. Die mikroseismischen Signale erlauben eine überzeugende Korrelation mit den visuellen Phänomenen.

Ein Vergleich natürlicher Vulkanausbrüche (im vorliegenden Fall am Vulkan Stromboli in Italien aufgezeichnet) mit empirisch gewonnenen Erkenntnissen der Laborexperimente ist keineswegs trivial. Wie bereits angesprochen spielen sich während natürlicher Vulkanausbrüche Wechselwirkungen zwischen viel mehr Prozessen ab als experimentell in Rahmen dieser Arbeit untersucht werden konnten. Nichtsdestotrotz stellen die im Rahmen dieser Arbeit gewonnen Erkenntnisse einen signifikanten Wissensmehrwert dar, der in numerische Modelle eingebunden eine wichtige Rolle in der Gefahrenabschätzung von explosiven Vulkanausbrüchen darstellen wird.

Abstract

Explosive volcanic eruptions are a threat for a large part of global population and infrastructures. Explosive eruptions are the results of energetic magma fragmentation, where only gas exsolved in the magma drive the eruption, or of the interaction with external water. The mechanisms of fragmentation are complex and various, but despite that at explosive eruption onset the potential energy stored in gas bubbles in the magma always transforms into kinetic energy via gas expansion and produce the ejection of pyroclasts and/or non-juvenile material in the atmosphere. Particle ejection rate, velocity and trajectory differ depending on source conditions, e.g. magma composition, gas overpressure, conduit length, vent geometry, etc.

Field observations, when possible, can help to characterize an ejection from which then the source conditions are indirectly retrieved. High-speed and infrared videos of volcanic ejections, seismic and acoustic measurements, as well as petrographical and geochemical analysis on the pyroclasts ejected offer insight on the eruptive event. Nevertheless, to link observations and source parameters is not trivial and it still requires a certain number of assumptions. Therefore, the knowledge of source conditions stays uncertain. On the other hand, empirical studies can help linking observations and input parameters, since the latter are chosen experimental conditions. In general, laboratory experiments are far less complex than natural eruptions. However, the simplifications imposed benefit the investigation of single processes as well as the understanding of the effects of boundary conditions on such observed dynamics. The goal, at the end, is to learn the patterns of certain dynamics and possibly, to recognize certain characteristics of volcanic eruptions and be able to associate them to source conditions. Additionally, empirical results provide input parameters for numerical modelling and thus hazard assessment.

I perform rapid decompression experiments of gas-particle mixtures generating starting jets. I use two different experimental apparatus, the first is the “fragmentation bomb” at the LMU facility and the second the “jet buster” at INGV Rome. With the two setups, it is possible to characterize the effect of boundary conditions such as: 1) vent geometry, 2) tube length, 3) particle load and size, 4) temperature, and 5) overpressure in the reservoir on the dynamics of the ejection of natural particles of different initial size distribution (from 0.125 to 4 mm). In particular, I focus the analysis on particle velocity and trajectory. Observations on particle fragmentation, mass ejection rate and lightning generation are also possible on experiments from the

“fragmentation bomb”. The experiments are recorded with a high-speed camera, which provides visual observation of the dynamics. On the “jet buster” experiments, the video recordings are coupled with piezoelectric sensors providing microseismic signals of the related propagation dynamics. The two apparatus are different and complementary. The “fragmentation bomb”, a shock-tube made of metal, is 24 cm long, allows high overpressures (here 150 bar) and temperatures (here 500°C), gas and particles are pressurized in the same chamber and the observations are made at vent exit. The “jet buster”, on the other hand, with its 3 m of transparent PMMA tube allows the observation of the whole propagation and dynamics inside the pipe as well at vent exit. The overpressure threshold is in the order of few bar (here 2 bar), and the gas reservoir is separated and below the sample chamber.

In the “fragmentation bomb” experiments, maximum particle velocity shows, in order of importance, 1) negative correlation with tube length; 2) positive correlation with particle load; 3) positive correlation with flaring vent walls, with peaks for funnel 15; 4) positive correlation with temperature, and 5) negative correlation with particle size. The evolution of particle velocity with time is non-linear and is mostly affected by particle load and tube length. Gas maximum initial spreading angle shows, in order of importance: 1) negative correlation with flaring vent walls; 2) negative correlation with experimental temperature; 3) positive correlation with tube length; 4) positive correlation with particle size, and 5) negative correlation with particle load. The gas spreading angle evolution with time shows a bell shape pattern and it is especially appreciable in setup 1 experiments, due to the particles later arrival. This is the main affecting parameter. The particle initial spreading angle shows: 1) positive correlation with particle load, 2) negative correlation with particle size; 3) negative correlation with vent geometry; 4) positive correlation with tube length, and 5) negative correlation with temperature. The particle spreading angle evolution with time shows patterns varying in particular with particle load and tube length.

Estimations of the mass ejection rate (MER) and instantaneous mass or particle concentration show peaks of 26kg/s for setup 2 experiments, 7 kg/s for setup 3 and 4.6 kg/s for setup 1. The evolution of the MER with time reflects the evolution of particle velocity with time. Finally, mm to cm electrical discharges, i.e. lightning, are observed. Their appearance is positively correlated with particle load, and negatively correlated with tube length, temperature, particle size, and flaring of vent walls.

In the “jet buster”, I perform both gas only and gas-particle mixture experiments. This to compare the elastic response of the system and jets’ dynamics. The gas only experiments includes a pinch of kaolin powder in order to make the flow front propagation visible in the camera. The gas flow front shows an initial fast propagation

(up to 500m/s) in the pipe accompanied by an abrupt deceleration (to 150 m/s) at vent exit where it generates a vortex ring. On the other hand, particles show maximum velocities between 40 to 100 cm in the pipe in respect to initial sample position. In addition, in this case, maximum particle velocity shows negative correlation with particle size and the evolution of particle velocity displays a non-linear trend. Good correlation between microseismic signals and process occurring in the pipe is observed.

The comparison of the experimental results with natural data collected on Stromboli volcano, Italy, is far from trivial. As mentioned above, volcanic eruptions are characterized by the interaction of several processes, thus making them far more complex. Nevertheless, I think the data set present here provides a promising link for both field volcanology (visual observations and quantitative monitoring) as well as numerical modelling in order to advance our understanding of explosive volcanic eruptions and assess the related hazard.

Preamble

Part of the content of Chapter 2 and Chapter 3 (sections 3.1, 3.2, 3.3 and 3.5) of this doctoral dissertation is published in a scientific peer reviewed journal. Possible applied changes did not modify the conclusions reported in the paper, but served to adapt the original format to the thesis layout and format. The full reference of the published paper is the following:

Cigala V., U. Kueppers, J. J. Peña Fernández, J. Taddeucci, J. Sesterhenn, and D. B. Dingwell (2017), The dynamics of volcanic jets: Temporal evolution of particles exit velocity from shock-tube experiments, *J. Geophys. Res. Solid Earth*, 122, doi:10.1002/2017JB014149.

Acknowledgments

Firstly, I would sincerely like to thank you, Ulli, for being my mentor for the past three years and some months. Thank you for all the positive support provided, for the opportunities given, for the advice and for expressing your opinion, but always respecting my own opinion and choices. For the thrust and freedom granted to conduct the project. It was a pleasure for me to work with you and I learned a lot from you. Thank you, Don, for always being available when needed and for providing support when asked. Thank you, Jacopo, for being a great mentor as well. You always provide great support and clever scientific discussion. I always like to hear and discuss ideas with you. Thanks, also, for all the great Stromboli campaigns (when do we fly the rocket in the plume?). Thanks also to Jörn, for the help with existential fluid dynamics questions and giving a different point of view in all discussions.

Then, I would also like to thank Alejandra for the support given me and for the work done together. I feel I have a lot to learn from you. In addition, I would like to thank Corrado, for granting me overnights in front of Sakurajima, and Betty for always giving me a clever suggestion or a good idea.

A big thank you goes to my PhD fellows and colleagues at LMU, past and present: Basti, Matt, Pancho, Jenny, Lukas, Damien, Cri, Leti, Klaus, Ana, Danilo, Tim, Sid, Kai, Fabian, Jeremie, Wenja and everyone I am forgetting to mention. Thanks also to Ale-Erbse and Taylor for the fun we had together. To Julia and Ale-Verna for the work done together. No, I am not forgetting about my crazy officemate. Thanks Guilhem for being who you are. It has not been the easiest office partnership at start, but I ended up appreciating your way of being. Thanks to the administration, to Rosa, Marina, Natalia, Margot for their professionalism and for all the help with endless bureaucracy. And thanks to Rike as well, for the same reasons and for being a great flat mate. Last but not least, a big thank you to the technicians of the workshop, Markus Sieben, Wolfgang Poppe, and colleagues.

Thanks to VERTIGO. Thanks to Greta and Joan for administration and personal support. Thanks to all my VERTIGO fellows for the great adventure these three years has been. In particular to Ines, PY, Inga and Matt for your friendship.

Thank you, Laura, for being a great colleague, but most importantly a good friend. For your honesty, your support and your seeing beauty everywhere, it is important and I sometimes forget.

Thank you, to the INGV Roma group for the field experiences and the lab welcoming: Valentino, Betta, Tullio and Piergiorgio.

Thank you, Juanjo, for the great collaboration and all the clever discussions about fluid dynamics and volcanoes.

Thanks to my Italian family in Munich: Betta, Benni e Gio since we hang out together, this city has a new colour! Thanks for the hanging out, the laughs and the more or less serious chatting. A big thank goes also to Gianlu, Nico and Ulrico. Vi voglio bene raga.

Thanks to those friends, I can always count on despite the distance: Lucia, Lucie, Stefania, Martina, Estelle, Edu, Erica, Priska, Alessandra, Laura. Thank you for showing you always care. You are important.

Finally yet importantly a big thanks goes to my family. To Mum, for showing me her greatest strength, to Dad, for showing me his greatest weakness. To my old brother, Andrea, for making me Aunt. To my little brother, Matteo, for the young man he is becoming. To my Grandma Luisa, my Aunt Anna and Uncle Virgilio for the endless support.

Grazie.

List of Content

Kurzfassung	I
Abstract	IV
Preamble.....	VII
Acknowledgments.....	IX
List of Content	XI
List of Figure.....	XIII
List of Tables	XV
List of Abbreviations	XVI
List of Symbols	XVII
1. Introduction	1
2. Background	5
2.1. Experimental literature.....	5
2.2. Vent Geometry	9
2.3. Conduit Length	13
2.4. Particle Load	13
2.5. Stromboli – the volcanic scenario.....	14
3. Fragmentation Bomb.....	17
3.1. The experimental apparatus	17
3.2. Data recording.....	20
3.3. Scaling.....	22
3.4 Particle fragmentation	25
3.5. Particle velocity.....	26
3.5.1 Maximum particle exit velocity (PEV).....	27
3.5.2 Temporal evolution of particle exit velocity	27
3.5.3 Discussion	31
3.5.4 Conclusions	35

3.6 Spreading angle	36
3.6.1 Initial gas and particle spreading angle	36
3.6.2 Temporal evolution of gas and particle spreading angle.....	38
3.6.3 Discussion	40
3.6.4 Conclusions	43
3.7 Mass ejection rate (MER)	45
3.8 Electrical discharges.....	49
4. Jet Buster.....	53
4.1 The experimental apparatus	53
4.2 Static analysis of the HP pipe.....	56
4.3 Gas-particle dynamics and the elastic response of the system.....	58
4.4 Analysis of particle dynamics	61
4.5 Discussion and remarks.....	64
5. Volcanic jets.....	67
5.1 Data recording	67
5.2 Pyroclasts velocity.....	68
6. Outlook.....	71
Appendix A	73
Appendix B	77
List of references	84

List of Figure

Figure 2.1 Schematic diagram.....	12
Figure 3.1 Overview and details of the fragmentation bomb.....	19
Figure 3.3 How the spreading angle is measured.....	21
Figure 3.4 GSD before (black histograms), and after (grey scale) ejection.....	25
Figure 3.5 Maximum particle exit velocity.....	26
Figure 3.6 Temporal evolution of particle exit velocity.....	29
Figure 3.7 Temporal evolution of particle exit velocity shown for the four different vent geometries	30
Figure 3.8 Particle velocity decay with the curve fitting from Alatorre-Ibargüengoitia et al. (2011)	33
Figure 3.9 Values of h expressed in centimetre versus vent geometry	34
Figure 3.10 Gas initial spreading angle.....	37
Figure 3.11 Initial spreading angle for the particle-laden jet	38
Figure 3.12 Temporal evolution of gas and particle spreading angle	39
Figure 3.13 Comparison of the temporal evolution of spreading angle.....	40
Figure 3.14 Example of original video frame	45
Figure 3.15 Diagrams showing MER and cumulative mass	47
Figure 3.16 Charts showing the instantaneous mass.....	48
Figure 3.17 Image a. shows millimetre size sparks.....	50
Figure 4.1 Schematic diagram of the "jet buster"	53
Figure 4.2 Example of two single frames from the original	54
Figure 4.3 Chart a. displays the trend maximum stress [N/cm^2].....	58
Figure 4.4 This figure shows a. the Δ time of the first arrival.....	59
Figure 4.5 A chronoplot showing the propagation.....	61

Figure 4.6 Evolution of particle velocity with time.	62
Figure 4.7 Chronoplot of experiment PARTB	64
Figure 5.1 a. Picture taken during the field campaign in May 2016.	68
Figure 5.2 Plots of pyroclast exit velocity with time	70
Figure A.1 Particle jet velocity decay with time for SL 1-2 mm particles, 15 MPa, 500 °C.....	74
Figure A.2 Particle jet velocity decay with time for SL 0.5-1 mm particles, 15 MPa, RT.....	75
Figure A.3 Particle jet velocity decay with time for SL 0.5-1 mm particles, 15 MPa, 500 °C.....	76
Figure B.1 Gas and particle spreading angle evolution with time for SL 1-2 mm particles, 15 MPa, 25°C.....	78
Figure B.2 Gas and particle spreading angle evolution with time for SL 1-2 mm particles, 15 MPa, 500°C.....	79
Figure B.3 Gas and particle spreading angle evolution with time for SL 0.5-1 mm particles, 15 MPa, 25°C.....	80
Figure B.4 Gas and particle spreading angle evolution with time for SL 0.5-1 mm particles, 15 MPa, 500°C.....	81
Figure B.5 Gas and particle spreading angle evolution with time for SL 0.125-0.250 mm particles, 15 MPa, 25°C.....	82
Figure B.6 Gas and particle spreading angle evolution with time for SL 0.125-0.250 mm particles, 15 MPa, 500°C.....	83

List of Tables

Table 3.1 Overview of experimental conditions.	18
Table 3.2 Summary of the gas properties	20
Table 3.4 Summary of the best fitting equation values.	28
Table 3.5 Summary of the number of experiments with visible electrical discharges.....	51
Table 4.1 Summary of the experimental conditions.....	55
Table 4.2 PMMA pipe properties	56
Table 4.3 Summary of the calculated tangential and radial stress.	57

List of Abbreviations

AP	ambient pressure
DNS	direct numerical simulations
g	grams
GSD	grain size distribution
HP	high pressure
MER	Mass eruption/ejection rate
ms	milliseconds
P	pressure
PEV	particle exit velocity
RT	room temperature

List of Symbols

A	Area [mm ²]
c	speed of sound [m/s]
d _p	particle diameter [mm]
E	elastic modulus [MPa]
h	height from the base of the sample in the tube to the observation point [m]
L	characteristic length [m]
M	Mach number
P	pressure [Pa]
R	gas constant [J/kg K]
Re	flow Reynolds number
Re _p	particle Reynolds number
St	Stokes number
t	time [s]
T	temperature [K]
U	flow velocity [m/s]
u _p	measured particle velocity [m/s]
v _{max}	maximum measured particle velocity [m/s]
ε	strain
Σ _T	stability number
γ	gas heat capacity ratio
μ	fluid dynamic viscosity [Pa s]
ρ	fluid density [kg/m ³]
ρ _p	particle density [kg/m ³]
σ	stress [MPa or N/cm ²]
ν	Poisson ratio
τ _p	particle characteristic relaxation time [s]
τ _{max}	maximum shear stress

1. Introduction

Explosive volcanic eruptions are the result of energetic magmatic fragmentation [Cashman and Scheu, 2015] and/or of violent interaction of magma and external water (i.e. lake, sea, groundwater and ice cap melting) [Zimanoswki et al., 2015]. Between the two mechanisms, the main difference is that exclusively gases exsolved from the magma drive magmatic fragmentation.

Upon fragmentation, magma, which is commonly considered a continuous liquid phase with dispersed gas bubbles and some crystals, evolves into a gas phase dragging dispersed particles (hot or cold from magma or country rock) out of the vent. Primary magmatic fragmentation occurs: 1) during rapid magma ascent, 2) after rapid decompression due to partial or total collapse of the volcanic edifice or the lava dome, 3) by magma shearing at conduit walls, or 4) when dome collapse occurs, by impact-induced explosion of hot solid blocks [Cashman and Scheu, 2015]. A “bottom-up” acceleration of bubbly magma or a “top-down” decompression front propagation, or both in sequence, drive then fragmentation [Cashman and Scheu, 2015]. In the first case, an upward acceleration of bubbly magma during decompression drives the fragmentation [Cashman and Scheu, 2015]. In the “top-down” propagation model, a sudden decompression event propagating downward in the conduit induces brittle fragmentation [Cashman and Scheu, 2015].

Despite the complex, non-linear processes that induce fragmentation, at explosive eruption onset, the potential energy (compressed gas in bubbles of the magma and exsolution by rapid diffusion of volatiles still dissolved in the melt) always transforms into kinetic energy via the expansion of gas [Kieffer, 1984; Woods and Bower, 1995]. The latter generates the ejection of pyroclasts into the atmosphere at a range of velocities and trajectory, posing potential hazard both in the near- and far-field. Ejected pyroclasts and gas may form eruptive plumes that commonly comprise a gas-thrust region overlaid, when formed, by a buoyant region [Woods, 1988; Valentine, 1998]. The gas-particle mixture in the gas-thrust or near-vent region can manifest the characteristics of a supersonic starting jet [Kieffer, 1984; Woods and Bower, 1995; Carcano et al., 2013]. Plume height is driven by kinetic energy and gas expansion in the near-vent region, followed by buoyancy due to the entrainment and heating of ambient air in the buoyant region [Woods, 1988; Valentine, 1998; Carcano et al., 2014]. With abundant fine ash present and a high thermal budget, an eruptive column

can become buoyant if sufficient ambient air is entrained and heated to reduce the density of the gas-particle mixture to values lower than the surrounding atmosphere. If those conditions are not met, a purely buoyantly column cannot form, leading to a (partial or total) collapse, generating pyroclastic density currents. Valentine [1998] summarized the boundary conditions favouring buoyant rise over collapse as 1) narrow vents, 2) high exit velocities, 3) high gas content and possibly 4) high pressure ratio at the vent.

The goal in volcanology research is to forecast volcanic eruptions and provide reliable information about the eruptive activity in terms of e.g., type, energy, duration, etc. [Sparks, 2003; Houghton et al., 2013]. These serve to assess and map the related hazards for the population and the infrastructures that might be at risk in case of an eruption. Technology is advancing rapidly and close to real-time volcano-monitoring systems based on seismic activity, geodesy and degassing are increasingly more reliable at providing indication of changes occurring on a volcano [Sparks, 2003]. The real-time monitoring coupled with the knowledge of historical activity and characterization of the eruption deposits can help further formulating probabilistic eruptions occurrence and define levels of areal dispersion. In addition, observational data on eruptions coupled with empirical and numerical modelling studies try to shed light on the complex dynamics ruling volcanic eruptions. In fact, it is indeed important to know when an eruption will take place, as well as to know how it will evolve and possibly end.

Explosive eruptions can sometimes be safely observed on the field or using satellites while occurring. Particle exit velocity, spreading angle (i.e., ejection trajectories) and their dynamic evolution with time have been measured successfully with laser Doppler techniques, high speed and infrared cameras [Dubosclard et al., 2004; Gouhier and Donnadiou, 2011; Taddeucci et al., 2012; 2015; Scharff et al., 2015; Gaudin et al., 2017]. In addition, acoustic power and intensity has been used to characterize volcanic jets velocity [Matoza et al., 2013]. Plume height, mass eruption rate (MER) and plume dispersal can be retrieved from high-speed imaging [Gaudin et al., 2014; Tournigand et al., 2017], satellites [Stohl et al., 2011] and from deposit investigations [Bonadonna et al., 2015]. The latter together with petrographic and geochemical characterization of the pyroclasts ejected can give insights on pre- and syn-eruptive conditions [Polacci et al., 2004; Dellino et al., 2012; Andronico et al., 2013]. The application of UAVs on volcanoes also allows for assessing crater area characteristics [Turner et al., 2017]. In recent years, another parameter that is getting more and more attention is volcanic lightning. It could provide a monitoring tool for volcanoes, also in remote areas as products of lightning strikes can be observed via satellite [Carn et al., 2016].

Furthermore, it could provide information about the plume characteristics and therefore, eruption source parameters [Anderson et al., 1965; McNutt and Williams, 2010; Behnke et al. 2013; Aizawa et al., 2016; Cimarelli et al., 2016; Van Eaton et al., 2016]. However, to link observations and source parameters is not trivial and it still requires a certain number of assumptions. Therefore, the knowledge of source conditions stays uncertain.

Empirical studies can help linking observations and input parameters, which are chosen and imposed experimental conditions. Laboratory experiments do not hold all natural complexities, but exactly for this same reason, they allow focusing on single simpler processes and understanding what parameters influence their dynamics. The final scope is to learn what to look for during a volcanic eruption and possibly recognize characteristic features that relate dynamics to source conditions [Alatorre-Ibargüengoitia et al., 2011; Kueppers et al., 2006a; Schmid et al., 2017]. Moreover, empirical results can provide insightful input parameters for numerical modelling and thus hazard assessment [Montanaro et al., 2016; Aubry et al., 2017].

The structure of the thesis is as follows.

In *Chapter 2 – Background*, I describe the current state of the art from a theoretical, numerical, experimental and observational point of view. I also briefly introduce and describe the differences between a subsonic, sonic and supersonic jet, and what are the important parameters defining the differences between the three cases.

Chapter 3 – Fragmentation Bomb is subdivided in several subchapters. I first describe the experimental setup and the experimental conditions in details together with the dimensionless scaling analysis. I then provide a complete overview of the results obtained for particle velocity and trajectory. I also describe the observations made on particle fragmentation, MER, and lightning. I discuss the significance and relevance of the results. Moreover, I consider the applicability of an empirical model from Alatorre-Ibargüengoitia et al. [2011] to the performed experimental conditions. A brief conclusive summary on important remarks ends this part.

Chapter 4 – Jet Buster is also divided in different subsections. I begin with a description of the experimental apparatus, highlighting the differences and complementarities of this system compared to the fragmentation bomb. I then present the main results and discuss them.

In *Chapter 5 – Volcanic Jets*, I show the observation made on jets produced by Stromboli volcano, Italy, recorded during a field campaign in May 2016. I compare the pyroclast ejection velocity quantified from Stromboli eruptions with the experiments performed.

Finally, in *Chapter 6 – Outlook*, I discuss possible future directions necessary to implement the empirical data set I created.

2. Background

The aim of this work is to understand better the roles of physical boundary conditions such as vent geometry, tube length, particle load, GSD, temperature and pressure on the dynamics of gas-particle jets generated by rapid decompression and gas expansion focusing on the near-vent region processes.

2.1. Experimental literature

Burgisser et al. [2005] provided a summary of the state of the art in experimental volcanology literature (see Table 1 in Burgisser et al. [2005] for a complete reference) spacing from volcanic plumes and surges to the magmatic system. They accounted only for works where a better understanding of the dynamics of a multiphase system was explicitly addressed [Burgisser et al., 2005]. Focusing on investigations on the explosive character of volcanic eruptions only, the majority of the studies cited by Burgisser et al. [2005] worked with injection of water and particle mixtures in water tanks while there was one study using a vertical shock-tube apparatus produced by Anilkumar et al [1993]. Burgisser et al. [2005] concluded that experiments above the “mixing transition” (with $Re > 10^4$) were still needed and that no experimental work to date was taking into account and reporting the scaling analysis of the St and stability number (Σ_T).

Beside, Cagnoli et al. [2002] used rapid decompression in a vertical shock-tube to analyse the dynamics of fine (38 and 95 μm) glass beads and used the results in a mathematical model to infer Vulcanian-like behaviour in volcanoes. Similar to Cagnoli et al. [2002], Chojnicki et al. [2006] performed a series of shock-tube experiments using 45 to 150 μm glass spheres, pressure ratios varying from 1 to 70 with an experimental Re_p reaching a value of 10^4 . They found that given an initial pressure ratio, the mixture velocity decreases with increasing particle size [Chojnicki et al., 2006]. Additionally, they stated that the measured mixture velocities were lower than the ones predicted by the pseudo-gas approximation and they explained the discrepancy with the presence of imperfect phase coupling and unsteady flow during the acceleration phase of the ejection [Chojnicki et al., 2006].

Differently, Clarke et al. [2009] and Chojnicki et al. [2015a,b] performed a series of injection experiments ($Re \sim 10^4$ - 10^5) where high-pressure mixtures of glass spheres (size ranging from < 10 to 45 μm) [Clarke et al., 2009] and aqueous solutions [Chojnicki et al., 2015a] were injected in a water-filled tank. These experiments were

used to characterize the dynamics and morphology of short-lived volcanic plumes from Vulcanian type eruptions [Clarke et al., 2009; Chojnicki et al., 2015a,b]. Moreover, Jessop et al. [2014; 2016] also performed injections of particle-water mixture into a water tank to investigate the dynamics of particle-laden jets issuing from fissure-like and caldera ring-dyke-like vents. Importantly, they defined the St regime of the mixtures they were using, which varied between $\ll 1$ to > 1 [Jessop et al., 2016]. Their goal was the description of a model for entrainment in Plinian plumes.

Solovitz et al., [2014] generated jets of compressed air through erodible vents fabricated with 3D printing. They observed that the vent was flaring rapidly and the flow dynamics changing in response. In particular, vent pressure was decaying and jet radius increasing [Solovitz et al., 2014]. Additionally, Graettinger et al. [2015] performed experiments involving buried chemical explosions to study the relationship between explosion energy, burial depth and multiple explosion on the resulting tephra distribution, as well as both subsurface and surface structures.

Beyond volcanology, the influence of different working conditions on gas and particle velocity is of interest for an enhanced understanding of general gas dynamics [Tsuji et al., 1984; Sommerfeld, 1994] or thermal spraying [Yin et al., 2016, and references therein]. Tsuji et al., [1984] performed analysis on particle-laden jets in a 5 m long tube where they looked into understanding the role of particles on gas turbulence. The apparatus was formed by a turbo blower providing airflow that was then mixed with plastic pellets of 200 μm to 3 mm in diameter and let flown in the 5 m tube in order to have steady conditions at the observation point [Tsuji et al., 1984]. They found that smaller size particles produced a decrease in gas turbulence, which was instead increased by larger particles. Sommerfeld [1994] described the effect of dispersed particles on the shock waves structure and the shape of the resulting underexpanded free jet via laboratory experiment. Using 26 and 45 μm glass beads at different particle mass loading, the Mach-disc, the shock wave normal to the flow direction of propagation, was observed to move upstream with increasing particle load [Sommerfeld, 1994]. Moreover, they highlight that particles were always moving slower than the gas at the nozzle exit [Sommerfeld, 1994]. Yin et al. [2016] provided a review on thermal spraying. The technique involves the use of accelerated gas-particle jets impinging on a solid substrate, where without fusion it allows the metal coating of the same substrate surface [Yin et al., 2016]. They summarized the efficiency of different working conditions as: 1) increasing gas pressure and temperature resolves in an increased particle velocity, with temperature more influential than pressure [Yin et al., 2016 and references therein]; 2) particles are usually slower with increasing particle size (size of powder particles ranging from 5

to 100 μm); 3) irregular particles are faster than spherical ones [Yin et al., 2016 and references therein]; 4) gas species have different acceleration efficiency, with helium holding the highest [Yin et al., 2016 and references therein].

The empirical contribution of the “fragmentation bomb” laboratory in Munich is diverse and started with Alidibirov and Dingwell [1996a,b]. The shock-tube system was created to investigate the fragmentation of vesicular magma subject to rapid decompression [Alidibirov and Dingwell, 1996a]. Cylinder of porous rocks are used as analogous of vesicular magma, fragmented via rapid decompression and analysed in terms of final GSD [Alidibirov and Dingwell, 1996a,b]. These experiments provided insights on the mechanism of magma fragmentation [Alidibirov and Dingwell, 1996b]. Kueppers et al. [2006a,b] investigated the efficiency and energy of fragmentation of natural volcanic samples applying fractal analysis on the GSD of experimentally fragmented pyroclasts. Scheu et al. [2006; 2008] studied the fragmentation threshold necessary to fragment samples from Unzen volcano, Japan. They observed a strong relationship between open porosity, applied pressure and fragmentation efficiency [Kueppers et al, 2006b; Scheu et al., 2006]. Alatorre-Ibargüengoitia et al. [2010, 2011] quantified the energy consumption due to fragmenting and ejecting porous rocks for a Vulcanian analogous scenario. Moreover, they proposed for the first time an empirical model to relate the particle velocity decay with time to the location of the sample inside the shock-tube [Alatorre-Ibargüengoitia et al., 2011]. This model found also application on volcanic eruptions [Taddeucci et al., 2012], and it is discussed in more details in section 2.4 and 3.4.3 where its applicability to the current experimental results is tested.

In addition, the shock-tube apparatus was used to characterize hydrothermal systems and phreatic eruptions [Mayer et al., 2015; Montanaro et al., 2016]. Mayer et al. [2015] experimentally investigated the influence of hydrothermal alteration and fragmentation mechanism on fragmentation efficiency, particle ejection velocity and resulting particle characteristics. The fragmentation mechanisms tested were steam flashing and gas expansion, with steam flashing resulting in greater efficiency [Mayer et al., 2015]. Montanaro et al. [2016] investigated the effect of liquid fraction and rock petrophysical properties on steam driven ejection and relative explosive energy. They estimated that steam flashing is one order of magnitude more energetic than argon gas expansion and that weak rocks presenting low permeability were fragmenting more efficiently generating a larger amount of fines [Montanaro et al., 2016]. Spina et al. [2016] used slow decompression experiment with silicon-oil-based suspensions as analogous for degassing in basaltic systems. They characterized to role of particle concentration and shape on gas volume fraction and fluid motion. Schmid et al. [2017]

investigated the behaviour of mud explosions characteristic of volcanic lakes using rapid decompression of water-clay suspensions. They defined a series of rheological regimes that can be used for characterizing field observations.

The present study focuses on the near-vent region, where, independently of fragmentation mechanism, impulsively released gas-pyroclast mixtures are ejected into the atmosphere following rapid decompression and gas expansion [Kieffer, 1984; Woods and Bower, 1995; Carcano et al., 2013]. This takes place over a wide range of eruption styles as e.g. Strombolian or Vulcanian eruptions, parts of Plinian eruptions or phreatomagmatic explosions [Koyaguchi and Woods, 1996; Gouhier and Donnadieu, 2011; Taddeucci et al., 2012; Scharff et al., 2015]. Moreover, if sonic conditions are reached at vent exit a gas-particle jet with supersonic characteristics can form [Kieffer, 1984; Kieffer and Sturtevant, 1984; Woods and Bower, 1995; Ogden, 2011; Carcano et al. 2014]. I investigated the ejection of a non-coupled ($St \gg 1$) gas-particle mixture using rapid decompression in two shock-tube setups: 1) at LMU Munich (called “fragmentation bomb”) and 2) at INGV Rome, (called “jet buster”). During these experiments, I varied the following parameters:

1. Setup geometry (tube length and vent shape),
2. particle load,
3. starting grain size distribution (GSD),
4. experimental temperature, and
5. reservoir overpressure (150 bar in the fragmentation bomb, and 2 bar in the jet buster)

The aim is a better determination of the relative control of these parameters on mixture ejection and a better determination of the relation between observable eruption dynamics and the underlying conditions during an explosive eruption.

2.2. Vent Geometry

The role of vent geometry on plume dynamics during explosive eruptions has been the focus of studies on ejection velocity [Wilson et al., 1980; Wilson and Head, 1981; Kieffer, 1989; Ogden, 2011] and jet radius [Woods and Bower, 1995; Jessop et al., 2016]. If ejection velocity is mainly determined by gas mass fraction, gas overpressure at the vent and magma temperature [Woods and Bower, 1995], a flaring vent can help driving the transition between sub and supersonic flow [Wilson and Head, 1981; Kieffer, 1989]. Indeed, the vent controls, together with conduit characteristics, the pressure ratio between the ascending flow and the atmosphere and therefore regulates jet dynamics [Saad, 1985; Ogden, 2011]. Furthermore, vent characteristics seem to affect the MER, as it is proportional to the cross-sectional area of the jet, which is related to the vent size [Koyaguchi et al., 2010; Ogden, 2011; Saffaraval et al., 2012; Jessop et al., 2016]. In nature, a wide range of vent geometries has been observed, from circular to elongated, and these features are dynamically evolving. Such shape changes are intrinsically related to eruption dynamics and may involve both widening (by, e.g., vent erosion and flaring) and narrowing (by, e.g., collapse, infill or accretion). At constant MER, an increase in the crater diameter will influence the flow dynamics such that column collapse becomes more likely [Wilson et al., 1980; Koyaguchi et al., 2010; Solovitz et al., 2014]. Moreover, changes of vent geometry will also affect the flow dynamics in the underlying plumbing system. Cone build-up by near-vent deposition and partial obstruction of the crater by pyroclastic material will additionally alter flow and ejection dynamics [Capponi et al., 2016].

To better understand how the geometry of the vent can have a large influence in the dynamics of a starting jet, one can refer to the one-dimensional isentropic theory for a convergent-divergent vent, also called “de Laval nozzle”. In aerospace engineering and gas dynamic, the exit orifice is called nozzle, indifferently of geometry. Here, to distinguish the different geometries adopted, the term “nozzle” is used only to refer to the converging vent geometry (see section 3.1 “The Experimental ‘Setup’” and Figure 3.1 for details). The convergent part of a “de Laval nozzle”, the throat, serves to accelerate the flow. Nevertheless, the conditions that the flow will actually reach at the throat, in the divergent part or in the atmosphere, depend on the vent design as well as on the stagnation pressure in the reservoir, with respect to ambient atmospheric pressure [Saad, 1985, Woods and Bower, 1995; Koyaguchi et al., 2010; Ogden 2011]. Vent design means the characteristic area ratio between exit (A_2) and critical area (A^*). The critical area is the narrowest area the flow has to pass through. The flow can be subsonic (Mach number, $M < 1$), sonic or choked ($M = 1$) or supersonic ($M > 1$) and

the relationship between M and the area ratio is expressed as follow [Saad, 1985; Woods and Bower, 1995; Koyaguchi et al., 2010]:

$$\left(\frac{A_2}{A^*}\right) = \left(\left(\frac{2}{\gamma+1}\right)^{\frac{\gamma+1}{2(\gamma-1)}}\right) \frac{1}{M} \left[1 + \left(\frac{\gamma-1}{2}\right) M^2\right]^{\frac{\gamma+1}{2(\gamma-1)}} \quad (1).$$

Where γ is the gas expansion coefficient. Equation (1) can be resolved to obtain M for a specific vent geometry with known area ratio. The value obtained is the designed Mach number; its actual applicability further depends on the pressure ratio between the reservoir (P_r) and the external ambient pressure (P_a). This relationship is expressed as follows:

$$\frac{P_r}{P_a} = \left(1 + \frac{(\gamma-1)M^2}{2}\right)^{\frac{\gamma}{\gamma-1}} \quad (2).$$

It is possible to describe seven main possible dynamic scenarios for a convergent-divergent vent considering the pressure ratio between the reservoir and the ambient conditions. Figure 2.1 presents a schematic description of the scenarios that will be now described in details. In case (a) of Figure 2.1 the flow is subsonic everywhere. The flow accelerates, with a consequent pressure drop, from the reservoir through the throat section. Here, the flow reaches maximum subsonic velocity and then decelerates in the divergent section and exhausts in the atmosphere always subsonically. If the pressure in the reservoir increases, scenario (b) in Figure 2.1 could originate. Here, the flow can reach $M=1$ at the throat, which is the narrowest point the flow has to cross in the system, and be choked. Any further increment of the reservoir pressure will not modify this condition, i.e., at the throat section there will always be $M=1$, while a reduction of the reservoir pressure will produce case (a) again. In case (b), the flow is only choked at the throat and in the divergent part starts decelerating. A further increase in the reservoir pressure produces a region of supersonic flow downstream of the throat (c). The supersonic flow accelerates in the divergent area, as it gets bigger, until it is stopped by a shock wave, normal to the flow direction, formed in the divergent section (Figure 2.1c). The flow undergoes abrupt deceleration, with an instantaneous pressure growth as it passes the shock (see the plot in Figure 2.1), and continues as subsonic flow outside the vent and in the ambient region. By increasing further the reservoir pressure, the shock moves downstream to the vent exit (d). In this case, the velocity of the flow will be very high before the shock and again subsonic after it. An additional increment in the reservoir pressure provokes an outward bending of the shock (e). It originates a complex pattern of shocks, some of which normal to the flow, and reflections. As a consequence, outside the vent region a mix of super- and subsonic flow is generated and before passing through the normal shock, the jet is initially contracted. In this condition, the jet is called overexpanded, which means that

the pressure at exit is lower than ambient pressure or in other words: the vent has expanded the flow too much. A further increase of pressure in the reservoir leads to weaken the wave pattern. Eventually, the ratio vent exit to ambient pressure reaches equilibrium and a uniformly supersonic jet is obtained (f). This is referred as “design conditions” or “correctly expanded flow”. Any additional pressure increase will outbalance once again the pressure ratio at the exit. When at vent exit the pressure is still higher than ambient pressure, expansion waves form and produce further acceleration in the jet, which will be supersonic and underexpanded, case (g). Expansion waves, contrary to normal shocks, produce a drop in pressure and therefore a velocity acceleration; see the plot in Figure 2.1.

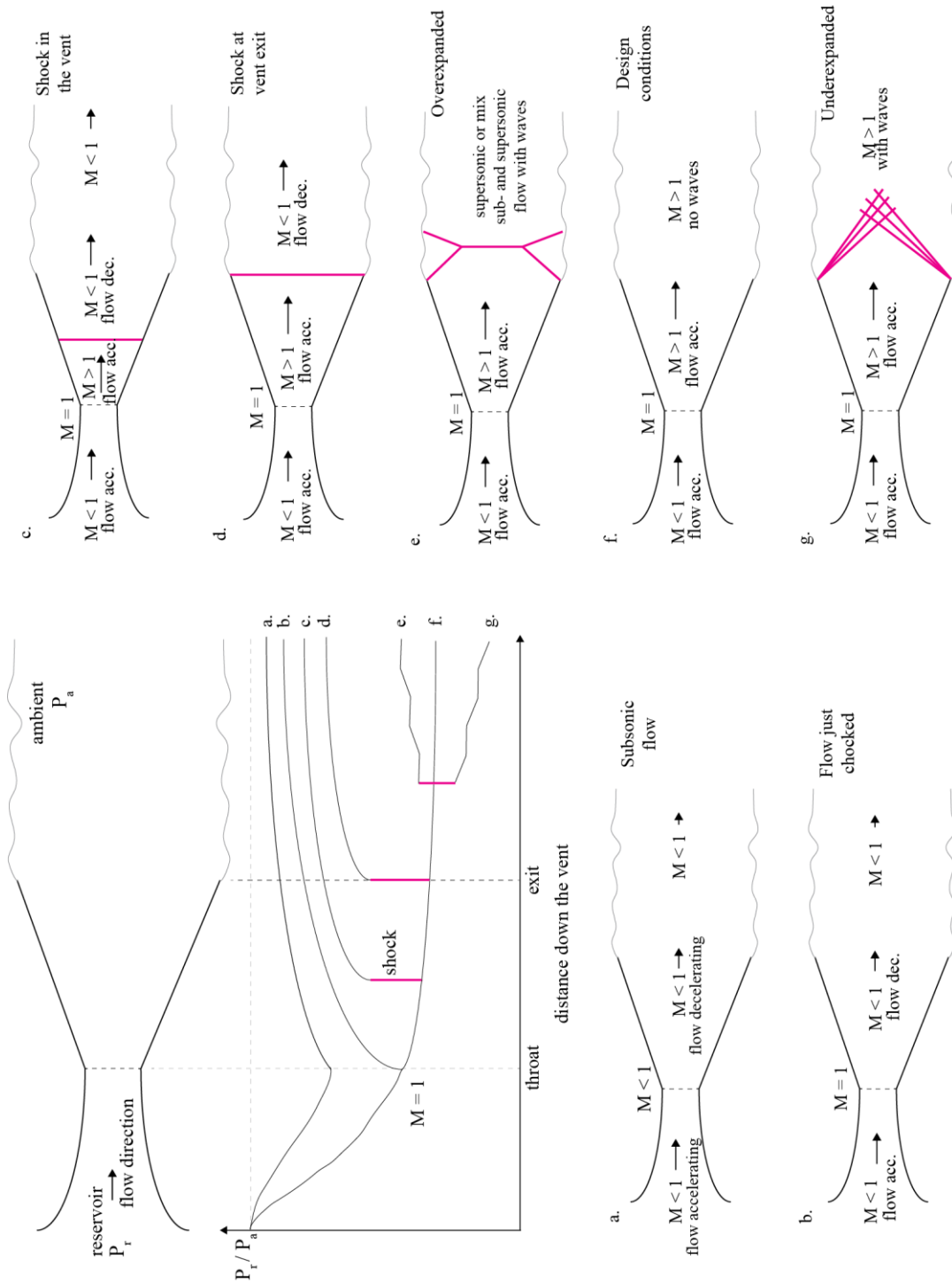


Figure 2.1 Schematic diagram describing how the pressure ratio between the reservoir and ambient influence the dynamics inside a convergent-divergent vent. Top left a cartoon representing a “de Laval nozzle”, below it a plot showing the drop in pressure ratio moving from the reservoir to the exit and outside the vent. In fuchsia are the shocks and the expansion waves only for case (g). From bottom left to the column on the right a series of cartoons show what happens in the vent in the different cases. (a) Subsonic flow. (b) Flow just choked at the throat. (c) A shock forms in the divergent part of the vent. (d) A shock forms at vent exit. (e) The jet is supersonic and overexpanded as a pattern of complex shocks forms outside the vent. (f) Designed conditions, the jet is uniformly supersonic without shocks or waves present. (g) The jet is supersonic and underexpanded as expansion waves form outside the vent.

2.3. Conduit Length

Conduit length can also be defined as the depth in the conduit where the magma surface is located, where fragmentation of a bubbly magma occurs and therefore where the gas-particle mixture starts its raising and possibly ejection [Wilson and Head, 1981; Koyaguchi, 2005]. Fragmentation depth is regarded as an important influence factor in explosive eruptions and therefore its estimation is essential [Wilson and Head, 1981; Gardner et al., 1996; Taddeucci et al., 2002; Polacci et al., 2004; Dürig et al., 2015]. It can affect both pyroclast properties [e.g., size and vesicularity, Gardner et al., 1996], because of possible differences in magma composition and volatiles content at different depths [Polacci et al., 2004], and pyroclasts ejection trajectories, i.e. spreading angle, because of possible different particle-particle interactions, particle-wall interactions and gas acceleration efficiency on particles [Dürig et al., 2015; Taddeucci et al., 2017]. The reconstruction of the fragmentation level is subject of different studies using theoretical analysis [Wilson and Head, 1981], numerical modelling [Polacci et al., 2004], petrographic analysis [Gardner et al., 1996] and field observations applying geometrical methods [Dürig et al., 2015] or empirical relationship [Taddeucci et al., 2012]. Dürig et al. [2015] proposed a method to estimate the depth in the conduit where pyroclasts originated using geometrical reconstructions of straight-only trajectories during the 2010 Eyjafjallajökull volcano, Iceland, eruption. Taddeucci et al. [2012] instead applied an empirical relationship obtained investigating particle velocity decay in shock-tube experiments by Alatorre-Ibargüengoitia et al., [2010; 2011]. They wanted to define the base and volume of ascending gas slugs generating short-lived explosions at Stromboli volcano, Italy [Taddeucci et al., 2012]. The empirical relation expresses as follows [Alatorre-Ibargüengoitia et al., 2011]:

$$v_p = \frac{v_{max}}{1 + \frac{v_{max}t}{h}} \quad (3),$$

where t is time, v_{max} is the maximum ejection velocity measured and h corresponds to the base of the sample in the autoclave. I tested the applicability of Equation 3 to the present experimental conditions and I discuss about it in section 3.5 of this thesis. Gaudin et al. [2014] also applied a variation of the formulation of Equation (3) on ejections from Stromboli, Italy, and Yasur, Vanuatu, volcanoes.

2.4. Particle Load

Both the amount and size of the ejected particles (“volcanic cargo”) have a great impact on jet dynamics. Two-way and four-way coupling interactions between fluid (melt or gas) and particles in volcanic systems have been demonstrated theoretically [Bercovici and Michaut, 2010], numerically [Carcano et al., 2014; Cerminara et al., 2016],

observationally [Taddeucci et al., 2015] and experimentally [Burgisser et al., 2005; Jessop et al., 2016]. A gas-pyroclast mixture may act as a pseudo-gas if particle concentration, mass and momentum exchange are small enough, i.e. $St < 1$, [Kieffer and Sturtevant, 1984; Burgisser et al., 2005; Carcano et al., 2013]. Accordingly, the commonly assumed “pseudo-gas” Eulerian model for the gas-particle mixture is oversimplified in most volcanic cases.

On the effect of particle loading on particle velocity, Budilarto (2003) reported experimental results on particle-laden jets performed in a downward jet flow facility using compressed air and glass beads of 25 and 70 μm . They showed a decrease in the decay rate of the particle velocity with increasing particle loading for the same particle size and for increasing particle size when considering equal particle loading [Budilarto, 2003, and references therein].

It is also of great interest to be able to quantify reliably the amount of pyroclasts been ejected, i.e. the MER. This parameter can be estimated using semi empirical relationship from plume height [Mastin et al., 2009] or numerical modelling [Bonadonna et al., 2012]. High uncertainties in these estimations remains [Bonadonna et al., 2015]. Gaudin et al. [2014] used automated image analysis on recorded eruptions to characterize the MER.

2.5. Stromboli – the volcanic scenario

Stromboli volcano is part of the Aeolian Island volcanic arc in Italy. From his name, the term Strombolian was originally forged by Giuseppe Mercalli at the beginning of the XX century to describe a volcano erupting “only fresh incandescent pyroclastic material and fluid” [e.g., Gaudin et al., 2017]. It rises about 3000m above the seafloor of the Tyrrhenian Sea, while his summit is about 900 m above sea level. The volcano has three main craters called NE, Central and SW in which several active vents [Turner et al., 2017] regularly produce explosions. The activity at the different vents can greatly vary both in style and intensity, but the common activity is usually described consisting in repeated mild Strombolian events where, at intervals of about tens of minutes, pyroclasts are ejected at an height that usually does not exceed 200 m [James et al., 2013]. To this common activity, Stromboli seldom adds paroxysmal events that largely differ from the daily style in terms of discharge rate, depth of magma origin and petrographic characteristics of the pyroclast ejected. Lava effusion sometimes anticipated paroxysmal activity [Metrich et al., 2005].

Focusing on the “normal” activity at Stromboli, his ejections have been widely studied in the past years. Especially since the booming of the applicability of high-speed imaging techniques coupled with other methods, e.g. acoustic and seismic measurements, infrared imaging, petrographical analysis, etc. [Andronico et al., 2013; Capponi et al., 2016;

Gaudin et al., 2014; 2017; Lautze et al., 2013; Taddeucci et al., 2012; 2014; 2015; Tournigand et al., 2017]. During a field campaign in May 2016 on Stromboli, I was able to record seven jet-like ejections from one of the active vents of the SW crater. According to the recent classification scheme proposed by Gaudin et al. [2017], these eruptions can be described as “Type 1 (bomb-dominated) rapid explosions”. I used the velocity profiles and particle trajectory of the recorded jets on Stromboli for a comparison with the experimental results.

Page intentionally left blank

3. Fragmentation Bomb

In this chapter, I describe the “fragmentation bomb” system, the experiment performed with it and main findings related to particle fragmentation, velocity, trajectory as well as mass ejection rate and electric discharges.

3.1. The experimental apparatus

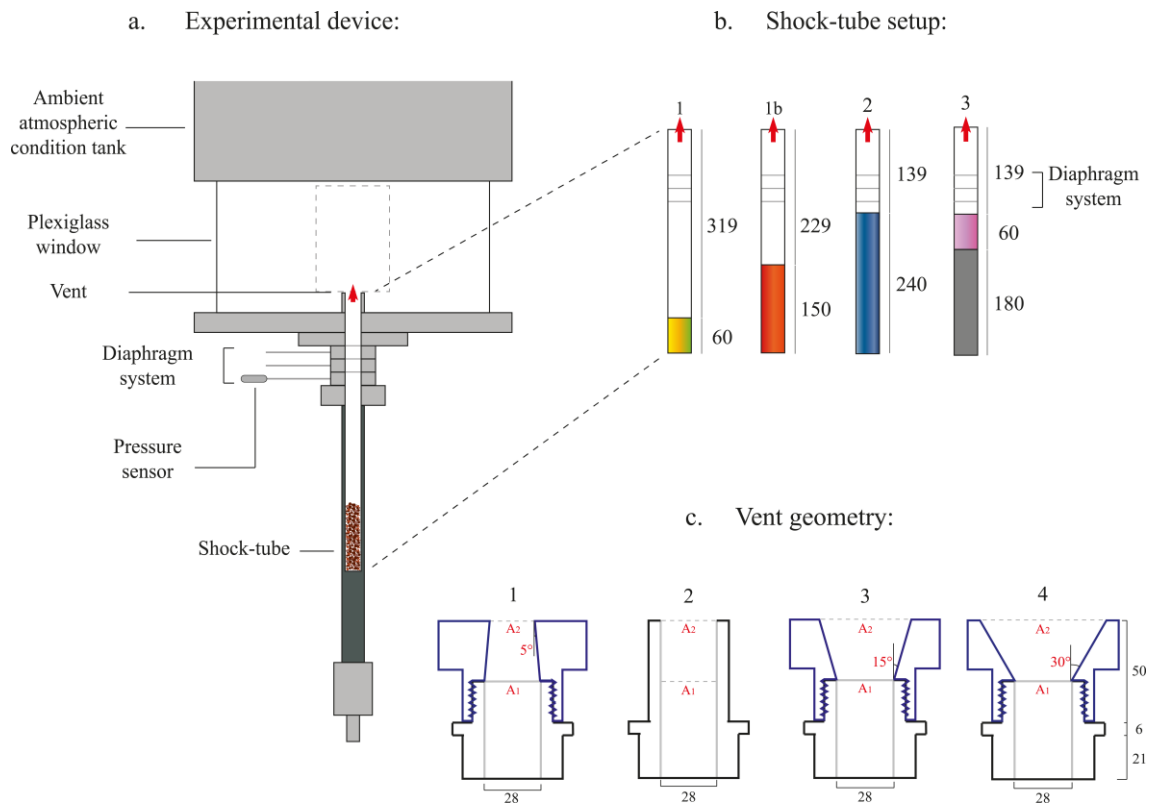


Figure 3.1 Overview and details of the “fragmentation bomb” (all values are in mm). a. The experimental device (not to scale), the grey dot-lined rectangle in the Plexiglas window represents the camera field of view. b. Four different starting conditions of tube length and particle load were chosen. The rectangles in colour indicate the tube volume initially occupied by the granular sample (i.e. sample chamber volume in Table 3.1). c. Four distinct vent geometries were used: (1) converging nozzle ($A_2/A_1 = 0.67$, A: area); (2) cylinder ($A_1 = A_2$); (3) diverging funnel 15 ($A_2/A_1 = 2.36$); (4) diverging funnel 30 ($A_2/A_1 = 4$). The diameter of A_1 is always 28 mm.

The experimental apparatus here used (Figure 3.1a) is an adapted version of the “fragmentation bomb” already described in Kueppers et al. [2006a,b] and Alatorre-Ibargüengoitia et al. [2011] and a highly evolved model of the original fragmentation tank of Alidibirov and Dingwell [1996a,b]. The apparatus is composed of a shock-tube (made of Nimonic 105 alloy) which allows for high P-T conditions (up to 100 MPa and 850 °C). The total pressurized volume is 60 (setup 3) and 240 mm high (setups 1, 1b and 2),

respectively, and has an internal diameter of 26 mm (Figure 3.1a, and b). The sample (using variable particle loads, see colours in (Figure 3.1b) is placed therein without pressurized gas beneath. I incrementally pressurize the system with Argon gas sealing the tube with a set of controlled-release diaphragm system. On diaphragm burst, four triangle-shaped segments of each diaphragm are bent upwards and generate some internal diameter variation (between 26 and 28 mm). A pressure sensor records the pressure drop and triggers the recording system. The ejection takes place into a 3.35 m high stainless steel tank at ambient conditions. I repeated each set of conditions at least 3 times, in order to verify experimental repeatability. The experiments have been performed during the course of >12 months with the following average conditions in the lab: 25°C, 30 % humidity and 1021.1 hPa. Through a cylindrical Plexiglas tube at the base (Figure 3.1a), direct visual observation and high-speed video filming are possible. A shock-absorbing panel at the top of this low-P section reduces particle loss and impact-induced fragmentation.

Table 3.1 Overview of experimental conditions: Left block: Grain size distribution (GSD, in mm) and temperature (T, in °C). Centre block: Distance of the sample surface from the vent exit before decompression (in mm), volume of the sample chamber (in m³) and the particle load (in grams). Right block: Exit area (in mm²) and exit diameter (in mm) for each vent geometry. *Averaged over several experiments.

GSD	T	Setup	Surface distance	Sample chamber V	Particle load*	Vent geometry	Exit area (A ₂)	Exit d
mm	°C		mm	m ³	g		mm ²	mm
1 - 2	25	1	319	3.2*10 ⁻⁵	34.8±2.8	Noz.	415	23
0.5 - 1	500	1b	229	8.0*10 ⁻⁵	83.0±2.3	Cyl.	615	28
0.125 - 0.250		2	139	1.3*10 ⁻⁴	150.9±8.6	Fun. 15	1451	43
		3	139	3.2*10 ⁻⁵	36.0±3.4	Fun. 30	2462	56

In this study, the primary variables were (Table 3.1):

- 1) Vent geometry (Figure 3.1c). Four different geometries applied:
 - i. a nozzle with converging walls ($\alpha = -5^\circ$) and area ratio $A_2/A_1 = 0.67$,
 - ii. a cylinder where $A_2=A_1$,
 - iii. a funnel with diverging walls ($\alpha = 15^\circ$) and area ratio $A_2/A_1 = 2.36$, and
 - iv. a funnel with diverging walls ($\alpha = 30^\circ$) and area ratio $A_2/A_1 = 4$.

All of them are made from stainless steel, have a constant height (77 mm) and internal diameter (28 mm). Vent shape does not change during the experiments (not erodible), differently to other studies [Solovitz et al., 2014].

- 2) The setups (1, 1b, 2 and 3 in Figure 3.1b and Table 3.1) differ in the distance of the sample surface from the vent before decompression and the particle load. Setups 1 and 3 have identical particle load, but different sample surface

location. Setups 2 and 3 have different particle load, but identical sample surface location. Setup 1b was added to investigate the observed differences between setups 1 and 3 with setup 2. I performed setup 1b experiments only with the cylindrical vent and 25°C to check for the influence of gas flux on the observed temporal ejection velocity evolution. I chose the cylindrical geometry for standard as it is the simplest geometry and the one commonly used for eruption modelling, and I did not observe a large influence of vent geometry on the velocity evolution with time (Figure 3.7, A1-3).

- 3) Sample properties. The sample is composed of fragments of basaltic lava with 15% porosity, named Schaumlava (SL), from the East Eifel volcanic field (Germany), and produced by mechanical crushing for industrial purposes. The sample was separated by wet sieving in three different size fractions: coarse (1-2 mm, Figure 3.2a), medium (0.5-1 mm, Figure 3.2b) and fine (0.125-0.250 mm). Douillet et al. [2014] have measured density (2.5 g/cm^3) and shape parameters. In every setup (1, 1b, 2 and 3), the loosely packed particles occupy $41.7 \pm 1.8 \text{ vol.}\%$, $43.8 \pm 1.6 \text{ vol.}\%$ and $50.2 \pm 1.3 \text{ vol.}\%$ for coarse, medium and fine grain size distribution, respectively, irrespective of setup.
- 4) Two temperatures were used, 25°C (RT) and 500°C, the latter of which was achieved by using an external tube furnace. Before decompression, all particles are in thermal equilibrium with the surrounding gas phase. Upon decompression, the expanding gas phase is rapidly cooled. The degree of cooling is possibly affected by the heat capacity of the sample. This material

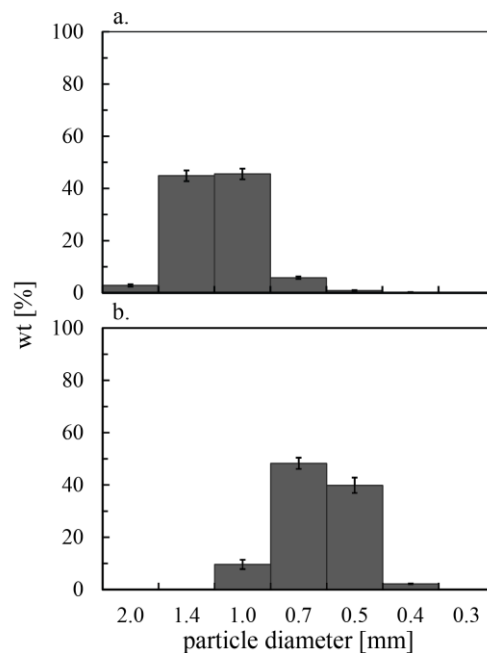


Figure 3.2 Grain size distribution before decompression plots of the 1-2 mm (a) and 0.5-1 mm (b) samples, respectively.

property has been measured using a *Netsch DSC 404C Pegasus* differential scanning calorimeter. A specific heat capacity between 830 (at low temperature) and 1000 J/kg/K (at 500°C) has been evaluated. These values are in agreement with published data for basalt [Waples and Waples, 2004].

- 5) I applied a gas overpressure or gauge pressure, (Argon) of 15 MPa in the shock-tube for all experiments. I use Argon gas to pressurize the shock-tube assuming that the difference in its heat capacity ratio γ compared to H₂O or CO₂ is of subordinate importance (Table 3.2). H₂O or CO₂ are the most abundant gas species in any terrestrial eruption.

Table 3.2 Summary of the gas properties for Argon, used to perform the experiments, and H₂O and CO₂ two of the main volcanic gases. *Water vapour

Parameter \ Gas	Ar	H ₂ O*	CO ₂
Specific gas constant R [J/kg/K]	208.0	461.5	188.9
Heat capacity ratio γ	1.67	1.33	1.29

3.2. Data recording

I record the experiments with a Phantom high-speed camera (V710 and V711) at 10000 fps. The field of view (resolution of 800x600 or 1024x600) is 20 cm high. The video is black and white. The optimal exposure is found to be 4 μ s with an EDR (extreme dynamic range) value of 1 μ s.

I use MTrackJ, an ImageJ plugin, to manually track single particles and measure their velocity. I evaluate velocity by measuring the distance of single particles in 5 consecutive scaled frames and averaging the velocity for this time interval. I can detect no perceptible acceleration or deceleration. I track up to 40 particles per video covering the entire duration of particle ejection at a resolution of 30 frames. The particle ejection lasted between 30 and 100 ms, with the shortest being the setup 3 ejections, from when the first particles exit the vent until particle ejection ceases. The recording system and therefore the analytical methodology has some limitations. The first is that for the fine particle fraction, manual tracking of single particles was not possible due to particle resolution; therefore, data on the velocity for these experiments is not available. The second is that at the beginning of particle ejection in experiments with high particle load, e.g., setup 2, it can be harder to discern single particles due to the high particle concentration in the jet. Zooming closer to the jet and look for singular particle features helps to resolve this difficulty.

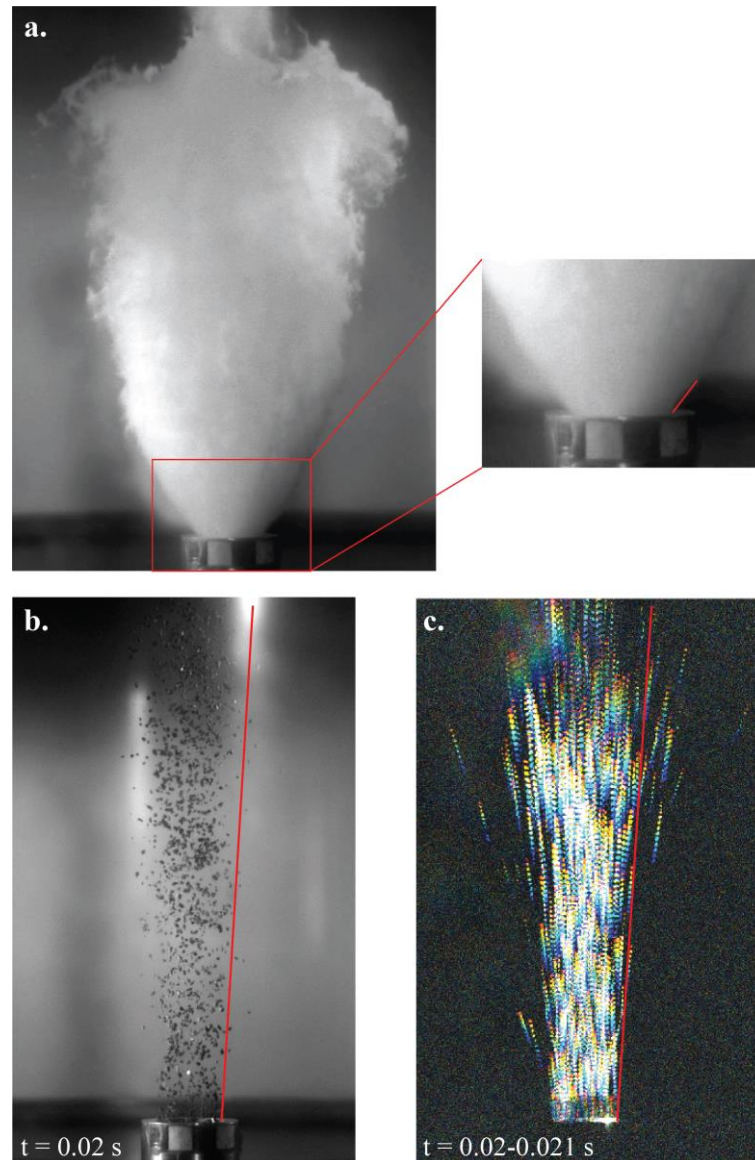


Figure 3.3 How the spreading angle is measured for the gas (a) and the particles (b, c). The gas expansion is measured very close to the vent, see zoom in (a). For the particles, the entire visible jet length is considered (b). The main difficulty when measuring the particle spreading angle is to be able to discern between main jet, formed by particles following the main flow direction, and outliers, particles clearly deviating from the main jet because of secondary processes such as particle-particle collision or particle-wall collision. To discern the outliers is not always trivial. The image in (c) is created by image subtraction of 10 frames, this way the trajectory of the particles (from blue to red) at different times is highlighted. From (c) is clearly visible which particles are not following the main jet. Image subtraction is used every time outliers were not easily discernible.

I then quantify the gas and particle spreading angle again using ImageJ. At subsequent frames, I draw a line (Figure 3.3) with a starting point located at the lateral extremity of the gas or particle jet at the vent exit and a second ending point following the maximum lateral spread of the jet. For the gas spreading angle (Figure 3.3a), I draw a very short line, zooming very close to the vent exit, as the maximum spreading angle, or maximum Prandtl-Meyer expansion, which forms the expansion wave diverging from the sharp exit corner of the vent, results just at the lip of the vent. The measurement is taken every other

frame from when the second diaphragm bursts out until gas is visible. Argon becomes visible because it undergoes large expansion and therefore cooling and condensation. In the experiments at room temperature, the condensation starts at vent exit, while in the experiments at higher temperature at the exit there is always a zone of lower condensation few millimetres high where argon can result still colourless and hardly visible. The measurement in this case requires being very careful, it results that in high temperature experiments the standard deviation between the measurements made at the right and left side of the jet can be larger than for room temperature experiments.

For the particle spreading angle case (Figure 3.3b), I draw the line considering the entire field of view, this way considering the entire length of the particle laden jet and its deviation from a vertical central line. I perform the first measurement of particle spreading angle when the jet entirely fills the field of view, which commonly happens about five frames after the first particles exit the vent. A difficulty I sometimes encounter during the measurements is about clearly discern particle outliners. Outliners are those particles that, instead of following the main jet flow direction, are deviating due to secondary processes, such as particle-particle and particle-wall collision or due to broken pieces of diaphragm that might fly in the field of view. The latter usually happening at ejection onset only. To discern particle outliners is not always trivial, therefore when necessary an image subtraction tool can be applied. Figure 3.3c shows an image created by subtracting 10 frames to each other, this way highlighting the pattern followed by the particles in time (from blue, earlier frame, to red). In Figure 3.3c, it is easier to discern which particles are deviating than for example in Figure 3.3b. Another limitation of the image analysis is that at some point in time particles will start falling back. This happens earlier for the fine particle fraction and setup 3, and creates a very dusty environment where the main jet results obscured and not easily trackable. This resolves in an apparent premature end of the ejection in some cases (see section 3.5.2 and following).

3.3. Scaling

For a close comparison of nature and experiment, it is important to compare the dynamics of the processes through a non-dimensional analysis of the main controlling forces on the flow. Here, I discuss Reynolds and Stokes numbers as the inertial and viscous forces dominating a momentum-driven flow, such as the flow in the near-vent region [Kieffer and Sturtevant, 1984], and to estimate the degree of coupling between gas and particles. The flow Reynolds number (Re) defines the ratio of inertial to viscous forces in a flow:

$$Re = \frac{\rho UL}{\mu} \quad (4),$$

where ρ and μ are the fluid density and dynamic viscosity respectively, U the flow velocity and L a characteristic length, for example the vent radius [Clarke, 2013] or the jet diameter [Kieffer and Sturtevant, 1984].

Re for volcanic eruptions ranges between 10^5 and 10^8 [Clarke, 2013] or can be as high as 10^{11} [Kieffer and Sturtevant, 1984]. The typical flow Re for these experiments ranges from 10^6 to 10^8 (Table 3.3), calculated using the one-dimensional isentropic theory [Saad, 1985; Woods, 1995] by estimating Argon gas density, viscosity and flow velocity at specific P and T values. I use the area ratio (see Equation 1) between the exit (A_2 in Figure 3.1 and Table 3.1) and the critical area (A^*) to estimate the flow Mach number (M), reported in Table 3.3, and therefore every other descriptive flow parameter. The critical area is defined by the narrowest cross-sectional area the flow has to pass through. In the case of this experimental setup, for the cylinder, funnel 15 and funnel 30 geometry the critical area is the sample chamber area, with a diameter of 26 mm and therefore $A^* = 531 \text{ mm}^2$. The exit (A_2) to critical (A^*) area ratio are 1.16, 2.73 and 4.64 for the cylinder, funnel 15 and 30, respectively. As a result, the exit M number is > 1 for these geometries (Table 3.3). On the other hand, in the nozzle vent the critical and exit area are the same, this provides $M = 1$ at the exit.

Although Re is a highly dynamic parameter, I estimate it for throat, lip of the vent and at fully expanded conditions, reached when the flow has expanded to ambient pressure. As characteristic length (L), the diameter of the vent at the throat, for throat conditions, and at its' upper end, for lip and fully expanded conditions, is chosen accordingly.

The Stokes number (St) describes the particle inertial response to the flow and it is calculated as follows:

$$St = \frac{\tau_p U}{L} \quad (5),$$

where τ_p is the characteristic relaxation time of the particles and it is calculated from equation (6) [Elghobashi and Truesdell, 1993; Carcano et al., 2013]:

$$\tau_p = \frac{\rho_p d_p^2}{0.33 Re_p \mu} \quad (6),$$

where ρ_p is the particle density, d_p is the particle diameter, μ is the fluid dynamic viscosity and Re_p is the particle Reynolds number. Re_p serves as correction factor accounting for relative velocities between gas and particles. Re_p is calculated according to equation (7):

$$Re_p = \frac{d_p \rho |U - u_p|}{\mu} \quad (7),$$

where u_p is the measured particle velocity and U is the flow velocity theoretically estimated for the fully expanded conditions using equation (8) from the one-dimensional isentropic theory [Saad, 1985; Woods, 1995]. The experimental apparatus does not allow for measuring directly the flow velocity of the pure gas, U . I measured the propagation

velocity of the condensed gas front directly above the vent from image analysis. As there are measurement ambiguities and large variations (e.g. 366 ± 67 m/s), I decided to stick to theoretical values.

$$U = \left[\frac{2\gamma RT_0}{\gamma-1} \left(1 - \left(\frac{P_\infty}{P_0} \right)^{\frac{\gamma-1}{\gamma}} \right) \right]^{1/2} \quad (8),$$

where T is temperature and P pressure. The subscript 0 indicates conditions in the tube prior to decompression, while subscript ∞ indicates ambient conditions and R is the specific gas constant. In the observation window (Figure 3.1a), where particle velocities are measured, St was found to be 17-135 (Table 3.3), meaning that gas and particles are not coupled. In theoretical studies, particles bigger than 0.5 mm are not coupled with the gas phase [Woods, 1995, Carcano et al., 2013; 2014]. In the case of experiments with particles of 0.125-0.250 mm, particles should be better coupled with the gas phase. However, low particle resolution prevents direct measurement of particle velocity.

Table 3.3 Summary of the non-dimensional numbers calculated for the different experimental conditions. Theoretical Mach number (M) at vent exit, flow Reynolds number (Re) at throat, vent exit and fully expanded conditions, particle Reynolds number (Re_p) at fully expanded conditions and Stokes number (St) at fully expanded conditions. * Particle size in mm

	M		Re			Re_p		St	
	exit	throat	exit	fully expanded	1-2*	0.5-1*	1-2*	0.5-1*	
25°C									
Nozzle	1	$5.4 \cdot 10^7$	$5.4 \cdot 10^7$	$5.1 \cdot 10^7$	$2.3 \cdot 10^6$	$1.1 \cdot 10^6$	56	29	
Cylinder	1.52	$6.1 \cdot 10^7$	$7.4 \cdot 10^7$	$6.3 \cdot 10^7$	$2.2 \cdot 10^6$	$1.0 \cdot 10^6$	46	25	
Funnel 15	2.87	$6.1 \cdot 10^7$	$1.1 \cdot 10^8$	$9.6 \cdot 10^7$	$2.2 \cdot 10^6$	$1.0 \cdot 10^6$	31	17	
Funnel 30	3.69	$6.1 \cdot 10^7$	$1.3 \cdot 10^8$	$1.3 \cdot 10^8$	$2.2 \cdot 10^6$	$1.1 \cdot 10^6$	23	12	
500°C									
Nozzle	1	$1.4 \cdot 10^7$	$1.4 \cdot 10^7$	$8.9 \cdot 10^6$	$4.4 \cdot 10^5$	$2.2 \cdot 10^5$	135	68	
Cylinder	1.52	$1.5 \cdot 10^7$	$1.8 \cdot 10^7$	$1.1 \cdot 10^7$	$4.2 \cdot 10^5$	$2.1 \cdot 10^5$	114	59	
Funnel 15	2.87	$1.5 \cdot 10^7$	$2.1 \cdot 10^7$	$1.7 \cdot 10^7$	$4.1 \cdot 10^5$	$2.0 \cdot 10^5$	76	40	
Funnel 30	3.69	$1.5 \cdot 10^7$	$2.4 \cdot 10^7$	$2.2 \cdot 10^7$	$4.1 \cdot 10^5$	$2.1 \cdot 10^5$	59	29	

3.4 Particle fragmentation

The processes and results of fragmentation are not a main aim in this investigation. The low porosity (15%) of the sample implies a low energy consumption in particle fragmentation by gas expansion [Kueppers et al., 2006b]. However, I observe the formation of some finer particles and quantify it for experiments performed with original 1-2 and 0.5-1 mm particles. To quantify it, I sieve again the samples after each ejection by dry sieving and observe the changes in GSD. The sieving is not done in detail, as I am interested in seeing only how much of the original distribution is smaller than 0.5 mm after ejection. Therefore, I do not use all the sieving intervals. Holzmüller [2016] was interested in understanding the causes of fragmentations in similar to the present experiments and performed a more detailed work on the GSD. Fragmentation due to gas expansion in the particles pores is definitely the main, but not only process involved in the experiments. A secondary process is the impact of the particles with the lid on top of the tank, and to a much lesser degree, particles could experience fragmentation when falling back on the bottom plate or by particle-particle interactions. Holzmüller [2016] performed ejection experiments in a tank with reduced height (1.27 and 2.27 m) and showed that tank height exerted an influence on final amount of fines produced and had a negative correlation. The tank used in the present investigation resulted in the lower amount of fines and, therefore, fragmentation due to impact with the tank lid can be neglected [Holzmüller, 2016]. Moreover, from the videos, no breakage was observed when particles were hitting the bottom plate once fallen back [Holzmüller, 2016]. Thus,

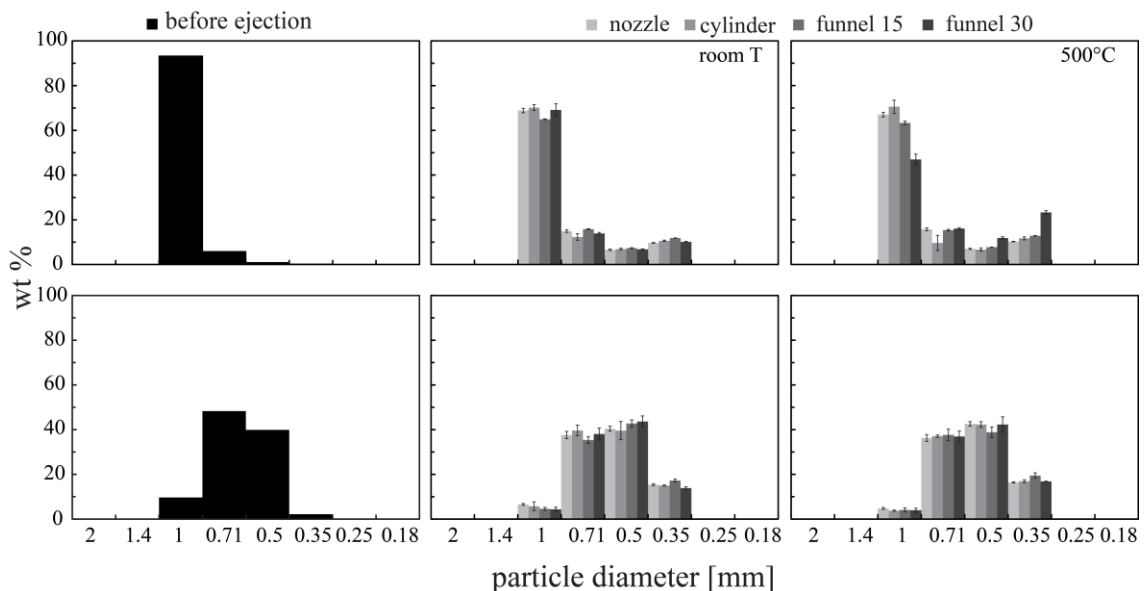


Figure 3.4 GSD before (black histograms), and after (grey scale) ejection performed with setup 2. Central histograms are for RT experiments, while the right histograms are for experiments at 500°C. The grey scale indicates the different vent geometry. Error bars indicates the difference between repetitions of the same experimental condition.

Holzmueller [2016] argued that this process could also be neglected. Regarding particle-particle interactions, I do not observe in any of the videos particles colliding with each other and resulting in fragmented pieces. This might still be happening, but I argue that it can be considered a minor fragmentation mechanism in the present experiments.

Setup 2 usually shows a higher amount of fine particles after ejection than both setup 1 and 3 and it is shown accordingly in Figure 3.4. However, setup 2 also has a larger initial particle load and therefore a higher chance of producing larger amounts of fines. Different vent geometries produce similar amount of fines, no particular control is observed. Higher temperature experiments can produce slightly larger amount of fine particles.

3.5. Particle velocity

A deliberate trigger of the rupture of the diaphragms initiates each ejection, i.e. gas and particles acceleration out of the tube. In all runs the gas, visible thanks to condensation under the illumination, precedes the first particles into the camera field of view by 1 to 5 milliseconds (ms), depending on the setup. Then, the particles are ejected over a variable amount of time and with specific patterns of changing ejection velocity and trajectory over time.

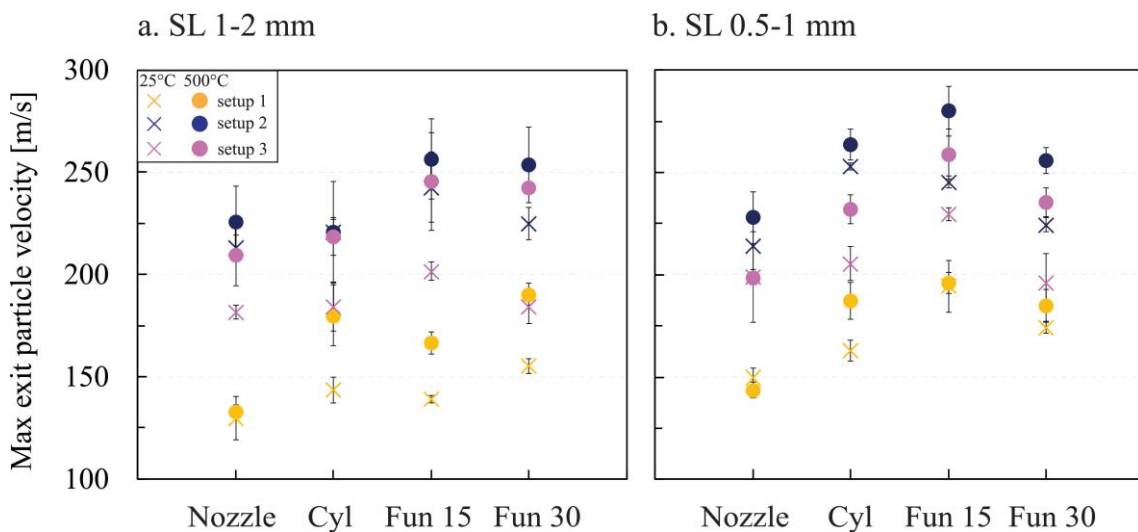


Figure 3.5 Maximum particle exit velocity plotted against vent geometry (Cyl = cylinder, Fun 15 = Funnel with 15° opening angle, Fun 30 = 30° opening angle) for particles 1-2 mm in size (a) and 0.5-1 mm in size (b). Each point and relative error bar represents the average value of velocity and standard deviation, respectively, of at least three repeated experiments at the same initial conditions. Dots are for 500°C experiments, crosses for room temperature. Error bars can be smaller than related symbol.

3.5.1 Maximum particle exit velocity (PEV)

Differences in PEV are shown as a function of tube length, vent geometry, particle load, grain size and temperature. Maximum values are always attained at ejection onset. Values range from 130 to 300 m/s and are influenced by several parameters (Figure 3.5). The strongest influence is exacerbated by the tube length, absolute values may vary by up to 80%, followed closely by particle load (up to 60%), then vent geometry (up to 30%) and temperature (up to 25%). Grain size shows the smallest apparent contribution to the particle exit velocity (up to 20%).

3.5.2 Temporal evolution of particle exit velocity

Particle ejection lasts for maximum approx. 100 ms in all experiments. After 20-30 ms, the velocity decay function is found to be asymptotic towards zero for all setups and is accordingly not shown. Figure 3.6 representatively shows the results for experiments with SL 1-2 mm particles, performed at 15 MPa, room temperature (~25 °C) and with the cylindrical vent. Time zero in the charts corresponds to the first appearance of condensed gas, which is followed by the particles with a certain delay depending on the setup (from 1-2 ms for setup 1b and 2 to 3-5 ms for setup 1). The temporal evolution of the velocity of particles during each experiment shows a non-linear decay which is strongly controlled by the particle load and tube length. Particle exit velocity at the vent decays most rapidly for setup 3 (Figure 3.6d) and most slowly for setup 2 (Figure 3.6c). The velocity decay in setup 1, 1b and 3 is well approximated by a power law equation, while in setup 2 it is better approximated by an exponential equation.

In order to compare quantitatively the results of the different geometries, their time velocity data points have been fitted with the best-fitted curve obtained for the cylindrical geometry (Figure 3.7). This way, velocity deviations caused by the vent geometry are more easily observable. In some cases, measured velocities are higher or lower compared to the cases with cylinder. In general, the temporal ejection velocity evolution is strongly non-linear for all setups with a noticeably different decay for setup 2. Setups 1, 1b and 3 are reasonably similar and show a minor influence of vent geometry. Results of setup 2 and a nozzle vent (Figure 3.7e) show the strongest variation from the other three vent geometries (Figure 3.7f-h). Overall, particle size and temperature do not affect the velocity decay trend significantly. I summarize the coefficients, fitting exponents and R^2 values for the fitting equations of experiments performed with the cylinder vent in Table 3.4. The results of experiments performed at 500°C and with 0.5-1 mm particles are in Appendix A.

Table 3.3 Summary of the best fitting equation values (coefficient, exponent, R^2) and max PEV for experiments performed with the cylinder vent and setup, temperature and GSD as listed in the table.

Setup	Temperature °C	GSD mm	Coeff. of fit equation	Fitting exponent	R2	Max PEV m/s
1	25	1-2	0.193	-1.255	0.977	144
1b	25	1-2	0.448	-1.059	0.964	220
2	25	1-2	237.4	-94.95	0.981	221
3	25	1-2	0.162	-1.121	0.985	184
1	500	1-2	0.161	-1.239	0.988	180
2	500	1-2	225.8	-97.82	0.965	221
3	500	1-2	0.145	-1.139	0.989	219
1	25	0.5-1	0.198	-1.263	0.970	163
1b	25	0.5-1	0.514	-1.053	0.927	237
2	25	0.5-1	265.0	-96.80	0.978	253
3	25	0.5-1	0.135	-1.185	0.968	206
1	500	0.5-1	0.058	-1.466	0.982	187
2	500	0.5-1	265.5	-120.1	0.971	264
3	500	0.5-1	0.094	-1.231	0.991	232

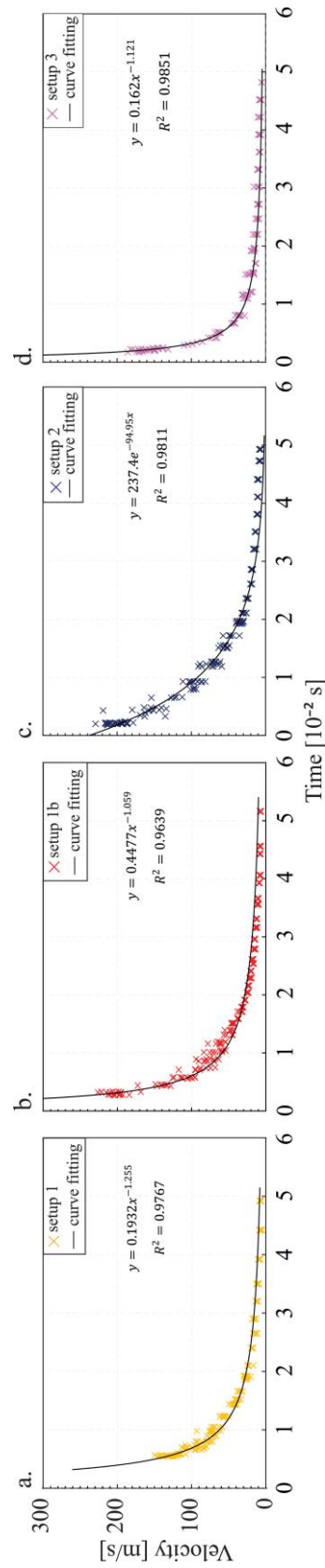


Figure 3.6 Temporal evolution of particle exit velocity at the vent for SL particles of 1-2 mm, initial overpressure of 15 MPa, 25°C temperature, cylindrical vent. a) setup 1, b) setup 1b, c) setup 2 and d) setup 3. Time zero is defined as the first appearance of condensed gas in the video, particles following after variable delay.

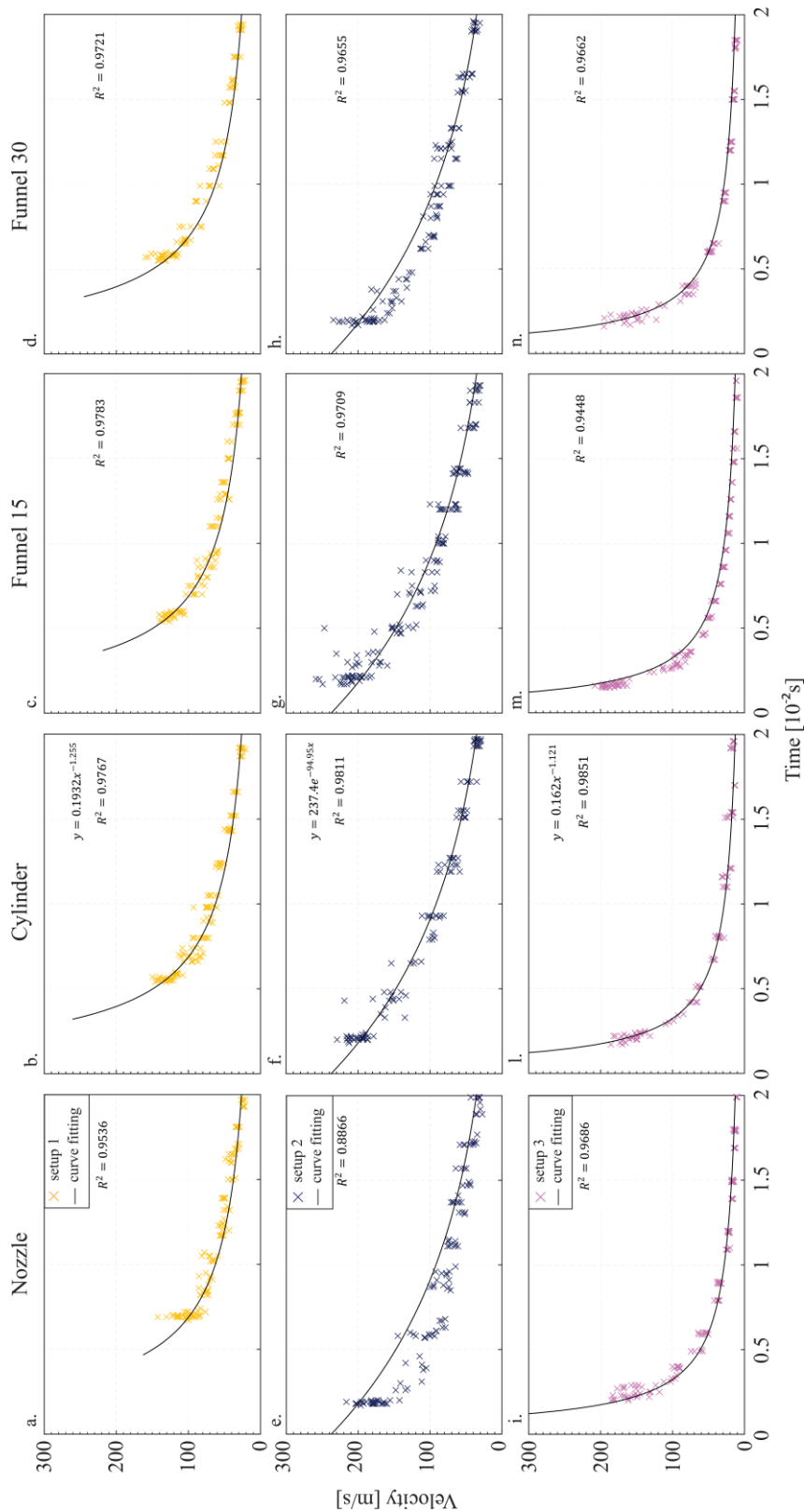


Figure 3.7 Temporal evolution of particle exit velocity shown for the four different vent geometries and the three setups (starting conditions: SL 1-2 mm particles, 15 MPa, 25°C). The best-fit curve of the cylinder geometry is superimposed on the data from the other three geometries showing the effect of vent geometry on particle velocity decay. Error bars are not plotted in this chart, but the values of standard deviation for each point are taken into account to weight the goodness of the fitting model

3.5.3 Discussion

Controlled laboratory experiments allow outlining the influence of geometrical and physical parameters on gas-particle jet dynamics. Magma inside a conduit exhibits strong horizontal and vertical gradients in its textures, mainly porosity, pore shape and permeability [e.g., Kueppers and Wadsworth, 2015]. I performed the experiments with loose fragments of monomodal GSD (Figure 3.2) with a porosity of approx. 15%. Such way, the influence of energy consumption by sample fragmentation is minor [Figure 3.4; Kueppers et al., 2006b] and the observed features can be directly related to the starting conditions as 1) geometry, 2) tube length, 3) particle load, 4) temperature and 5) GSD. Inside the tube, upon decompression, gas is expanding and accelerating in uniaxial direction. The associated gas flux inside the sample is above the value of permeable gas flow possible even in such loose particles. According to a permeability (k) model for granular material of monodisperse size distribution [Wadsworth et al., 2016], k is about $10^{-8.4} \text{ m}^2$ for particles of 1-2 mm and 10^{-9} m^2 for particles of 0.5-1 mm, respectively. Therefore, particles will be set in motion. Coupling and acceleration of particles with and by the gas scale with particle size, shape and density, and with gas flux and the residence time of the particles in a gas stream. After leaving the high-pressure autoclave from the vent, gas expansion is still axisymmetric, but no longer unidirectional; friction with the surrounding air begins to decelerate the jet and gas-particle coupling dynamics change. Overall, experiments with a converging nozzle show the lowest peak velocity values while the funnel 15 vent consistently show the fastest values of exit velocity. These trends can be explained by gas expansion dynamics. In all experiments, the gas flow is initially supersonic because of the high-pressure ratio between the overpressurized reservoir (P_r) and the external atmospheric conditions (P_e). Additionally, the vent geometry will affect the flow [see Equation 2 and Saad M., 1985; Yin et al., 2016]. The nozzle vent has an exit-to-critical-area ratio of 1. Therefore, the gas accelerates until reaching sonic conditions at the exit ($M=1$, Table 3.3). Afterwards, the gas is free to expand further. On the other hand, the cylinder and the funnel-shaped vents have an exit-to-critical-area ratio larger than 1 and the gas can expand to supersonic velocity at the exit ($M>1$, Table 3.3). However, this highly depends on the exit pressure ratio. The necessary pressure ratio is given by the Equation 2 and it depends on γ of the gas. Above a certain minimum pressure ratio, there is a positive correlation of the exit-to-critical-area ratio and M at the exit (Equation 2). The M values in Table 3 are the “designed” ones for the vent geometries in use, under the assumption that at ejection onset the pressure ratio, expressed by Equation 2, is high enough [Saad, 1985]. Stated this: the nozzle vent, with an exit-to-critical-area ratio of 1, provides $M=1$ (Equation 1, Table 3.3) if the reservoir to exit pressure ratio is at least 2, while the cylinder with an area ratio of 1.16 provides $M=1.5$ if the pressure

ratio is at least 4.2. Funnel 15 has an area ratio of 2.73, which gives $M=2.8$ if the pressure ratio is at least 26.8. Funnel 30 has an area ratio of 4.64, which means a designed M of 3.7 if the pressure ratio is at least 72. The particles do not leave the tube instantaneously at diaphragm burst, hence for the time the particles leave the tube and I can measure their velocity, the pressure ratio drops until a value that might be below the necessary one to have supersonic flow. Seeing the PEV values, I argue that the pressure ratio at particle exit from nozzle, cylinder and funnel 15 did not drop yet below the necessary one when particles exit. On the other hand, the pressure ratio from funnel 30 seems to have already dropped to a value below the necessary one and, therefore, the acceleration efficiency for this geometry is lower than, for example, the one of the funnel 15.

In addition, I can argue than for all the experiments performed with setup 1, independently of vent geometry, the pressure ratio at the vent has already dropped below supersonic conditions at the onset of particles ejection.

Temperature has a positive correlation with particle velocity. A higher temperature means that for fixed volume and pressure, a smaller amount of gas (in moles) is filling the reservoir. On the other hand, the speed of sound of the gas flow greatly depends on temperature ($c^2 = \gamma RT$, where c is the speed of sound, γ is the gas heat capacity ratio, R the gas constant and T is temperature). Accordingly, a higher temperature produces a larger speed of sound ergo particles are accelerated more even if less gas is available. Furthermore, I observe that smaller particles exhibit higher velocities than larger ones. This result can be explained by the better coupling of smaller particles with the gas flow, e.g., smaller St . Yin et al. [2016] reported similar findings for temperature and particle size effects in cold spraying empirical tests using spherical or irregular particles of metallic composition (Al, Cu), tens of μm in size.

In addition to the maximum exit velocity, the temporal evolution of particle exit velocity measured at the vent is different as a function of the initial conditions; in particular, tube length and particle load (Figure 3.7 and Appendix A). At constant particle density, size, and applied overpressure, the acceleration of the particles by drag exerted by the expanding gas phase is comparable for all four setups and quasi-instantaneous. Accordingly, the observed difference in exit velocity is a direct consequence of travel path length before leaving the vent. No significant deceleration of individual particles can be measured above the vent within the field-of-view. Consequently, the observed difference in maximum exit velocities, and the different decay curve (power law vs. exponential) is attributed to a dynamic evolution of the pressure gradient inside the shock-tube, with a negative correlation of pressure gradient and tube length. At the high-pressure gradient, the sample has no time for outgassing by permeable gas flow. Rather, the gas

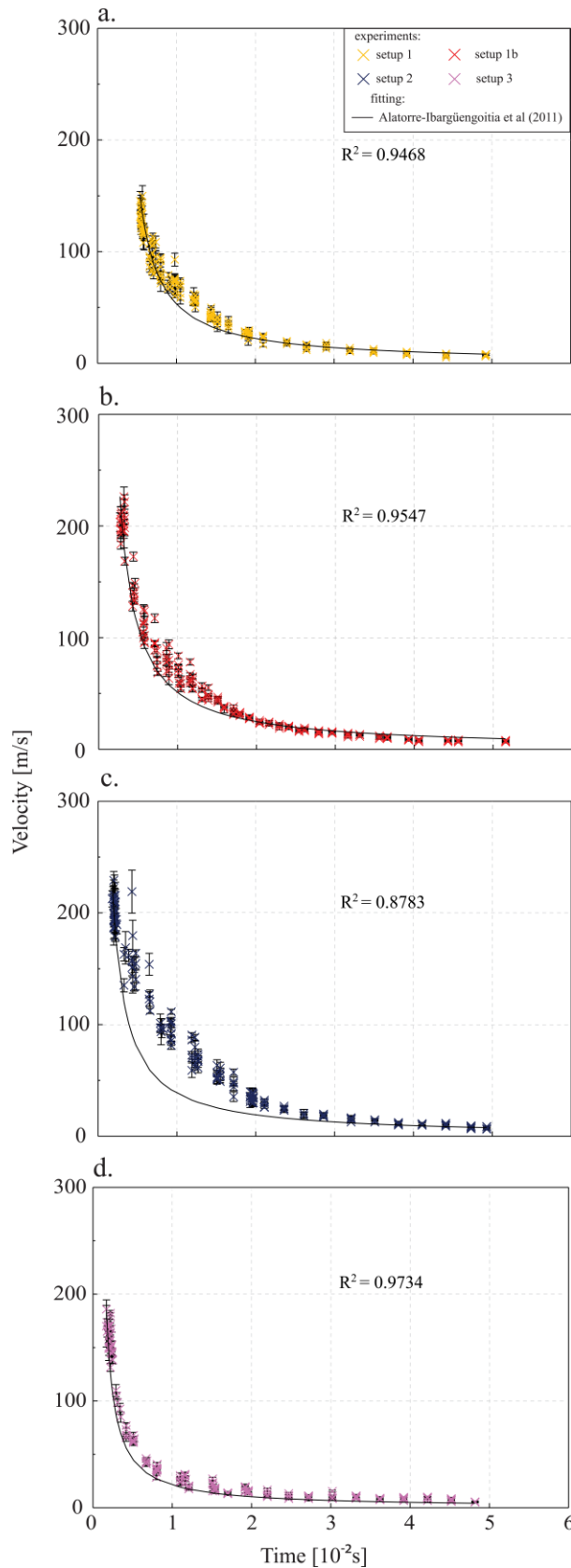


Figure 3.8 Particle velocity decay with the curve fitting from Alatorre-Ibargüengoitia et al. (2011). Error bars can be smaller than related symbol.

will set the particles in motion, thereby increasing the average particle-particle distance and bulk permeability. As a consequence, particles that are initially in the upper part of the sample will experience acceleration not only by the expanding gas that is initially “in their vicinity”, but also by gas that has been stored in the lower parts of the sample. This is clearly manifested by setup 2 and to a lesser degree (for a shorter amount of time) by experiments with 1b. Initially, gas velocity will be higher than particle velocity and consequently accelerate particles according to their shape and surface roughness. Once the gas has decompressed, particles will overtake the gas because of their inertia, as observed during Strombolian eruptions [Taddeucci et al., 2015]. Similar velocity decay trends have also been reported for pyroclast ejections on different volcanoes [Dubosclard et al., 2004; Gouhier and Donnadieu, 2011; Taddeucci et al., 2012; Scharff et al., 2015].

Moreover, I recognize a smaller but systematic influence of vent geometry on velocity decay. In order to “visualize” the results, I use the best-fit curve of the cylindrical vent, as a standard, for all four vent geometries per setup and calculated the R^2 values (Figure 3.7, Appendix A and Table 3.4).

The variations are minor for cylinder and funnel geometries, but substantial

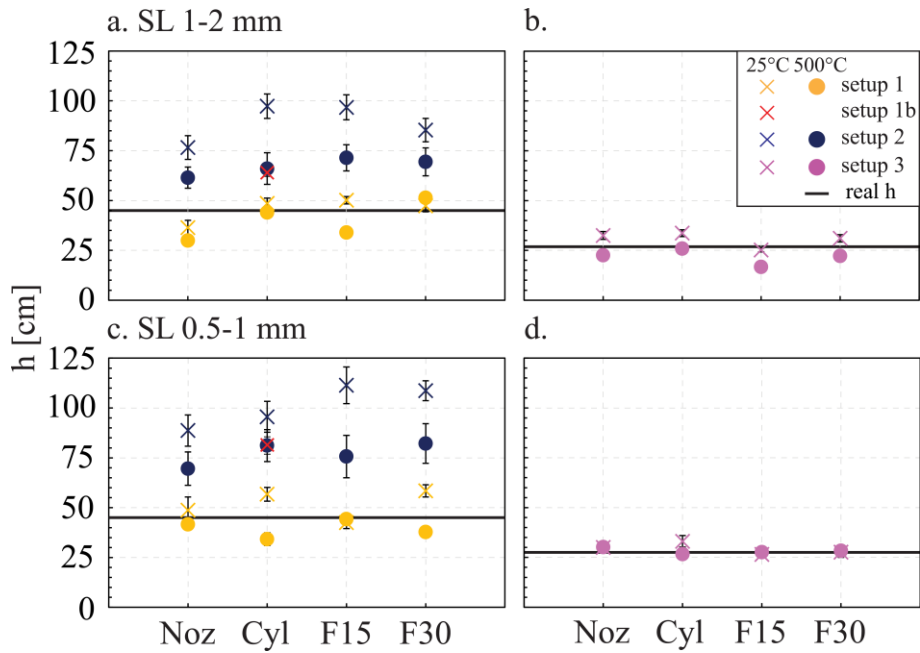


Figure 3.9 Values of h expressed in centimetre versus vent geometry for the different setups and particle size (a and b coarse fraction, c and d medium fraction). The horizontal black line is the real h (in the experiments), while the data points are the predicted h based on Equation 2. Charts b and d show a relative lower h location, this is only because in setup 3 the total length of the conduit is actually shorter, see Figure 2 for reference.

for the converging nozzle with setup 2. The latter, having a smaller critical area and therefore a smaller rate of discharge, has the strongest effect of gas expansion behaviour and accordingly particle acceleration.

Gas-pyroclast jets in nature are the first, direct observable result of the hidden process of magma fragmentation below the surface [Dubosclard et al., 2004; Gouhier and Donnadieu, 2011; Taddeucci et al., 2012; Scharff et al., 2015]. Scaled and repeatable laboratory experiments can help in shedding light on the physical processes inside a volcano. One goal is to constrain the depth of the magma surface and the effective overpressure. The observed velocity evolution of laboratory experiments was used to develop the empirical relationship expressed in Equation 3 [Alatorre-Ibargüengoitia et al., 2011].

Taddeucci et al. [2012] applied this formula to short-lived volcanic explosions (exploding gas slug in Strombolian explosions) to define the base and volume of ascending gas slugs. In the experiments, I vary the position of the base of the sample as well as particle load and I test the fitting of the results with Equation 3 (Figure 3.8). For this, I use the known h (black line in Figure 3.9) and the measured maximum ejection velocity to derive v_p . R^2 values range from relatively satisfactory (setup 1 ($R^2 = 0.9468$), 1b ($R^2 = 0.9547$) and setup 3 ($R^2 = 0.9734$)), to a substantial misfit for setup 2 ($R^2 = 0.8783$), primarily because exit velocities (between 3.5 and 23.5 ms after t_0) are significantly higher than predicted. Assuming h unknown, I use Equation 3 to calculate h based on the known velocity decay.

I find that h can be reasonably predicted for 1 and 3, while it is overestimated for setup 1b and 2 (Figure 3.9). In addition, there is no strong indication of better estimation of h with vent geometry, particle size or temperature.

In setups 1b and 2, the particle column is up to 3 times longer compared to setup 1 and 3 (Figure 3.1b). Two of the fundamental assumptions in Equation 3 are that pressure is uniform and particle velocity is constant in the conduit [Alatorre-Ibargüengoitia et al., 2010, 2011; Taddeucci et al., 2012], or, at least, that the particle acceleration phase has the same duration [Gaudin et al., 2014]. As discussed above the length of the particle-filled conduit in setups 1b and 2 is likely enough to have differences in the pressure gradient that accelerates the particles, thus pushing the system away from the applicability of Equation 3. It follows that using Equation 3 to infer eruption properties may give relative errors in h as large as 100% if the equation fit to the observed velocity decay in time shows a R^2 less than about 0.95, in particular when the misfit is towards higher than predicted velocities. However, such misfit, or, in other terms, a shift of the decay curve from a power law to an exponential function, may reveal changes of the acceleration pattern of pyroclasts during the eruption. This information is potentially important, hinting, e.g., at unsteady pressure gradients within the conduit or non-negligible effects of permeable gas flow.

3.5.4 Conclusions

I have investigated the complex dynamic processes and two-way interactions taking place in shock-tube experiments. These experiments mimic processes in the conduit and the near-vent region during explosive eruptions. Through the evaluation of empirical relationships, a better understanding of the underlying processes of directly observable, natural volcanic eruptions will be possible. The results may aid in understanding the development of buoyant eruption plumes [Tournigand et al., 2017].

Given the experimental conditions, the present results indicate that – in decreasing importance - tube length, particle load, vent geometry, temperature and grain size affect the dynamics of a starting jet. As the focus of this paper is on the dynamic evolution of particle exit velocity, the following conclusions can be drawn. Maximum PEV shows:

- 1) Negative correlation with tube length;
- 2) Positive correlation with particle load;
- 3) Positive correlation with flaring vent walls, with peaks for funnel 15;
- 4) Positive correlation with temperature;
- 5) Negative correlation with particle size.

Moreover, the temporal evolution of the velocity at which subsequent particles are being ejected shows:

- 1) The decay is non-linear and it is primarily affected by particle load and tube length. The four setups used show very different trends. Results of experiments with setups 1, 1b and 3 can be fitted by power-law equations, results of experiments with setup 2 by an exponential equation. This is related to the height of the sample inside the autoclave as the upper most part of the clasts is exposed to more permeable gas flow. Setup 3 presents the steepest velocity decay. As the smaller volume of gas and particles is located closer to the exit, the decompression is acting more rapidly. A similar relationship of particle load and decay rate of particle velocity was shown by Budilarto [2003].
- 2) Vent geometry only exert a large effect in experiments performed with setup 2 and the nozzle vent geometry.
- 3) Temperature and particle size do not exhibit large effects.

Although natural volcanic eruptions are highly dynamic and the geometry of the plumbing system undoubtedly more complex than in these experiments, the effect of boundary conditions such as tube length (=conduit length), particle load (=ejected mass) has been demonstrated to be first-order control on the ejection dynamics of particles not coupled with the gas ($St \gg 1$). On the other hand, the effect of vent geometry, temperature and GSD was found to be of second-order control at the experimental conditions I performed. For a furthering of the general understanding of eruptions, the coupling of expanding gas and particles under less regular geometries, choked-flow and smaller St number conditions deserves further attention. In that context, the fragmentation depth from where particles are being accelerated and eventually ejected is a prime goal as I anticipate that it has strong implications for the assessment of volcanic ballistic hazards.

3.6 Spreading angle

3.6.1 Initial gas and particle spreading angle

Measures of the initial gas (Figure 3.10) and particle spreading angle (Figure 3.11) are plotted against the vent geometry. Figure 3.10 shows the values of maximum exit spreading angle for the gas versus the vent geometry for the different initial GSD, coarse (Figure 3.10a), medium (Figure 3.10b) and fine (Figure 3.10c). The maximum angle commonly appears within the first five measurements, i.e., 10 frames. Vent geometry exert a large effect. For the same setup, the nozzle geometry shows commonly the largest values, followed by cylinder, funnel 15 and funnel 30; the latest two show similar values. Temperature also shows an important effect: with room temperature experiments generally showing larger values than higher temperature ones. Tube length follows, with setup 1 showing larger values than setup 2 and setup 3. Particle load and size show the smallest influence. In the experiments performed with the fine GSD (Figure 3.10c), for

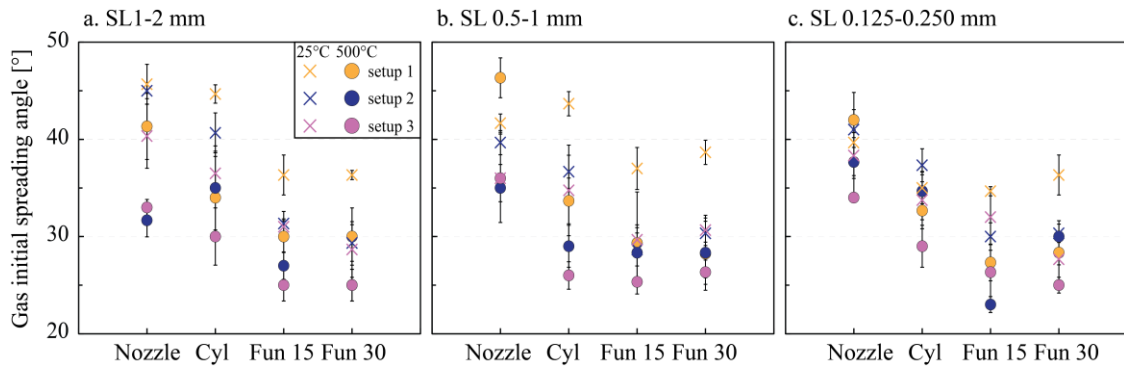


Figure 3.10 Maximum exit spreading angle for the gas plotted against vent geometry. (Cyl = cylinder, Fun 15 = Funnel with 15° opening angle, Fun 30 = 30° opening angle) for particles 1-2 mm in size (a), 0.5-1 mm in size (b) and 0.125-0.250 mm in size (c). Each point and relative error bar represents the average value of gas spreading angle and standard deviation, respectively, of at least three repeated experiments at the same initial conditions. Dots are for 500°C experiments, crosses for room T. Error bars can be smaller than related symbol.

the same geometry, the variation of maximum angles depending on a different setup is smaller than in the other two cases.

Figure 3.11 shows the initial particle spreading angle versus the vent geometry for the different initial GSD, coarse (Figure 3.11a), medium (Figure 3.11b) and fine (Figure 3.11c). In this case, the plotted angle is the very first measurement made and it does not always correspond to the maximum particle spreading angle for a certain condition. In fact, the first measurement corresponds to the maximum angle for setup 1 and most of setup 3, while in the case of setup 2 the maximum angle can appear up to 3 ms after the start of the ejection (Figure 3.12 and Figure B1 to B6 charts e to h). Particle load shows the largest effect, with setup 2 commonly displaying the largest angle values. Setup 3 and 1 can show similar results implying that the tube length does not play a large role. Particle size shows also a large effect, but the effect is enhanced in experiments with the fine fraction, while experiments with particle of coarse and medium size show similar results. Vent geometry exerts a smaller role, in particular the nozzle vent shows constantly larger values, while funnel 15 smaller ones. Temperature has a minor role; room temperature experiments can show larger values than hot experiments.

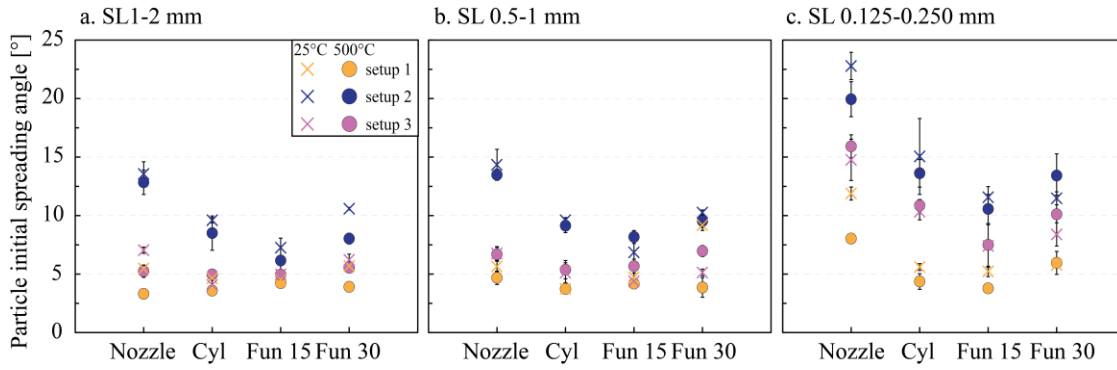


Figure 3.11 Initial spreading angle for the particle-laden jet plotted against vent geometry. (Cyl = cylinder, Fun 15 = Funnel with 15° opening angle, Fun 30 = 30° opening angle) for particles 1-2 mm in size (a), 0.5-1 mm in size (b) and 0.125-0.250 mm in size (c). Each point and relative error bar represents the average value of particle spreading angle and standard deviation, respectively, of at least three repeated experiments at the same initial conditions. Dots are for 500°C experiments, crosses for room T. Error bars can be smaller than related symbol.

3.6.2 Temporal evolution of gas and particle spreading angle

I further quantify the temporal evolution of both gas and particle spreading angle. Figure 3.12 shows an example of spreading angle evolution for both gas and particles for experiments performed at room temperature, with the cylinder vent geometry, coarse particle fraction and setup 1 (Figure 3.12a), setup 2 (Figure 3.12b), and setup 3 (Figure 3.12c), respectively. The gas spreading angle evolution, grey squares in Figure 3.12, is particularly appreciable in Figure 3.12a for the setup 1 case (see also Figure B1, B2, B3 and B4 in Appendix B). Here, the particles take up to 6 ms longer than in setup 2 and 3 to exit the vent and therefore the gas jet shows clearly the whole initial expansion up to a maximum and the sequent narrowing; when particles exit, the gas is less or not at all condensed and becomes impossible to track. In the case of setup 2 and 3, the gas is still visible and expanding while particles are coming out and can undergo further expansion sometimes showing a second peak of maximum spreading angle. In this case, and also due to turbulence, it becomes less regular and the measured left and right angles can sometimes differ largely, this is shown by a larger standard deviation of some of the points (up to $\pm 5^\circ$).

The particle spreading angle evolution greatly differ within one setup and another. Setup 1 (Figure 3.12a) commonly shows an almost linear increase of the spreading angle with time. Setup 2 (Figure 3.12b) can show an initial increase towards a maximum peak, a subsequent narrowing of the jet and then again an increase of the spreading angle starting after about 20 to 30 ms from ejection onset. Setup 3 (Figure 3.12c) behaviour falls in between setup 1 and 2, it can sometimes show a small initial peak followed by a short narrowing and then a linear increase of the angle with time.

In Figure 3.13a, the same conditions shown in Figure 3.12b are compared with experiments performed all with: 1) setup 2 and funnel 15, coarse particles and room

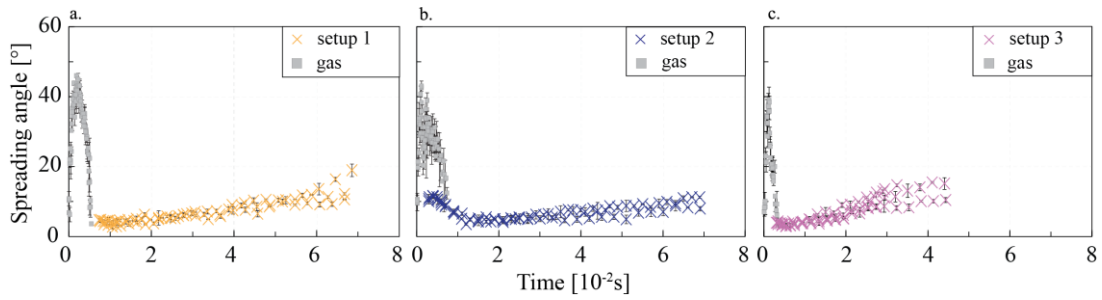


Figure 3.12 Temporal evolution of gas and particle spreading angle SL particles of 1-2 mm, initial overpressure of 15 MPa, 25°C temperature, cylindrical vent. a) setup 1, b) setup 2 and c) setup 3. Time zero is defined as the first appearance of condensed gas in the video, the particles follow after a variable delay. Error bars can be smaller than related symbol. See also video in the supplementary material.

temperature (Figure 3.13b); 2) cylinder, coarse particles and 500°C (Figure 3.13c), and 3) cylinder, fine particles and room temperature (Figure 3.13d). First, I compare Figure 3.13a and 3.13b, vent geometry is different between them, and data for funnel 15 (Figure 3.13b) show smaller initial peaks for both gas and particles and a larger degree of deviation of the particles around 35 to 60 ms. Generally, keeping the other conditions constant and varying only the vent geometry, I mainly observe two differences: 1) a change in the maximum initial value for the angle of both gas and particles (see also Figure 3.10 and 3.11); 2) a larger or smaller deviation of the particles around 30 to 60 ms. In particular, experiments with funnel 15 and 30 usually show more particles deviating at a larger angle at this time than particles ejected by the nozzle or cylinder geometry (see also Figures in Appendix B for further details). Between Figure 3.13a and 3.13c, only temperature differs. In this case, the trends look similar to one another, differing only in the initial maximum peak reached by both gas and particles. Finally, Figure 3.13a and 3.13d differ because of the initial GSD. In Figure 3.13d, the ejected fine particles commonly show a larger initial expansion than the coarser counterpart does. The very high peak for the gas spreading angle occurs during particle ejection and it can be argued that what was measured was actually the expansion of a gassy and dusty part of the particle laden jet, which expansion is also influenced by the ejection of the fine particles jet. The dusty part is usually lighter (white-greyish) in colour than the dense core particle jet, so they are discernible from one another. Experiments performed with the fine fraction commonly result shorter in time compared with the other particle fraction and might not show the later particle deviation. This is due to the fact that in these experiments, around 20 or 30 ms fine particles start already falling back and the field of view becomes easily very dusty. These conditions do not favour image analysis and if sometimes a denser particle jet is still visible (most of setup 1 cases), in the majority of setup 2 and 3 it becomes impossible to provide an accurate measure.

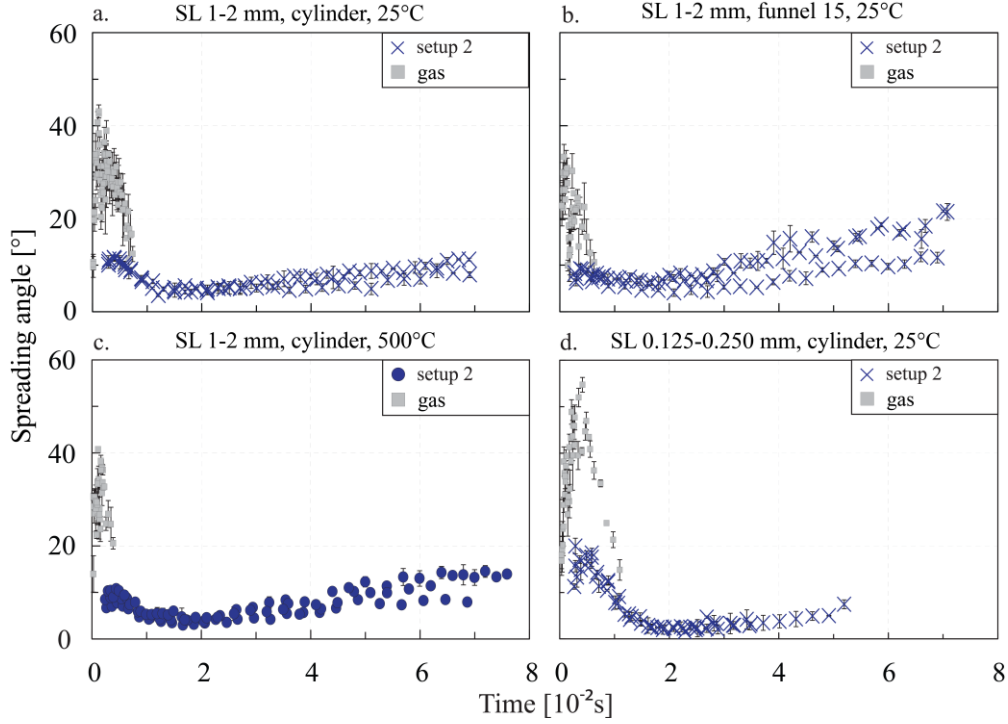


Figure 3.13 Comparison of the temporal evolution of gas and particle spreading angle for experiments performed all with setup 2 and a) coarse particle fraction, 25°C temperature, cylindrical vent, b) coarse particle fraction, 25°C temperature and funnel 15, c) coarse particle fraction, 500°C temperature, cylinder, and d) fine particle fraction, 25°C temperature and cylinder vent. Time zero is defined as the first appearance of condensed gas in the video, particles follow the gas after variable delay. See also video in the supplementary material. Dots are for 500°C experiments, crosses for room temperature. Error bars can be smaller than related symbol.

3.6.3 Discussion

At ejection onset, the gas makes the first appearance in the field of view. In all vent geometry scenarios, gas expands completely occupying the available space in the vent and it can then further expand once it has left the vent area. According to the 1D isentropic theory [Saad, 1985] the degree of expansion, i.e. the Prandtl-Meyer expansion fan, depends on γ of the gas and M number, and consequently on the pressure ratio [Kieffer and Sturtevant, 1984; Saad, 1985], and it is expressed as follows:

$$\theta = \sqrt{\frac{\gamma+1}{\gamma-1}} \tan^{-1} \sqrt{\frac{\gamma-1}{\gamma+1} (M^2 - 1)} - \tan^{-1} \sqrt{M^2 - 1} \quad (9)$$

Using M for fully expanded conditions, which from theoretical analysis results 4.39 for every geometry, θ results 52.9°. This value is higher than any of the measurements collected (Figure 3.10). The closest values are reached in experiments performed with the nozzle and cylinder vent geometries and setup 1, and they range around $46 \pm 2^\circ$. As discussed in section 3.4.3 the M numbers here calculated are for theoretical and design conditions. The real values, reached by the experimental system, can be smaller, or can actually approach the theoretical ones, but for a short and limited amount of time, which may not be resolved by the recording system. In addition, it can be argued that the early

arrival of the particles in setup 2 and 3 affects gas dynamics and it does not allow the gas to reach full lateral expansion by itself. Indeed, as shown in Figure 3.12 or 3.13, when particles exit the vent it is possible to measure a larger gas spreading angle, but these values cannot be directly related to gas expansion only and therefore they were not considered to define the maximum gas spreading angle.

Room temperature experiments commonly show larger values of gas spreading angle compared to high temperature experiments. At high temperature, the first cm of gas jet outside the vent is not always condensed and therefore the measure can be difficult to make. Taking this measuring limit into account, it can be argued that a hotter gas may respond with a less pronounced lateral expansion than a colder and denser one due to the relationship between θ and γ of the gas [Kieffer and Sturtevant, 1984].

The gas spreading angle shows a bell shape evolution with time, with an initial increase towards a maximum and a later narrowing as the pressure at the vent decreases [Kieffer and Sturtevant, 1984]. This pattern is most regular for setup 1, mainly because in this setup particles arrive up to 6 ms later than in setup 2 and 3 when particles exit only about 1.5 ms after the gas. Therefore, in the latter two cases, gas expansion is altered by the arrival of the particles; the lateral gas jet can display higher turbulence, which also reflects in larger standard deviation between measures on the right and the left of the jet.

Particle spreading angle constantly show smaller maximum values than gas spreading angle and it is firstly affected by particle load (Figure 3.12). Setup 2 commonly displays the largest angle values. This can be explained by the higher number of particles ejected, and a possible easier lateral rebounding by particle-particle interactions. Setup 3 and 1, on the other hand, show similar results, only 1° to 3° larger in setup 3 cases in experiments with coarse and medium particles, implying that the tube length does not play a great role in these cases. On the other hand, with the fine fraction, the particle spreading angle in setup 3 experiments is commonly 4° to 10° larger than setup 1, implying that in this case the tube length exerts a stronger effect. As a consequence, it is possible to say that the effect of particle size is enhanced in experiments with the fine fraction, while experiments with coarse and medium size fractions show similar results. The fine particles have less inertia and they should be better coupled with the gas phase, therefore, they are more prone to follow gas expansion and possible be more affected by gas turbulence [Sommerfeld, 1994]. On the other hand, coarse and medium particles can follow a more vertical trajectory at the beginning as they are less prone to be affected by the gas dynamics around them.

Vent geometry in general exerts a small role. The nozzle vent shows constantly larger values, while funnel 15 smaller ones, but the values of cylinder and funnel 30 show similar trends for all the other conditions (Figure 3.11). Once it is released, the particle-

laden jet, occupies the whole vent in the case of nozzle and cylinder vents; therefore, the jet diameter at ejection onset will always be as large as the vent exit diameter: 23 and 28 mm for nozzle and cylinder, respectively. In the nozzle vent, just before the exit, particles are forced to pass in a constriction and they are then subject to expansion once out. Part of the large values of spreading, especially in setup 2 experiments, may be influenced by a larger number of interactions between particles, e.g., via collisions, as numerous particles get initially deviated centrally by the vent geometry and then outward by rebounding. When particles are ejected from the funnel 15 and funnel 30 vents, they show an initial jet diameter that can be larger than 28 mm (which is the vent inner diameter before the change in walls shape occurs, see Figure 3.1 for reference). This shows that the jet is already expanding before the vent exit, but particles are then prone to follow initially more vertical trajectories.

Temperature has a minor role on particle spreading angle; room temperature experiments can show larger values than hot experiments, but the difference is more than 3° in two cases only: nozzle geometry, fine particles setup 1 and 2. The fact that room temperature experiments show a larger angle might be related to the enhanced gas expansion at room temperature that is then reflected on the particle spreading, even if at a lesser degree.

The evolution of the particle spreading angle with time (Figure 3.12, 3.13 and Figures in Appendix B) displays different patterns principally based on the setup used. Particles ejected from setup 1 experiments show the minimum initial spreading angle, compared to setup 2 and 3. In setup 1, particles initially follow a vertical trajectory, and they do not seem much affected by their neighbouring particles. Moreover, the minor spreading indicates that the initial overpressure has been mostly dissipated by the time particles exit. This is in agreement with the dissipation of gas expansion [Kieffer and Sturtevant, 1984]. A larger initial spreading is displayed only in experiments performed with the nozzle geometry and the fine particle fraction (Figure B5a and B6a). For coarse and medium particles and for any vent geometry, the initially vertical trajectory starts spreading radially about 20 ms after t_0 and particles show an increase in rotation. The same happens in the case of setup 2 and 3. Differently however is the evolution of the spreading angle with time at particle ejection onset. In setup 2, particles tend to spread radially from the beginning with a peak after 3 ms. Afterwards, once most of the particles have left the system, their trajectory tends to collimate towards a quasi-vertical ejection before starting to spread radially from around 20 ms on. In the case of setup 3 experiments, the evolution of particle spreading angle follows an intermediate path. The spreading angle is initially 1° to 10° larger than the angle in setup 1 experiments, but smaller by 2° to 7° compared to setup 2. Subsequently, it shows the “typical” quasi-vertical pattern followed by lateral spreading from around 20 ms on. The different setups are defined by particle load and

tube length, the results show that particle load exerts a larger effect than tube length on the particle spreading angle evolution.

Coarse and medium size fractions show similar spreading angle patterns independently of setup and vent geometry. Experiments performed with the fine fraction show instead greater differences. In general, the initial values are greater, up to 10° , in fine fraction experiments than in the ones with coarser particles. As mentioned above, due to their smaller size, the fine particles can also be subject to a larger effect of gas turbulence at the jet side. Moreover, experiments with fine particles display an earlier abrupt end than the coarse and medium fractions. If it is true that in the case of setup 3 the sample load is ejected almost completely in a shorter amount of time due to the small volume involved and its closeness to the exit, it needs to be taken into consideration a second factor. Generally, after 50 to 60 ms some particles can start falling back. However, in the case of the fine particles having less inertia than their coarser counterpart they start falling back earlier, already around 20 ms, and in a larger number. This leads to a sudden dimming of the field of view that does not allow a clear sight of the core jet and measurements become unreliable (Figure 3.13, Figure B5 and B6).

Experiments performed with the nozzle geometry show an initial collimation of the jet before a later additional spreading also in setup 1 cases (see for example Figure B1a, B3a, B4a and more extreme Figure B5a and B6a). Once again, this effect can be attributed to the initial constriction of the smaller exit area, and possible rebounding effects, which increase the lateral expansion. The same effect is overturned towards the end of the ejections. In fact, if initially the nozzle geometry seems to help the spreading, later on, around 40 ms the effect is the contrary and the few slow particles still being ejected are essentially less laterally deviated than in experiments with funnel 15 and funnel 30. Once particles have lost most of their momentum, a particle exiting from the funnel shaped vents with an outward deviating trajectory will not find obstacles to its path, because the walls are further away. On the other hand, results show that in the nozzle geometry, exactly because the exit is narrow, particles might interact with the walls before exit, rebound and set out slightly less deviated. This is an assumption, as it is not possible to see what it is happening inside the vent in the apparatus.

Finally, temperature modifies the initial values of the spreading angle, but it does not affect the later evolution (Figure 3.13a, and b).

3.6.4 Conclusions

I investigated the dynamics of gas and particle spreading angle, i.e. lateral trajectories in respect to a vertical centreline, in mixtures of non-coupled ($St \gg 1$) to possibly better coupled (e.g. particles of 0.125-0.250 mm) gas and particles rapidly ejected from shock-

tube experiments. The particles ejected present natural roughness, but they are always at the solid state in the experiments. This greatly differs from what it has been recently observed in some natural volcanic eruptions. Taddeucci et al. [2017] have shown that often bomb size pyroclasts are ejected while still fluidal and this greatly affect their flying dynamics. Moreover, natural meteorological phenomena as e.g. wind can influence particle trajectory, while in the experiments ambient air is still and disturbed by the ejection only.

From the experimental conditions tested, it is possible to draw the following conclusions on gas maximum initial spreading angle, in order of importance of the effect:

- 1) Negative correlation with vent geometry, i.e. for smaller exit area the angle is usually larger;
- 2) Negative correlation with experimental temperature;
- 3) Positive correlation with tube length, because a longer tube length give more time to the gas to expand before particles arrive;
- 4) Positive correlation with particle size and negative correlation with particle load. The latest two having a very small influence.

The gas spreading angle evolution with time shows a bell shape pattern and it is especially appreciable in setup 1 experiments, due to the particles later arrival. This is the only main affecting parameter.

For the particle initial spreading angle, measured as lateral spreading of the whole particle-laden jet and not of single particles, the following conclusions can be drawn, in order of importance:

- 1) Positive correlation with particle load, the more numerous particles ejected can enhance lateral rebounding effects;
- 2) Negative correlation with particle size, extremely expressed by the fine particle fraction;
- 3) Negative correlation with vent geometry, but general smaller effect.
- 4) Positive correlation with tube length and negative correlation with temperature, these two parameters exert only a minor role.

The particle spreading angle evolution with time shows patterns varying in particular with particle load and tube length. The vent geometry affects mainly the initial spreading, the maximum values, enhanced in experiments with nozzle geometry, and the final deviations, enhanced in experiments with funnel 15 and funnel 30 geometry. Experiments performed with coarse and medium particle size show very similar evolutions, while experiments performed with the fine fraction show similar trend, but much more exasperated in terms of initial maximum values and later evolution. The experiments with

fine particles are difficult to analyse after 20 ms in most of cases, it can be argued that after the collimation observable in both setup 2 and 3 (e.g., Figure B5b) particles should start deviating more lateral as in the coarse and medium size fraction cases. On the other hand, this is not visible due the falling back and sudden dimming of the field of view. The fact that the jet issues into a close tank can also be considered part of the problem. Finally, temperature exert a minor role in the spreading angle evolution.

3.7 Mass ejection rate (MER)

The quantitative measure of the MER of an eruptive event is one of the principal aims of volcanology [Mastin et al., 2009; Bonadonna et al., 2012, 2015; Gaudin et al. 2014]. I present here the preliminary results of an image analysis tool applied on videos from the “fragmentation bomb” experiments. A Matlab algorithm is developed to recognize and separate objects of different grey scale in the videos. Particles are naturally dark in colour and have been ejected in front of a light source. First, the algorithm analyses individual still frames of the high-speed videos. By defining an average grey scale threshold, single particles can be individuated from gas, neighbouring particles and the background. This threshold creates binary images (Figure 3.14), where particles are composed of black pixels and everything else is white. The black pixels are then counted and converted in area occupied by the particles. The MER is then calculated based on the temporal evolution of the particles-to-gas area ratio. The measurements take place in a rectangular

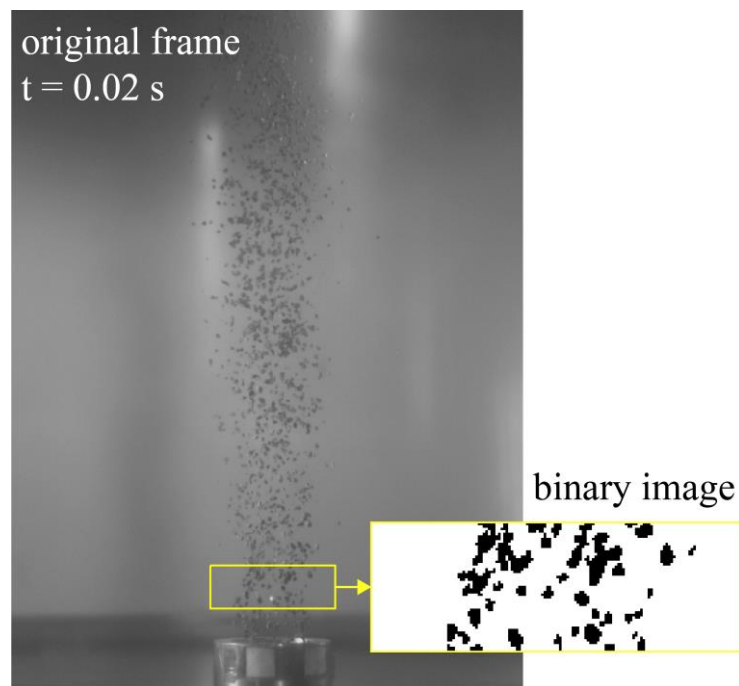


Figure 3.14 Example of original video frame with highlighted the reference window in yellow. The original frame is subject first to background subtraction, and then the window is cut and made binary resulting in the black and white rectangle. The latter is then subject to analysis for the MER calculations.

reference window (5x1.5 cm, Figure 3.14) located right above the vent exit and centrally in respect to the jet axis. Hence, it follows an Eulerian approach.

The following assumptions and limitations are taken into account for the analysis. In the videos, 3D objects are projected onto a 2D surface. In order to take into account the third dimension and the fact that particles might hide behind other particles, a conversion from pixel to particle is implemented using a correction factor obtained from a 2D simulation. In the simulation, particle concentration is randomly increased in a reference window first allowing particle superimposition, i.e. particles can hide other particles behind them, then forbidding the superimposition. The area occupied by particle results different in the two cases, and the ratio between the two areas is the correction factor. The correction factor becomes necessary when the particle concentration reaches 50% of the whole area of the reference window, i.e. correction factor > 1.5 . In addition, given the raster nature of the images, while all the pixels within a particle will be easily counted as black pixels, the contour of an object, i.e. of a particle, is composed by a certain percentage of white and black pixels. Therefore, if a certain pixel will be counted as black or white depends on the threshold applied. This obviously introduces an error, but has proven practical for the interpretation of the results. The threshold level is computed according to the method proposed by Otsu [1979].

The light conditions are found to be a major source of background noise. It is caused primarily by gas condensation, resulting in very bright or dimming particles at ejection onset, in particular in setup 2 and 3, and by high particle concentration sometimes creating a shadow in the background. If the gas noise results in possible underestimation of initially black pixels, the shadow noise can instead produce an overestimation of black pixels. Background image subtraction helps removing some of the noise caused by both problems. Different threshold level for background subtraction were tested, a value of 128 is found to give the best results. In addition, a filter is applied to avoid counting random single black pixels, which do not represent particles, commonly composed by several pixels. Finally, the MER is calculated using two main assumptions. First, the initial conversion from black pixel area to area occupied by particles. To do this, at every time step the total area occupied by black pixels is multiplied by the mean particle diameter (e.g., 1.4 mm for experiments performed with 1-2 mm particles, see Figure 3.2 for reference) and particles are assumed spherical. This area is then converted in particle mass. From the mass, the MER is obtained, using the classic continuity equation, multiplying by particle velocity and dividing by the height of the reference window. In this way, the overestimation due to a single slow particle that takes more than one frame to exit the reference window is scaled and corrected. The particle velocity factor is applied

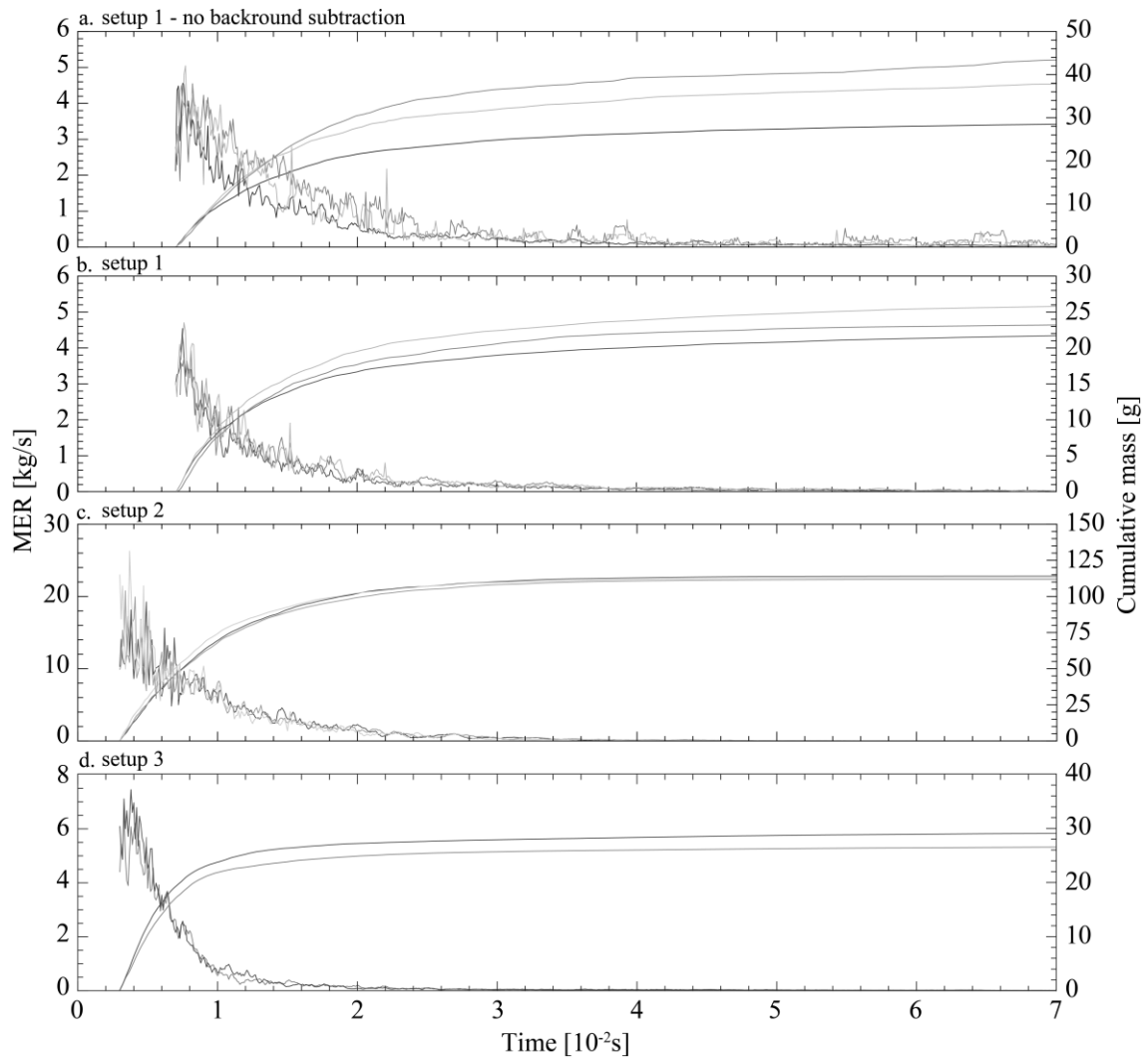


Figure 3.15 Diagrams showing MER and cumulative mass obtained from experiments performed with cylinder, room temperature and 1-2 mm particles for setup 1 (a and b), setup 2 (c) and setup 3 (d). Chart a. shows the results for videos analysed without background subtraction and displays higher data scatter. Chart b. shows the same conditions of chart a, but the analysis is performed after the videos are processed with background subtraction. It resolves in less data scattering compared to chart a. In addition, charts c. and d. are results from videos processed with background subtraction. The different grey scale are for different repetitions of the same experimental conditions.

using the best fitting equation of the measured evolution of particle velocity with time (see section 3.5.2). The results obtained consist in the evolution of the MER with time (Figure 3.15); by integrating the latter, the cumulative mass (Figure 3.15) and the instantaneous mass (Figure 3.16) or instantaneous particle fraction are also calculated.

The calculation of the MER results affected by the choice of threshold and background subtraction. The MER calculated from videos where background subtraction is not applied results in a higher data scattering (Figure 3.15a) than the one from the same videos with background subtraction applied (Figure 3.15b). This is attributable to higher noise in the original videos that is smoothed by image post-processing, i.e. background subtraction application. The MER values for setup 2 generally displays the highest peak

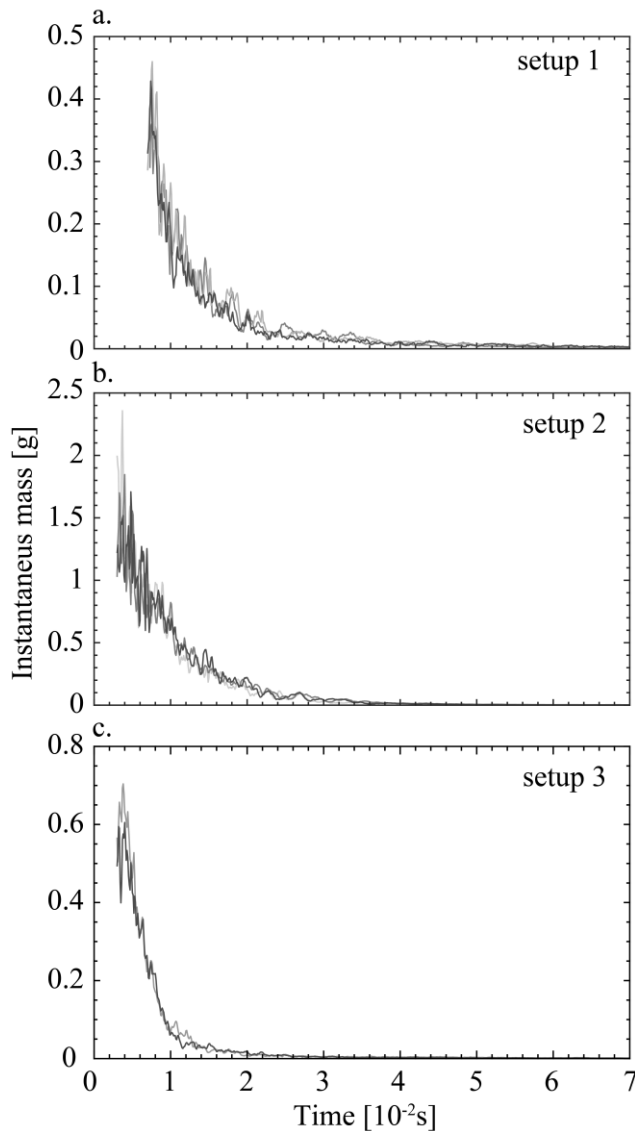


Figure 3.16 Charts showing the instantaneous mass calculated from the integration of the MER. From these results, it is possible to determine particle fraction or particle concentration at different time steps. The different grey scale are for repetitions of the same experimental conditions.

MER and instantaneous mass curves can be observed at ejection onset, representing higher initial particle concentration, but also later in the evolution. The latter can be usually related to clustering of particles.

The algorithm needs further testing and a more precise error estimation, but these preliminary results look promising. Quantifying particle concentration at vent exit or any other location along the jet axis with high degree of accuracy can provide insightful information about the starting conditions, gas-particle dynamics, turbulence and clustering of particles. In nature, the strongly dynamic mass eruption rate has been repeatedly observed and quantified but so far, volcanology has not been able to relate this

values with 26 kg/s (Figure 3.15c), as it would be expected due to the larger number of particles involved. Setup 3 follows with 7 kg/s and setup 1 with 4.6 kg/s. In addition, the evolution of the MER with time reflects the evolution of particle velocity with time. For example, setup 3 shows the steepest curve (Figure 3.15d) in good agreement with particle velocity trends reported in section 3.5.2. In general, the cumulative mass retrieved results underestimated by up to 18% (setup 2) in respect to the original mass deployed in the experiments. Figure 3.16 shows the instantaneous mass evolution with time giving an idea of particle concentration at different time steps for the three setups. Particle concentration is highest for setup 2, followed by setup 3 and setup 1. Setup 2 shows also higher data scattering at ejection onset, which could be partially associated to noise due to larger amount of condensed gas that is not properly removed by the image processing. Peaks in the

to starting conditions as gas overpressure, fragmentation depth or efficiency or conduit processes. Particle clustering has commonly been attributed to the relative motion between particles and gas phases and consequent inertial instabilities, as well as to interaction between particles [Agrawal et al., 2001]. It could be of interest to expand the investigation on the particle clusters by analysing their frequency of appearance and size depending on the different conditions.

3.8 Electrical discharges

Volcanic lightning is a marvellous phenomenon largely observed and described in literature since long time and consequence of plume electrification. Already *C. Plinius Caecilius Secundus*, better known as Pliny the Younger, in his second letter to his friend *Tacitus* about the 79 A.D. eruption of Vesuvius, Italy, wrote “*ab altero latere nubes atra et horrenda ignei spiritus tortis vibratisque discursibus rupta in longas flammaram figuras dehiscebat: fulguribus illae et similes et maiores erant*”. The phrase can be translated as “on the opposite side, a horrible, black-faced cloud, torn by fire-stricken arrows, came precipitously forward, opening into large flares of fire: these were similar to lightning, but extraordinarily bigger”. Hence, their description is indeed old, and since then the observations of the phenomenon have been increasing with passing time together with a development of the investigation techniques [Anderson et al., 1965; Behnke et al. 2010; Aizawa et al., 2016; Cimarelli et al., 2016; Van Eaton et al., 2016]. On the other end, the full understanding of the physics behind their generation mechanism still debated [McNutt and Williams, 2010; Méndez Harper and Dufek, 2016]. Complex interactions between the different eruption source parameters (e.g., fragmentation processes, magma properties and therefore relative gas and pyroclast characteristics, eruption energy and ejection dynamics) as well as environment conditions influence the exchange and segregation of electric charges in the eruptive plume, and consequently the occurrence or not of lightning [Méndez Harper and Dufek, 2016].

Electric discharges have been observed in particle-laden jets generated with a similar to the present shock-tube apparatus [Cimarelli et al., 2014]. Cimarelli et al. [2014] used the combination of a high-speed camera, to record the ejection, and two ring antennas made of copper at the vent exit to measure the electric potential. They concluded that there is a relation between discharges and amount of fine particles and that particle clustering may be effective in distributing the charge [Cimarelli et al., 2014].

In the present experiments, electric discharges are not a main aim of the investigation. No antennas are employed on the system, but electric discharges are observed in the videos. From the observations, I compiled a summary of the present experimental conditions that favour or not the generation of electric discharges. A limitation of the visual observation

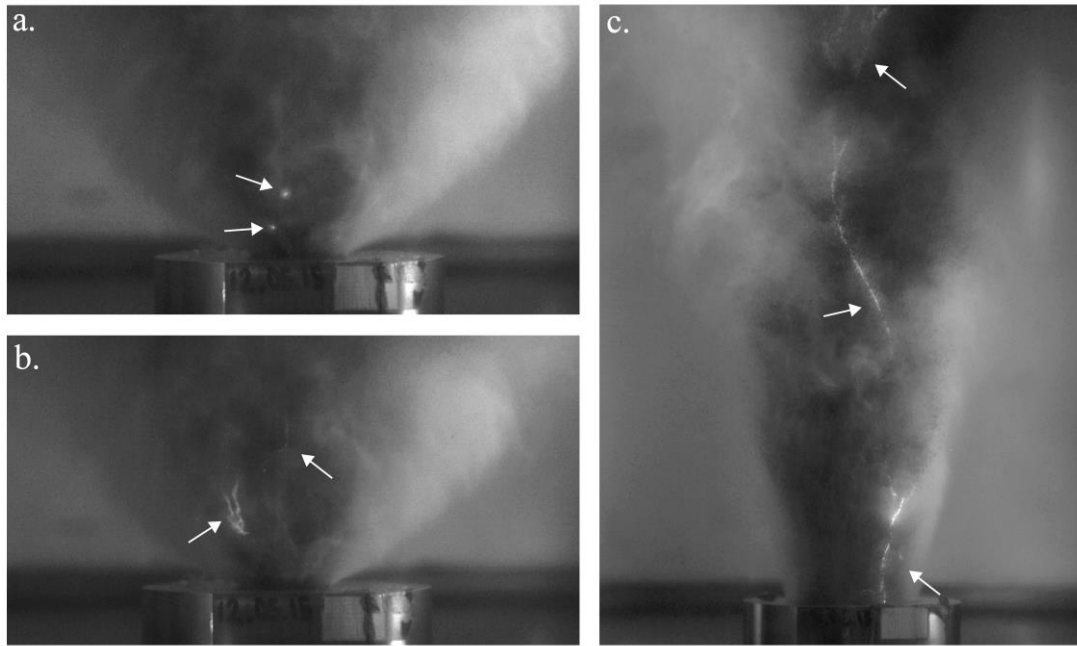


Figure 3.17 Image a. shows millimetre size sparks close to vent exit from an experiment performed with fine particles, room temperature, setup 2 and nozzle vent. Image b. shows centimetre size lightning close to vent exit from an experiment performed with fine particles, room temperature, setup 2 and nozzle vent. Image c. shows up to 20 cm long (could be longer as the upper ending part is not clearly visible) lightning from an experiments performed with fine particles, room temperature, setup 2 and funnel 15 vent.

is that the combination of recording frame rate and exposure, in this case 10000 fps and $4 \mu\text{s}$, respectively, is very likely not fast enough to record every discharge in the experiments. Moreover, I film only one side of the jet, therefore, if a lightning occurs on the opposite side and it does not cross the jet: it is not going to be visible. Still, it is clear that certain experimental conditions are favouring the generation of more lightning than others are. The electrical discharges in the experiments appear like small, millimetre size sparks (Figure 3.17a) and longer, centimetre size lightning (Figure 3.17b). I observe only in two experiments three lightning occupying the whole field of view in the vertical dimension, therefore, about 20 or more cm long. These three are the longest ever observed in the experiments and they are observed in experiments performed with fine particle fraction, room temperature, setup 2 and funnel 15 vent geometry (Figure 3.17c). All the discharges are visible only in one frame of the video. Their propagation is never visible and the majority appears at ejection onset, when overpressure is still high [Cimarelli et al., 2014], even thou in the case of experiments with fine particles, some discharges can be seen up to 10 and maximum 20 ms after the beginning of the ejection.

Table 5 summarizes the observations regarding both the number of experiments where lightning are observed as well as how many lightning are counted depending on setup, GSD, temperature and vent geometry.

Particle load has positive correlation with number of lightning observed and shows the largest effect, while tube length has a negative correlation, but a smaller effect. The experiments performed with the fine particles are also displaying the highest number of lightning, while coarse and medium show a similar trend. Temperature has a negative correlation, and I observe a larger number of lightning in room temperature experiments, even if the total number of experiments with lightning occurrence at room temperature is close to, but less than the ones at high temperature. For an equal number of experiments with lightning occurrence for the different vent geometries: the nozzle geometry displays a larger of single flashes. Cylinder, funnel 30 and funnel 15 follow, in decreasing importance.

Table 3.4 Summary of the number of experiments with visible electrical discharges, i.e., lightning. *percentage of number of experiments with lightning on the number of experiments performed with different conditions (setup, GSD, temperature, vent geometry).

Setup	n° of experiments	n° of experiments with lightning	% per condition*	n° of lightning
1	73	2	2.7	7
1b	4	3	75.0	9
2	72	58	80.6	464
3	75	31	41.3	114
GSD				
coarse	77	26	33.8	51
medium	75	27	36.0	60
fine	72	41	56.9	483
Temperature				
25°C	115	44	38.3	415
500°C	109	50	45.9	179
Vent geometry				
Nozzle	54	22	40.7	253
Cylinder	61	28	45.9	147
Funnel 15	54	22	40.7	90
Funnel 30	55	22	40.0	104
Total n° of exp	224	94		594

Page intentionally left blank

4. Jet Buster

In this chapter, I present the “jet buster” system, the experiment performed and main findings related to gas and particles dynamics obtained via image analysis of high-speed videos and microseismic signals.

4.1 The experimental apparatus

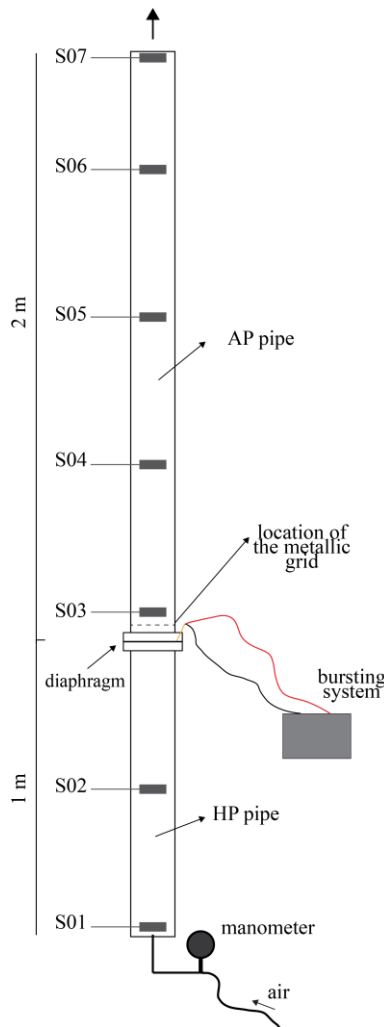
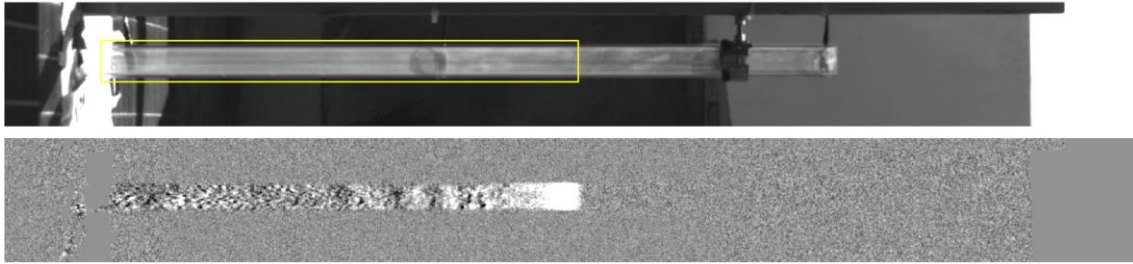


Figure 4.1 Schematic diagram of the “jet buster” not to scale. From bottom to top the manometer to control the air pressure in the HP pipe, the diaphragm and the bursting system. The relative position of the metallic grid and the AP pipe on top. The sensors (S01, S02, etc.) are located at approximately 50 cm one.

I performed a series of experiments at the high pressure – high temperature laboratory of INGV in Rome, Italy. The experimental facility was originally created to study the dynamics of Taylor bubbles, i.e., slugs, rising in a conduit and then bursting [Taddeucci et al., 2013]. The experimental apparatus is located outside of the laboratory building. During the experiments, the average atmospheric conditions were the following: 27.5°C, 45.5% humidity, 1015 hPa.

The system is comprised of a 3 meters height PMMA cylindrical transparent pipe (Figure 4.1). The external diameter is 50.09 mm and the thickness 5.14 mm. The long pipe actually consists of two connected pipes: the first pipe is of one meter height and can be pressurized with compressed air (HP pipe in Figure 4.1); the second pipe is on top of the HP pipe, is two meters long, and is open at the end to be at atmospheric pressure (AP pipe in Figure 4.1). The pressure is controlled with a manometer connected to the bottom of the lower pipe. A circular plastic membrane made from commercial binding sheet about 0.75 mm thick, separates the HP and AP pipes (diaphragm in Figure 4.1). This membrane lays on top of a constantan alloy wire connected to the buster electrical box: a controlled short circuit burns the wire that subsequently cuts the plastic membrane and starts the ejection. When performing experiments with loose particles, a fine metallic grid with voids < 0.5 mm is placed 5.4 ± 0.4 cm above the diaphragm. This grid

t = 0.8483 s



t = 0.8498 s

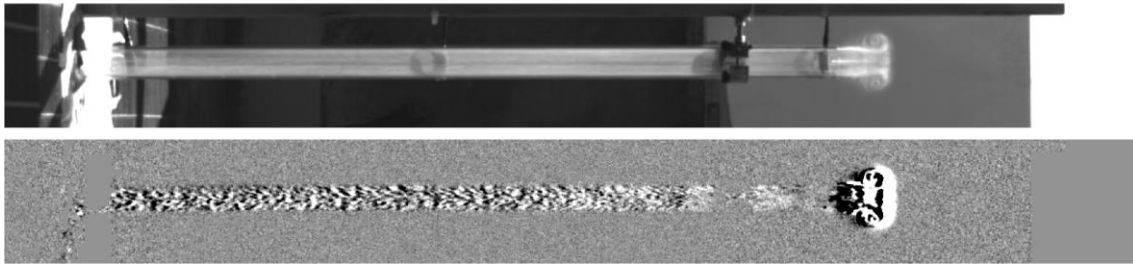


Figure 4.2 Example of two single frames from the original recording of experiment GAS and after background subtraction on the upper pipe. In the first image from top, inside the yellow rectangle, the gas mixed with the kaolin is partly visible, i.e., the pipe in the rectangle is more opaque than in the part right above. It becomes better visible after background subtraction in the image below. The second couple of images show the same experiment few frames later. The gas exits the pipe and creates a vortex ring. Once again, the background subtraction enhances the recognition of gas motion. Images are originally vertical.

prevents fine particles from having direct contact with the diaphragm, which would affect its ability to open.

Seven high-dynamic piezoelectric film sensors are spaced about every 50 cm along the pipe, from bottom to top (S01, S02, etc. in Figure 4.1). The sensors record the elastic response of the system and the jets' dynamics at a sampling rate of 500 kHz. Additionally, the experiments are filmed with two high-speed cameras, a NAC HX3 and a NAC HX6, both at a sampling rate of 17000 fps, with a resolution of 1920x168 and 1536x168, respectively. The HX3 camera records the lower part of the AP pipe, from the diaphragm up to approximately one meter and below S05. The HX6 camera is placed above on a metal walkway and records the upper part of pipe (Figure 4.2) from S05 to exit, and about 30 to 40 cm above the vent exit. In the lower part, a spotlight is used to illuminate the pipe, while the upper part is illuminated by sunlight. The videos are analysed to estimate air-particle mixture velocity. The air propagation is measured using an automated image analysis algorithm running over images with subtracted background. A pinch of kaolin is dropped in the pipe, which along with the presence of sunlight in the upper pipe, allows the gas to appear whitish and particularly visible (Figure 4.2). The algorithm measures the displacement of pixels with a certain colour moving upward with time, from which it is then possible to measure the propagation velocity of the front flow. The particles' velocity can be resolved with the same algorithm, however for comparison, I also perform manual tracking of single particles with MTrackJ at different locations in the pipe. I track

up to a hundred particles passing through selected locations following them for 5 consecutive frames. As the cameras and piezoelectric sensors are synchronized to trigger together, it is possible to compare data.

The following experimental conditions are tested and are also listed in Table 4.1.

- 1) Two kind of particles are used--kaolin and Schaumlava (the same particles used in the experiments with the “fragmentation bomb”--see section 3.1 of this thesis). The kaolin powder has a mean diameter of 20 μm measured with laser refraction analysis using the Coulter $\text{\textcircled{R}}$ LS230. The kaolin is used in two cases (experiment GAS and GASM) to make the gas visible and thus only a pinch (about 0.07 grams) is used. In these two experiments, the goal is to observe just the gas dynamics and characterize the elastic response of the jet buster under these conditions. On the other hand, in experiment KAOL, I test the response of 7 grams of kaolin. The Schaumlava (SL) particles are sieved wet and separated in the following three GSD: coarse 2-4 mm (PARTC), medium 1-2 mm (PARTB), and fine 0.5-1 mm (PARTA). The experiments with SL particles always involve about 15 grams of particles plus a pinch of kaolin to enhance gas visibility.
- 2) The overpressure in the HP pipe was 2 bar (i.e., 0.2 MPa; gauge pressure) in all the experiments presented here and the pressurized air fills the entire volume of the HP pipe: $1.2 \cdot 10^3 \text{ cm}^3$. The gas used is always compressed air.

Table 4.1 Summary of the experimental conditions used. The table lists the experiment label, if the metal grid is used or not, the sample and its GSD (* mean diameter for the kaolin), particle load, applied pressure, and the volume of compressed air. The particle load for the first experiment is not measured, but it can be assumed to be of the same quantity as the second experiment, as in both cases just a pinch of kaolin is dropped in the pipe to enhance gas visibility.

experiment	metal grid	sample	GSD [mm]	particle load [g]	applied P [MPa]	Gas volume [cm ³]
GAS	N	kaolin	0.02*		0.199	$1.2 \cdot 10^3$
GASM	Y	kaolin	0.02*	0.0689	0.205	$1.2 \cdot 10^3$
PARTA	Y	SL	0.5 - 1	15.33	0.202	$1.2 \cdot 10^3$
PARTB	Y	SL	1 - 2	15.40	0.200	$1.2 \cdot 10^3$
PARTC	Y	SL	2 - 4	15.22	0.205	$1.2 \cdot 10^3$
KAOL	Y	kaolin	0.02*	7.22	0.201	$1.2 \cdot 10^3$

Unlike in the “fragmentation bomb” (see chapter 3 for reference), in the “jet buster” system, the compressed volume of air initially rests in the HP pipe below the particles, which are located in the AP pipe. When the membrane breaks, the gas decompresses upwards and sets the particles in motion. Since the pipe is transparent, it is possible to

follow the particles from the bottom to the exit and the full acceleration and deceleration dynamics can be appreciated. Here I present experiments performed with 2 bar. The membrane dividing the HP pipe from the AP pipe is made of thin plastic and breaks easily under pressure, making it difficult to reach higher pressure levels. The maximum overpressure tested is 8 bar, related results are out of the scopes of the present investigation.

4.2 Static analysis of the HP pipe

I estimate the stress under static conditions in the HP pipe prior to decompression in order to understand to which stresses the PMMA pipe is subject to during the compression phase. These properties determine the elastic response of the PMMA pipe and are thus important to interpret the observations made. The properties of the PMMA pipe are listed in Table 4.2. The material properties are retrieved from the commercial information sheet of the producer.

Table 4.2 PMMA pipe properties. Inner and outer diameter and thickness were personally measured. The material properties come from the commercial information sheet for the PMMA pipe.

PMMA pipe properties	
inner radius, r_i [mm]	19.91
outer radius, r_o [mm]	25.05
thickness [mm]	5.14
Poisson ratio, ν	3.75
elastic modulus, E [MPa]	3200
max tensile yield stress [MPa]	72
max compressive yield stress [MPa]	103
thermal expansion coefficient from 0 to 50°C [1/°C]	$7 \cdot 10^{-5}$

The ratio between the pipe thickness and the internal diameter is 1/8; therefore, the stress can be solved using the Lamé's theorem for thick walled cylinders [Lamé, 1852; Arciniega-Ceballos et al., 2015]. The main assumption of this theorem is that the axial strain (ε_L) along the pipe length is constant, meaning that along the longitudinal axis any section of the cylinder will remain planar before and after the application of pressure in the pipe. Moreover, the longitudinal stress (σ_L) is also assumed constant and neglected at any point away from the pipe extremities. Additionally, thermal expansion is assumed to be negligible: while the system was tested outdoors, the HP pipe is never exposed to direct sunlight. Therefore, the main variables are the stress and the strain in the radial (σ_R , ε_R , respectively) and in the tangential (σ_T , ε_T) directions. The HP pipe is pressurized inside,

therefore, the internal pressure (P_i) is taken as an experimental variable, while the external atmospheric pressure (P_o) is considered equal to zero.

Given that σ_L is constant, that P_i is known (0.2 MPa), and that $P_o = 0$, it is possible to define the following parameters:

$$a = \frac{P_i r_i^2}{r_o^2 - r_i^2} \quad (10), \text{ and}$$

$$b = \frac{P_i r_i^2 r_o^2}{r_o^2 - r_i^2} \quad (11).$$

It follows that:

$$\sigma_R = a - \frac{b}{r^2} \quad (12),$$

at any radius r in the pipe wall, with maximum $\sigma_R = -P_i$ when $r = r_i$, with a negative sign on P_i indicating compressive radial stress. The tangential stress is:

$$\sigma_T = a + \frac{b}{r^2} \quad (13),$$

for any radius r of the pipe wall and it is at its maximum for $r = r_i$.

Since σ_L is neglected, the radial and tangential strains are obtained from the related stresses according to Hook's law as follows:

$$\varepsilon_T = \frac{1}{E} (\sigma_T - \nu \sigma_R) \quad (14),$$

$$\varepsilon_R = \frac{1}{E} (\sigma_R - \nu \sigma_T) \quad (15).$$

Thus, the radial displacement at any radius r in the pipe wall is expressed as follows:

$$\delta r = \frac{r_i^2 r P_i}{E(r_o^2 - r_i^2)} \left[(1 - \nu) + (1 + \nu) \frac{r_o^2}{r} \right] \quad (16).$$

Finally, the maximum shearing stress is obtained from:

$$\tau_{max} = \frac{(\sigma_T - \sigma_R)}{2} = \frac{P_i r_o^2}{(r_o^2 - r_i^2)} \quad (17).$$

With a P_i of 0.2 MPa, τ_{max} for the pipe used (see radii in Table 4.2) is 0.54 MPa while the values of stress, strain, and radial displacements are summarized in Table 4.3.

Table 4.3 Summary of the theoretical calculated tangential and radial stress and related strain and radial displacement at different radii of the pipe wall. Mid radius means the radius in the middle of the pipe wall; refer to Table 4.2 for details. Stress, strain, and displacement are higher on the inner radius.

	Tangential stress [N/cm ²]	Tangential strain	Radial stress [N/cm ²]	Radial strain	Radial displacement [μm]
inner radius	89	3.00*10 ⁻⁰⁴	-20	-1.66*10 ⁻⁰⁴	5.98
mid radius	77	2.50*10 ⁻⁰⁴	-8	-1.16*10 ⁻⁰⁴	5.47
outer radius	69	2.14*10 ⁻⁰⁴	0	-0.80*10 ⁻⁰⁴	5.62

4.3 Gas-particle dynamics and the elastic response of the system

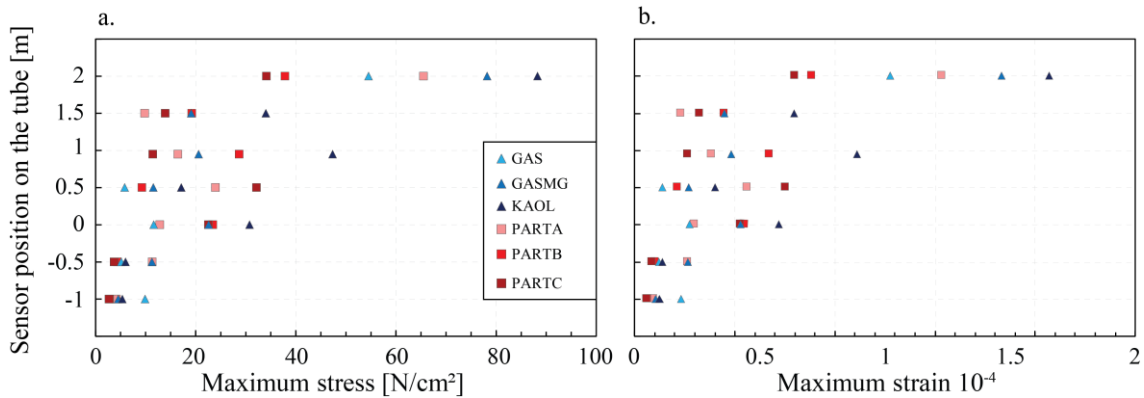


Figure 4.3 Chart a. displays the trend maximum stress [N/cm^2]; chart b. displays maximum strain. 0 (zero) on the y-axes represents S03, which is the closest sensor to the diaphragm and, therefore, it is taken as reference point. -1 represent sensor S01 while the value 2 represents sensor S07.

Like in a shock-tube system, when the diaphragm bursts, a shock wave propagates upward in the AP pipe, while expansion waves travel downward through the HP pipe [Arciniega-Ceballos et al., 2015]. The wave field related to the gas-particle mixture dynamics is complex as can be observed in the videos. However, the piezoelectric sensors recorded all kind of waves at 500 kHz that can be considered like microseismic signals of the pipe [Arciniega-Ceballos et al., 2014]. The waves' propagation depends on the properties and geometry of the medium through which the waves travel. Whether the metallic grid is present and the particle size distribution and their properties may cause some effect on the waves' propagation. Following Arciniega-Ceballos et al. [2015], the maximum stress (Equation 17, Figure 4.3a) is obtained from the maximum amplitude recorded at each sensor and normalized by the sensor area after the instrument correction. Thus, the values reported in Figure 4.3 are for the different sensors at different times, according to wave arrival and related maximum amplitude. The highest stress values are usually observed related to S07 (Figure 4.3a), the sensor at the pipe exit. In addition, the maximum strain is calculated from the maximum stress (Equation 15, Figure 4.3b). Stresses and strains show a trend on S07 depending on the sample type and particle size. KAOL shows the highest values. Between GAS and GASM, the difference is due to the presence of the metal grid in the second experiment. In this case, the maximum stress and strain are higher for GASM than GAS. In the experiments with SL particles, PARTA (0.5-1 mm) shows higher values than PARTB (1-2 mm), which shows slightly higher values than PARTC (2-4 mm). On the other sensors, the same trend (or any other trend) is not observed. The smallest values of stress and strain are recorded on S01. In all charts, the values for S05 and S06 in the GAS experiments are missing because of sensor saturation.

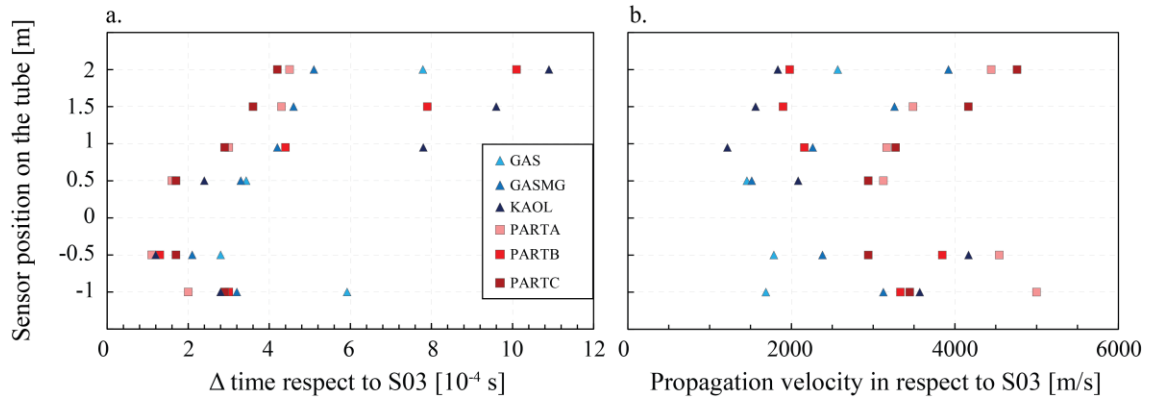


Figure 4.4 This figure shows a. the Δ time of the first arrival of the wave propagation in respect to sensors S03 (0 on y-axes), which is taken as reference, and b. the related calculated propagation velocity obtained dividing the sensor distance from S03 by the arrival time.

The wave propagation velocity (Figure 4.4b) is calculated using the times of first arrival (Figure 4.4a) of the waves at each sensor and the distances between the sensors and sensor S03. S03, indicated with 0 (zero) on the y-axes, is the closest to the diaphragm and is therefore chosen as the reference point. In this case, the propagation velocity in experiment GAS usually shows lower values than in the other cases. In the experiments with particles, experiment PARTC (2-4 mm) shows faster values of wave propagation velocity, followed by PARTB (1-2 mm), and finally, PARTA (0.5-1 mm).

Thanks to the addition of kaolin, the gas propagation inside and outside of the pipe is observable on the videos and it can be compared with the signals from the sensors. Figure 4.5 shows one example of the combination of a “chronoplot”, obtained from the automated algorithm, with signals from the sensors S07 (at exit) and S03 (above the diaphragm), for the experiment GAS. The signals’ amplitude is normalized to their own maximum amplitude, i.e., they are plotted in arbitrary units. From left to right in the image there are first two original frames showing the lower and upper part of the AP pipe as recorded by the two cameras before the diaphragm burst. Then the two graphs obtained from the algorithm, for the respective parts of the pipe that appear graphically separated. The chronoplots have units of time in seconds on the x-axes, and height in meters on the y-axes. The height corresponds to the pipe height as shown in the images from the camera. In the lower part, 0.2 m corresponds to the location of the diaphragm and the tracking of the propagation of the front flow starts from there. In the upper part, the pipe exit corresponds to 1.4 m on the chronoplot. The thick, inclined lines correspond to gas propagating upwards (due to acceleration) and downwards (due to counter flow) (Figure 4.5 upper chronoplot) in the pipe and outside. The steeper the inclination of the lines, the faster the propagation. The upper pipe is brighter thanks to the sunlight; this allows for better observations of the dynamics. Hence, first a 507 m/s gas-particle (kaolin) mixture front can be observed rising up to the exit, where it then creates a vortex ring and

decelerates abruptly to 153 m/s; at the same time, a wave starts propagating downwards at 279 m/s. The formation of the vortex ring correlates with the signal recorded by sensor S07. On the lower chronoplot, the propagation starts at the diaphragm and the corresponding signal is recorded by sensor S03. The first propagation front is not visible, but the second is. It shows higher contrast with the background than the first front, possibly because it carries a higher concentration of kaolin particles from the start. This front accelerates from 159 m/s, in the lower part, to 212 m/s in the upper part. After this, a series of downward and upward wave reflections propagate in the pipe. This plot does not show other corresponding pulses from the microseismic signals because they have different frequencies than the ones used for S03 and S07 in the plot. At around 20 ms in the upper part of the chronoplot, pieces of diaphragm rising toward the exit become visible.

In experiment GASMG, the first gas front rises at 463 m/s in the upper part of the pipe and decelerates to 126 m/s at the exit. In experiment KAOL, the first gas front rises at 451 m/s and decelerates to 106 m/s at the exit. In the experiments with particles, the front is never visible in the pipe, while at the exit it can create vortex rings rising at 104 to 115 m/s. The Re for the gas front associated with these exit velocities ranges from $2.7 \cdot 10^5$ to $4 \cdot 10^5$. The values are calculated using the density and viscosity of air and the inner pipe diameter as the characteristic length (Equation 4).

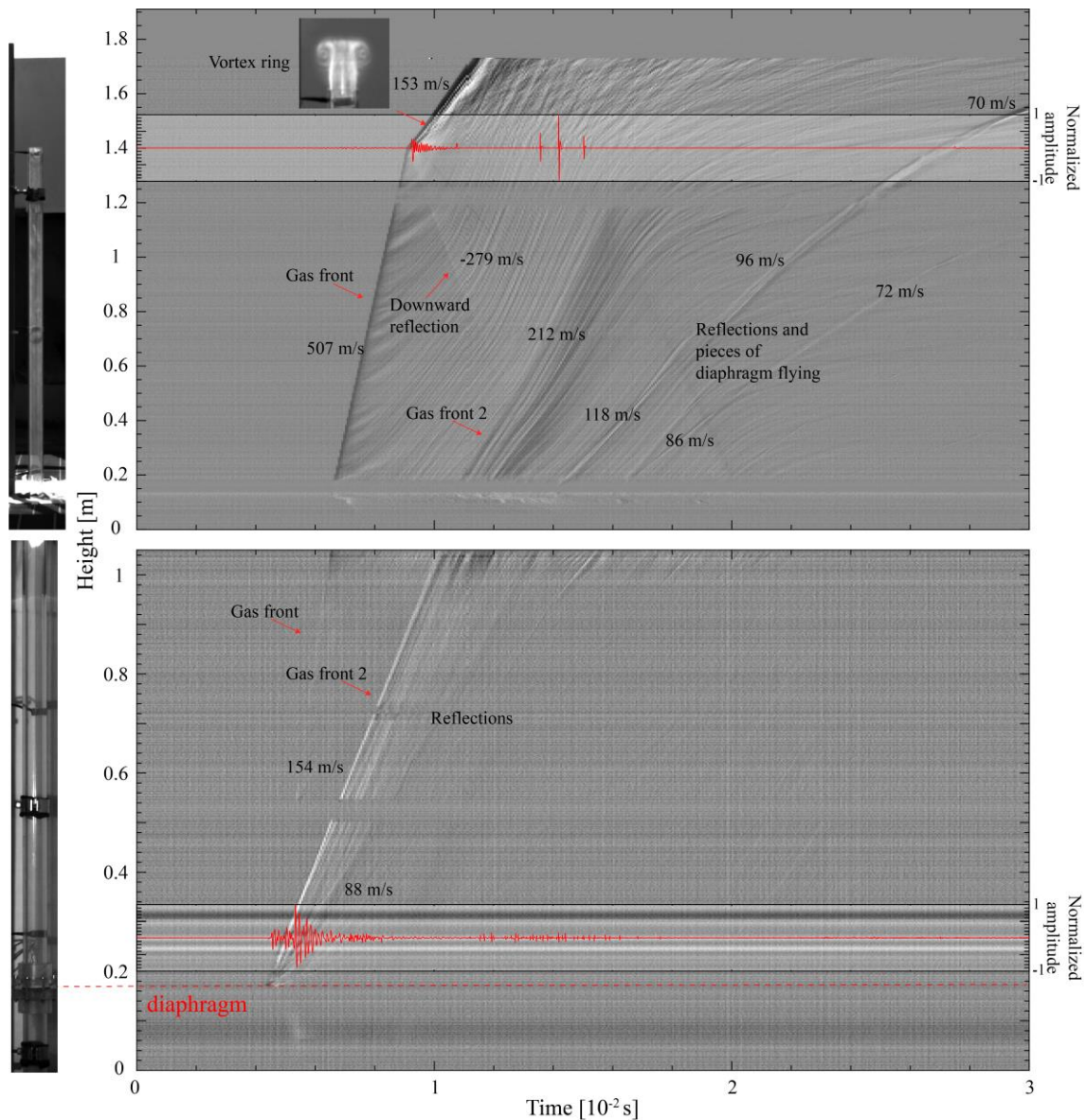


Figure 4.5 A chronoplot showing the propagation in height (y-axes) and time (x-axes) of gas front upward and downward propagation in experiment GAS. On the left side of the figure, two images of the lower and upper part of the pipe as recorded by the cameras. Due to experimental and camera setting there is a gap between the two parts: this gap is only graphical. The two parts are analysed separated and therefore the y-axes restart from zero in the upper part. The total height of the pipe is about 2 m. In the plot, thick lines delineate the propagation of the gas: the steeper the line, the faster the propagation. Negative velocity indicates a downward propagation. High frequency microseismic signals from S03 and S07 are plotted in the respective positions; they are correlated with diaphragm burst (S03) and vortex ring formation (S07).

4.4 Analysis of particle dynamics

In this section, I show the results of manually tracked particle velocity for PARTA (0.5-1 mm), PARTB (1-2 mm) and PARTC (2-4 mm) experiments as well as the automatic tracking on the front of the gas obtained using an automated detection algorithm. At ejection onset, the pressurized air expands in AP pipe and pushes the particles that will thus start moving upwards. The rising in the pipe and sequent ejection last up to 125 ms. The end is determined when particles do not exit the pipe anymore and the last ones, still

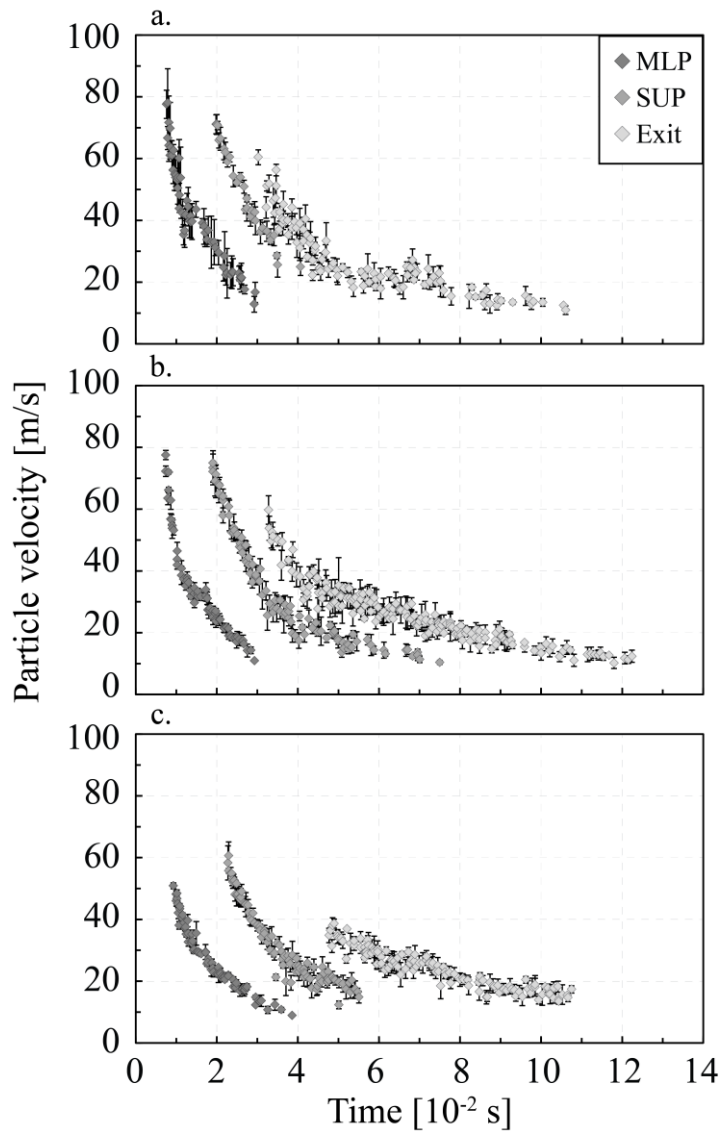


Figure 4.6 Evolution of particle velocity with time for experiments with particles of size a. 0.5-1 mm (PARTA), b. 1-2 mm (PARTB) and c. 2-4 mm (PARTC). The evolution was analysed in three different position in the pipe: MLP around 40 cm from the metal grid, SUP around 6 cm from S05 in the upper part of the pipe and “Exit” means at pipe exit. Time zero correspond to the starting of the upward movement marked by a sudden uplift of very fine particles, kaolin, laying on top of the sample.

in the pipe, start falling backward. I perform manual tracking of single particles passing three different positions in the pipe. The first tracking location is approximately in the middle of the lower part of the AP pipe (MLP in Figure 4.6), 40 ± 3 cm from the metal grid where particles lay at rest before decompression starts. The second location is 6 ± 2 cm above S05, which is located right at the start of the upper part of the pipe (SUP in Figure 4.6). The third location is at pipe exit (Exit in Figure 4.6). Figure 4.6 shows the evolution of particle velocity with time at the three positions mentioned above and for experiments performed with particles 0.5-1 mm (PARTA, Figure 4.6a), 1-2 mm (PARTB, Figure 4.6b), and 2-4 mm (PARTC, Figure 4.6c). Peak velocities range from 80 m/s for PARTA and PARTB in MLP and SUP positions to 60 m/s for PARTC in SUP position.

This means that particles accelerate up to 40 to 100 cm from the starting position and then start decelerating. At exit, they decelerate and lose 25% of their peak velocity in all three cases. The front particles are usually moving faster than the following ones, with the tail particles commonly showing the slowest velocity. Collisions between particles and with the pipe walls are frequent, especially among the particles in the tail of the flow, some of which do not even make it to the exit and start falling back in the pipe. The velocity trend of PARTA at exit (Figure 4.6 a) shows a secondary peak around 70 ms. Just before the peak, particles are exiting singularly or at most in groups of 3 to 5 particles at the same time. At 70 ms, a cluster of particles exits the pipe, resulting in slightly faster velocities than the particle just before them. After this, the deceleration continues.

In Figure 4.7, I present the chronoplot for experiment PARTB combined with the three charts showing the evolution of particle velocity with time. They correspond to the three velocity decays shown in Figure 4.6b for experiment PARTB in the three tracking locations. In the lower part, 0.2 m corresponds to the location of the diaphragm and the propagation starts from there. In the upper part, the pipe exit corresponds to 1.33 m on the chronoplot. From the upper part at exit, it is possible to recognize the propagation of a first gas front, with a velocity at exit of 116 m/s. It is not visible in the pipe, possibly because of reduced contrast with respect to the background, but it can be argued that the propagation velocity in the pipe should have been similar to the one showed in the GAS experiment (Figure 4.5), possibly a bit lower due to the loss in kinetic energy used to accelerate particles. On the other hand, a second gas front is observable for the whole pipe length, possibly because it is carrying a larger concentration of kaolin particles. It accelerates upward from 100 to 160 m/s. Particles follow the gas with an initial delay of 5 ms in the lower part. Later, as the gas accelerates faster, they are still slower than the gas front and arrive in the upper part with 20 ms delay. This delay between the second gas front and the particles allows us to observe the upper part counter-flow waves propagating downward. Once particles fill the pipe in its visible length, these downward reflections disappear from view, as they are most likely disturbed by the presence of particles. In addition, the velocity measured on the chronoplot, from the travelled height and relative time, show good agreement with the manually tracked velocity. Note that the portions of the pipe and the times at which I manually tracked particle velocity are highlighted in yellow in Figure 4.6.

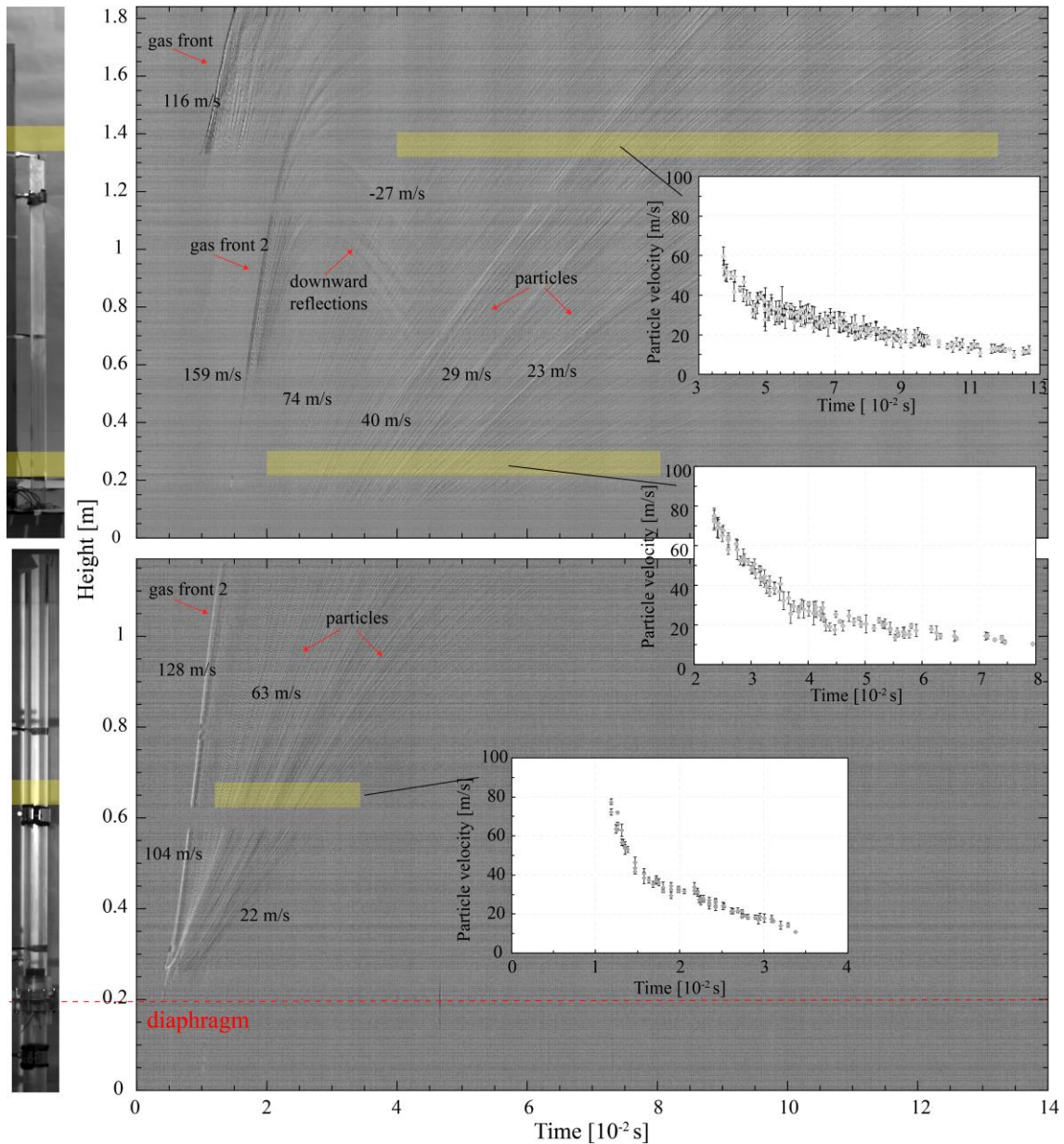


Figure 4.7 Chronoplot of experiment PARTB with correspondent charts of the evolution of particle velocity with time manually tracked. On the left, two images from the lower and upper part of the pipe, respectively, as recorded by the cameras. Similarly, to Figure 4.5 the gas propagation is visible. However, the first front is observable only once it reaches the exit and creates a vortex ring. Downward reflections are also partly visible in the upper part, as well as the particle rising. Yellow rectangles show the location in space (pipe height) and time of the manually tracked particles. There is good agreements between the two methodologies.

4.5 Discussion and remarks

In the presented experiments, I analyse the rising, propagation, and ejection of gas and particle mixtures in a long transparent pipe. These are to be considered preliminary experiments, as no repetition of the same conditions are currently available. However, the results offer interesting observations on the gas and particle dynamics.

The experiments are performed with increasing complexity: GAS ejects only air and a pinch of kaolin, while in GASMG, the metallic grid is inserted in the AP pipe. KAOL

tests the ejection of 7 g of kaolin while the three last experiments involve SL particles with increasing particle size, from 0.5-1 mm (PARTA), to 1-2 mm (PARTB), and finally, 2-4 mm (PARTC). In these last four experiments, the sample is always laying on top of the metal grid. Using image analysis, I am able to measure the gas front velocity and the particle velocity using a combination of automated algorithm and manual tracking with the MTrackJ software. The gas front velocity in the upper pipe and before exit, measured on the chronoplot, is highest (507 m/s) in experiment GAS and shows a decrease of about 9% in GASMG and 11 % in KAOL. In the experiments with SL particles, the same gas front is not visible in the pipe, but only at exit (see Figure 4.7, upper part of the chronoplot). At exit, after the abrupt deceleration, the velocity of GAS is still the highest; GASMG shows 17% lower velocity and the other experiments about 30% lower. These results show that adding obstacles in the path of the gas influences its propagation. Indeed, in the case of experiments KAOL, PARTA, PARTB and PARTC, part of the gas kinetic energy is lost to accelerate the particles upwards. Differences due to the experimental conditions can also be observed from the signal analysis, with sensor S07 showing the strongest trend. The microseismic signals are not widely investigated here, as they are not a focus of my investigation. However, from data collected they show great potential in correlating signal and related propagation process. In Figure 4.5, the creation of the vortex ring at exit, for example, corresponds to an acceleration in the microsignal of S07. A deeper investigation of the microsignals could surely provide more insights in the propagation dynamics.

Moreover, the transparent pipe allows for the characterization of particle propagation in the pipe. Results show an initial acceleration, reaching a peak between 40 and 100 cm from the diaphragm, depending on particle size. PARTA and PARTB show similar trends, while PARTC, which has coarser particles and is thus less coupled with the gas phase, shows generally lower velocity. At exit, particles are always decelerating. However, here they also show the least steep decay, compared to the measurement made in the lower part of the pipe (MLP) or at the start of the upper (SUP) part. This could mean that most of them are exiting at their terminal velocity. In PARTA, I observed a secondary small velocity peak around 70 ms on the velocity trend at exit (Figure 4.5a “Exit”). The peak corresponds to the exit of a clustering of particles. Particle clustering, and in general particle fraction, has been shown to increase the velocity of surrounding falling particles in particle falling experiments [Del Bello et al., 2017]. Moreover, particles moving upwards are subject to collisions, both with other particles in their vicinity and with the pipe walls. The latter especially occurs when particles are rising more slowly, so generally among the particles in the tail of the flow. No fragmentation

induced by these collisions is seen in the videos; however, I cannot confirm that the camera has adequate resolution to observe such processes.

5. Volcanic jets

One of the goal of performing the present empirical investigation was to provide observations on features that can be related to source conditions also in the field. In other words, if certain dynamics are observed during an explosive eruption, do they resemble anything observed in the lab? Linking nature and laboratory is not straight forward, as I anticipated before, natural processes are often far more complex than laboratory experiments. Moreover, the field does not always offer the best observational conditions, e.g. direct view on the active vent often not possible, clouds, unpredictable activity, etc. I present here the data collected from explosive eruptions on Stromboli volcano and discuss their comparison with the experiments.

5.1 Data recording

In May 2016, I participated to a ten days field campaign at Stromboli volcano, Italy. During this period, one of the vents in the SW crater (Figure 5.1a) repeatedly ejected bomb size (> 64 mm) pyroclasts; this type of activity is defined as “Type 1 (bomb-dominated) rapid explosions” [Gaudin et al., 2017]. They were recorded with the camera stationary set at *Pizzo sopra la Fossa* (Figure 5.1b), at an elevation of about 918 m a.s.l., about 100-150 m above the craters and at a horizontal distance of approximately 290 m from the crater area. The camera, a Phantom v711, was set at maximum resolution 1280x800, recording at 500 fps with 10 μ s exposure and 5 μ s EDR. Mounting a telescopic lens in the range of 70 to 300 mm. The pixel resolution in the images is 0.067059 m/pix. The best observation conditions were on the 26th of May 2016. Weather conditions during the day were good. In the crater, there was continue active degassing and the vents were mostly covered in sight by clouds of vapour. Out of the seven events recorded, the presence of the clouds affected only one event, and that is therefore not analysed. The seven events occurred in about two consecutive hours, at an interval of about 20 minutes one from the other, with the exception of the 5th and 6th events that happened with an interval of 3 minutes one from the other. After the last ejection, the activity at this vent stopped. At the same time nearby vents, from the same crater, were erupting mild to strong ash plume. The latter are not of interest in this investigation and it was the predominant activity during the whole field campaign.

I quantified particle velocity using MTrackJ; I tracked single particles at a resolution of 10 frames taking five consecutive tracking points per particle. The measured velocities are not absolute velocities, this because, using just one camera, it is not possible to define

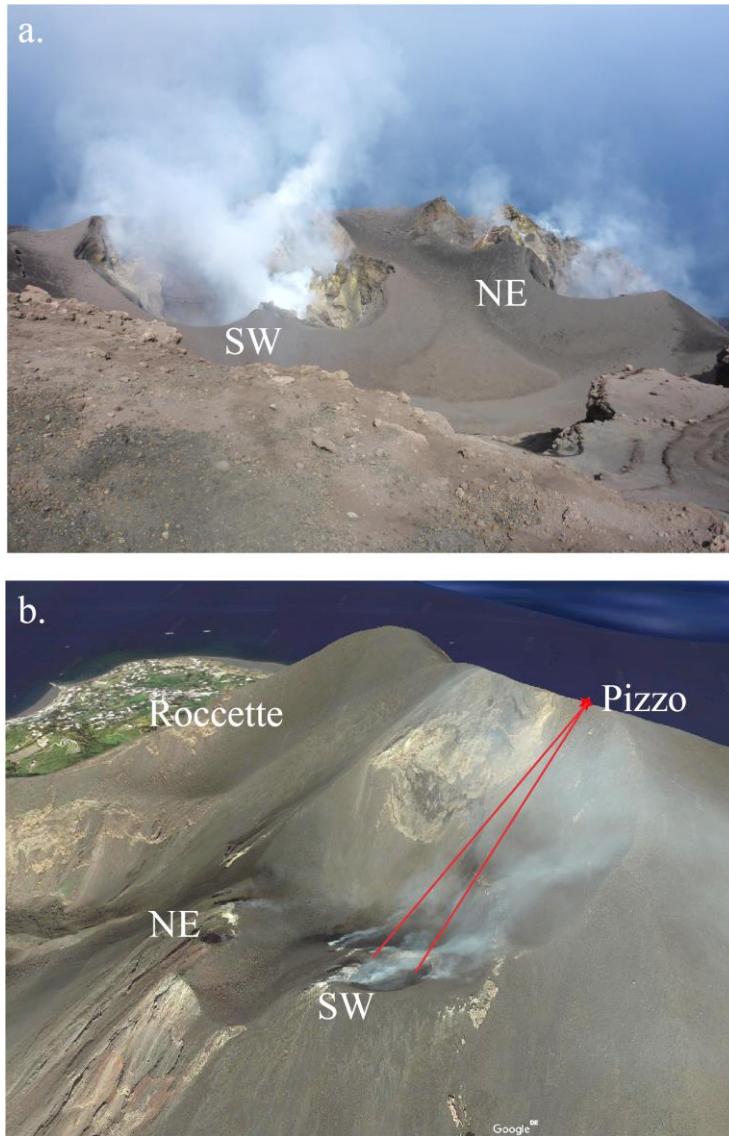


Figure 5.1 a. Picture taken during the field campaign in May 2016. It shows the crater area of Stromboli volcano, Italy, from Pizzo. On the left the SW crater and on the right the NE crater. b. Screenshot of the summit area of Stromboli from Google Earth, the red star is approximately the position of the camera looking down at the SW crater.

at which angle in respect to the camera the pyroclasts are flying and therefore they are considered to fly with a vertical trajectory. Gaudin et al. [2014] pointed out that for a particle moving at angle of 30° toward the observation point of the camera, its velocity will be underestimated of about 15%.

5.2 Pyroclasts velocity

Figure 5.2 shows the resulting velocity evolution with time of the pyroclasts ejected during the six events. The maximum velocity measured is 81 m/s (Figure 5.2a). Maximum velocity varies between 60 and 80 m/s, except for the event in Figure 5.2 d where velocities are all below 40 m/s. Single ejections last about 3 s. Apparent longer ejections (maximum 4 s here) are commonly the result of the arrival of a second ejection pulse. This is visible

in Figure 5.2a, and b. In addition, Figure 5.2f shows two shorter pulses of about 1 and 1.5 s, respectively. A second peak of pyroclasts velocity always highlights the start of the second pulse.

These velocity profiles show agreement with data from Stromboli eruptions reported in Taddeucci et al. [2012] and Gaudin et al [2014]. However, the maximum velocities could be considered quite low in comparison with other eruptions recorded on the same volcano. The camera was set to have a quite large field of view in this case, and only large bombs are accurately visible. I can observe a larger number of particles flying around these analysed bombs, but they are not in focus and therefore not measurable. Hence, the maximum velocity for the recorded events may also be higher than those here reported. Finally, it is not trivial to compare them with the experimental results. A decay trend is visible, and can be more or less steep, or not be visible at all like in the case of Figure 5.2d. It is also influenced by the arrival of secondary pulses, something that in the experiments presented is not yet reproducible. Moreover, I used natural particles in the experiments, but these particles are solid all the time. Taddeucci et al. [2017] have recently showed that bombs can often be fluidal when ejected, changing shape during in flight time and even breaking up in smaller pieces. All these processes of course increase the degree of complexity of the problem of volcanic pyroclasts ejections. In addition, I tracked the particles from their first appearance in the field of view, i.e. when they exit the vapour cloud and become visible. Accordingly, the location of the tracking could be some meters above the vent and particles could already have started deceleration. For this reason, if the vent cannot be seen directly, the particle spreading angle was not measured, because of the uncertainty of the starting point of the tangent to the trajectory.

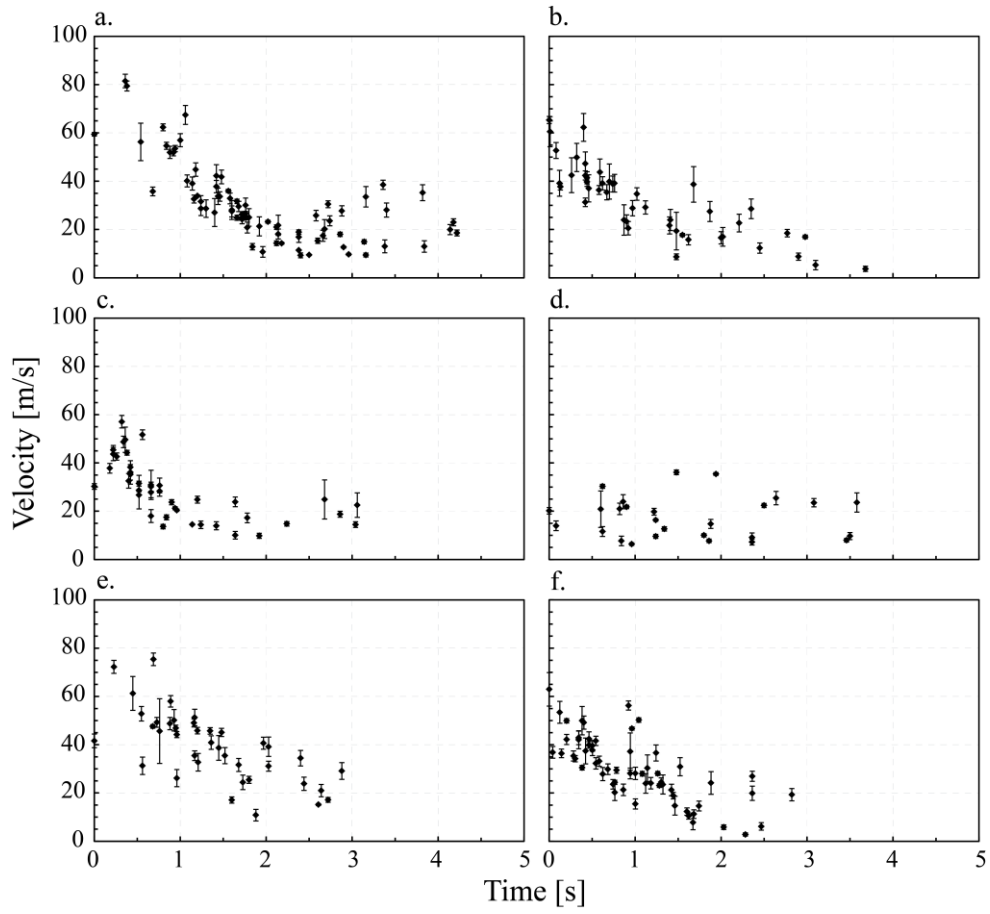


Figure 5.2 Plots of pyroclast exit velocity with time of the six eruptive events recorded at Stromboli volcano, Italy.

6. Outlook

I performed several sets of experiments on starting gas-particle jets to understand better phenomena observed and related to explosive volcanic eruptions. The aim was to better constrain the effect of boundary conditions such as vent geometry, tube length, particle load, temperature and overpressure on the jet dynamics and thereby better understand eruptive behaviour. The conditions tested reveal variable influence on parameters like particle ejection velocity, spreading angle, mass eruption rate, or electrical discharge. In the used setup, the “fragmentation bomb”, particle load is found to have the strongest effect, followed by tube length. At the conditions tested, the vent geometry shows a small influence on particle velocity, mainly confined to the maximum values recorded, while it shows a larger effect on the spreading angle, both in terms of maximum values and evolution with time. Coarse (1-2 mm) and medium (0.5-1 mm) size particles show similar behaviour, while the fine (0.125-0.250 mm) size fraction shows, at least on the spreading angle results, substantially different trends, possibly due to a different and better coupling with the gas phase. At the chosen observational conditions, the velocity of single particles of the fine fraction is impossible to measure. This data gap could be resolved in future studies by choosing a smaller field of view and even higher temporal resolution. A second approach could be to employ a laser Doppler system. This way one could contribute to understanding if and to which degree particles are coupled with the gas phase and what is the main effect of this coupling.

I used the temporal evolution of particle exit velocity to test the applicability of the fragmentation depth model proposed by Alatorre-Ibargüengoitia et al. [2011] on the performed conditions. Results show good applicability only for experiments performed with setup 1 and 3, both of which used the same amount of sample material; in experiments with setup 2 however, an error of up to 100% is found. As this model has been applied to constrain real eruptions, it is therefore of paramount importance to reinvestigate the dependence of the model in the light of the uniform starting conditions and decipher why the variability (as to be expected in nature) of some experimental sets could not be forecasted.

In addition, the experiment performed with the “jet buster” provide important insights into gas and particle dynamics rising in a long and tubular conduit. In these experiments, I show in particular how the combination of direct video observations and microseismic signals provides a more comprehensive characterization of processes and dynamics occurring along the tube and at vent exit. It is possible to correlate propagation velocities,

particle dynamics and signal acceleration, amplitude and therefore estimate the related forces exerted by the flow on the pipe system depending on experimental conditions. Particle-particle and particle-wall collisions are observed in the pipe, they both influence particle velocity and trajectory, while particle fragmentation is not observed. Finally, this experiments show great potential for the investigation of not only ejection dynamics, but also conduit flow. In particular, I find very important the coupling of visual observations and microseismic signals. The performed experiments should be integrated with further testing of, for example, different 1) gas volume and pressure; 2) particle size, and 3) tube length. In particular, very fine particles in the range of 20 to 100 μm could be used to investigate volcanic plumes characteristics. In addition, I think that the possibility of having more than one HP section should be tested to investigate the influence of multiple pulses on flow propagation and ejection dynamics.

The comparison with observations from volcanic eruptions is not trivial yet, but patterns can be recognized. Natural eruptions are far more complex than the experiments here presented, yet it is necessary to simplify a process in order to understand it and to understand the effect of boundary conditions on it. Only if a – apparently simple at first glance - process is well constrained, complexities can be added. In this respect, future investigations should definitively include the use of complex vent geometries as usually observed in nature.

Furthermore, empirical results could be used to test the accuracy of numerical models working of volcanic explosive eruptions and dealing with non-coupled gas-particles starting jets. A series of DNS (direct numerical simulation) of gas jets assuming conditions similar to the “fragmentation bomb” settings were initiated in collaboration with the Technische Universität of Berlin (TUB) and are currently under investigation in an ongoing PhD thesis. In a first step (and limited to 2.5 million CPU hours), no particles were taken into consideration, as the main goal was to simulate turbulent gas dynamics in the experimental system at the highest possible level of detail. Preliminary results indicate that the high pressure used in the “fragmentation bomb” is a major challenge. In fact, the most complex condition resolved so far was 8 MPa overpressure in the reservoir. Higher pressures lead to a spatial and temporal non-physical solution of the jet turbulence. Therefore, more work in this direction is necessary.

Finally, I think the data set present here provides a promising link for both field volcanology (visual observations and quantitative monitoring) as well as numerical modelling in order to advance our understanding of explosive volcanic eruptions and assess the related hazard. Better knowledge of these inherently unstable and dynamic processes may well be applied in the field of general understanding of gas-particle dynamics.

Appendix A

In this section, I present the comparison of the effect of vent geometry on velocity decay for the conditions not presented in the main text. Figure A1 shows the results of experiments performed with particles 1-2 mm, 500°C, Figure A2 and A3 experiments with 0.5-1 mm particles, room temperature and 500°C, respectively.

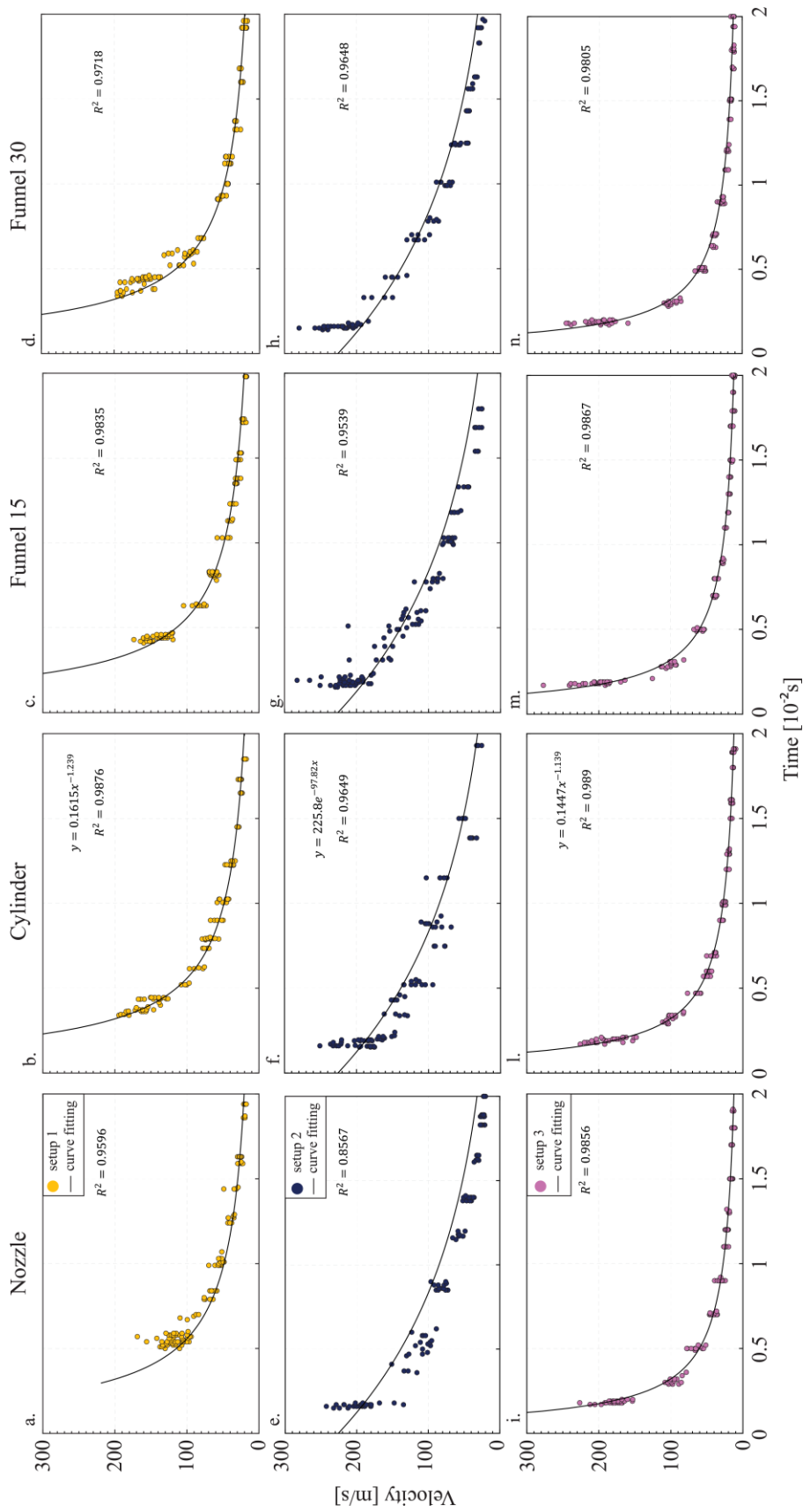


Figure A.1 Particle jet velocity decay with time is shown for the four different vent geometries and setups, SL 1-2 mm particles, 15 MPa, 500 °C. The curve fitting obtained for the cylinder vent case is superimposed on the data from the other vents. The equations can be found on the relative chart.

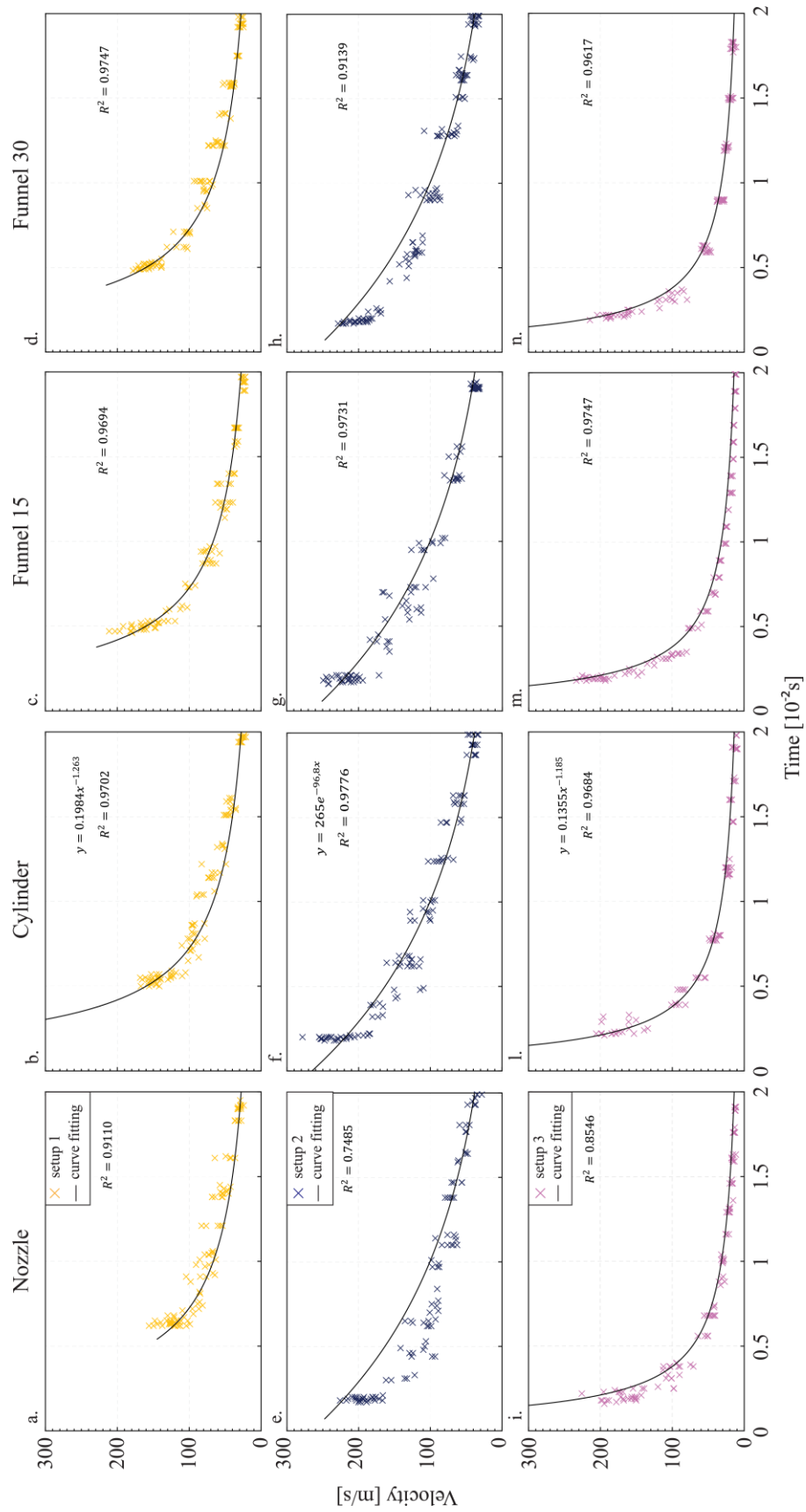


Figure A.2 Particle jet velocity decay with time is shown for the four different vent geometries and setups, SL 0.5-1 mm particles, 15 MPa, room temperature. The curve fitting obtained for the cylinder vent case is superimposed on the data from the other vents. The equations can be found on the relative chart

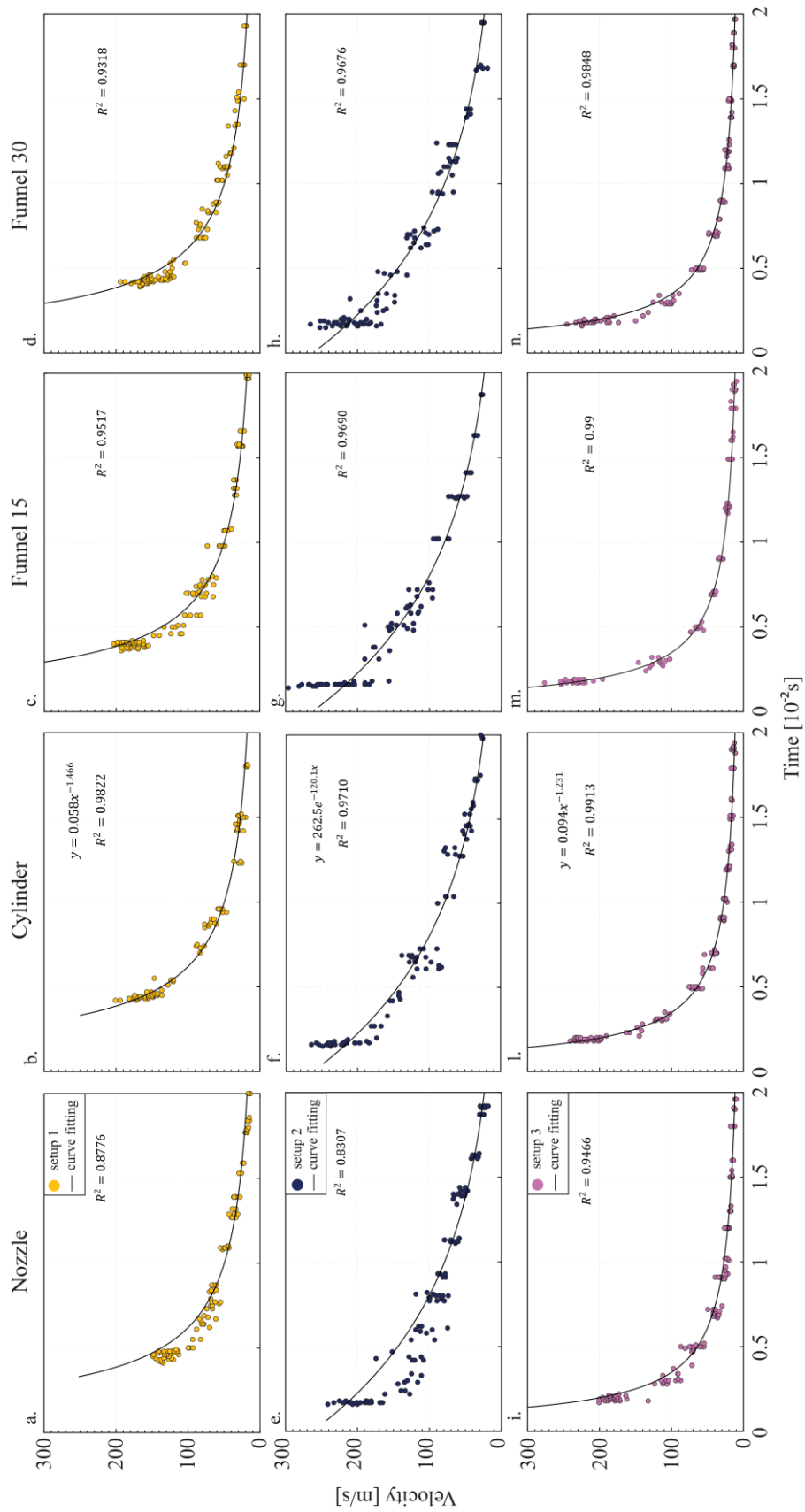


Figure A.3 Particle jet velocity decay with time is shown for the four different vent geometries and setups, SL 0.5-1 mm particles, 15 MPa, 500 °C. The curve fitting obtained for the cylinder vent case is superimposed on the data from the other vents. The equations can be found on the relative chart

Appendix B

In this section, I present the comparison of the effect of vent geometry on gas and particle spreading angle evolution for the conditions not presented in the main text. Figure B1 shows the results of experiments performed with particles 1-2 mm and room temperature, Figure B2, 1-2 mm particles and 500°C, Figure B3 and B4 experiments with 0.5-1 mm particles, room temperature and 500°C, respectively. Finally, Figure B5 and B6 show the results of experiments performed with 0.125-0.250 mm particles room temperature and 500°C, respectively.

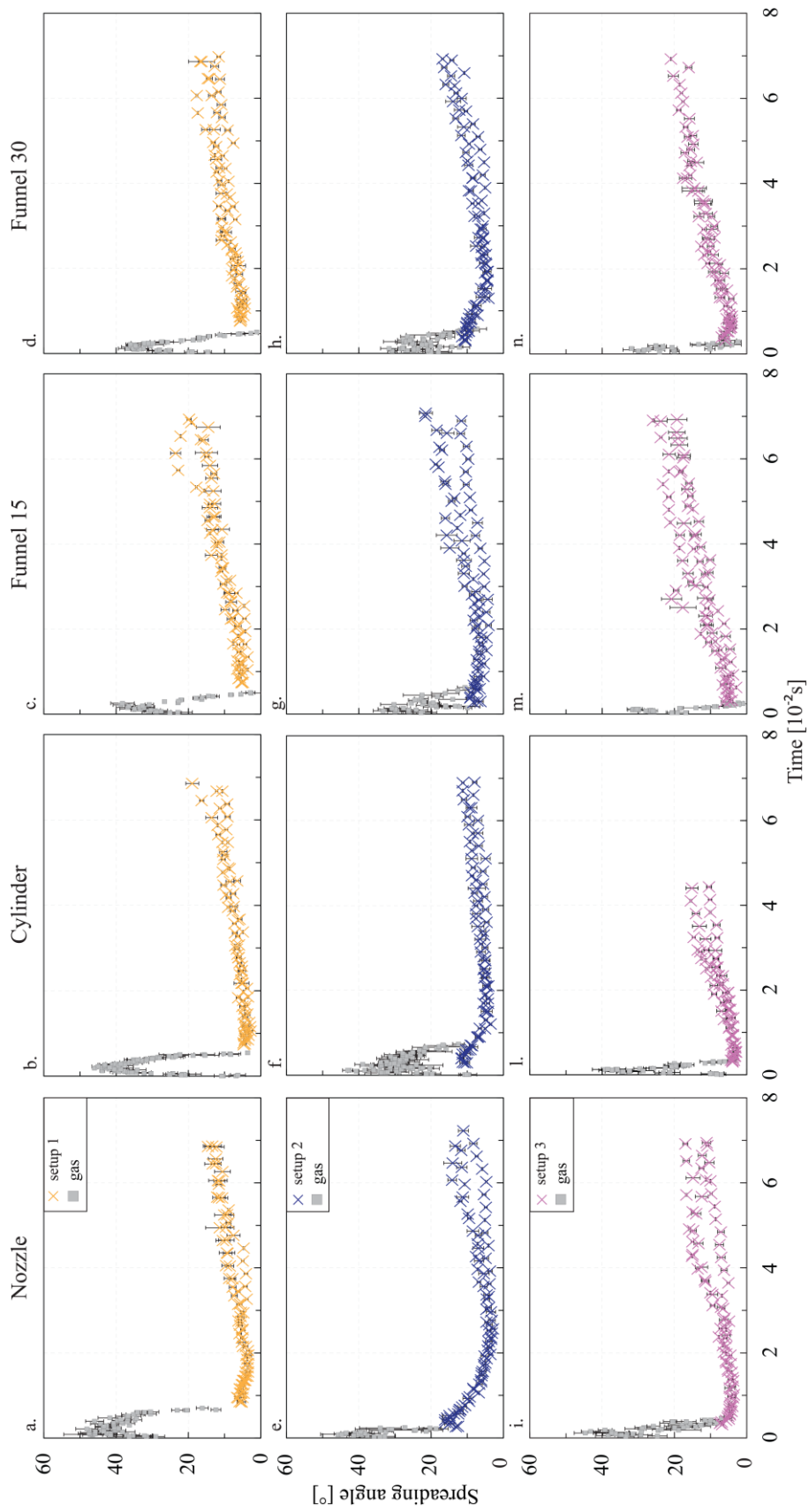


Figure B.0.1 Gas and particle spreading angle evolution with time is shown for the four different vent geometries and setups, SL 1-2 mm particles, 15 MPa, 25°C. Error bars can be smaller than related symbol

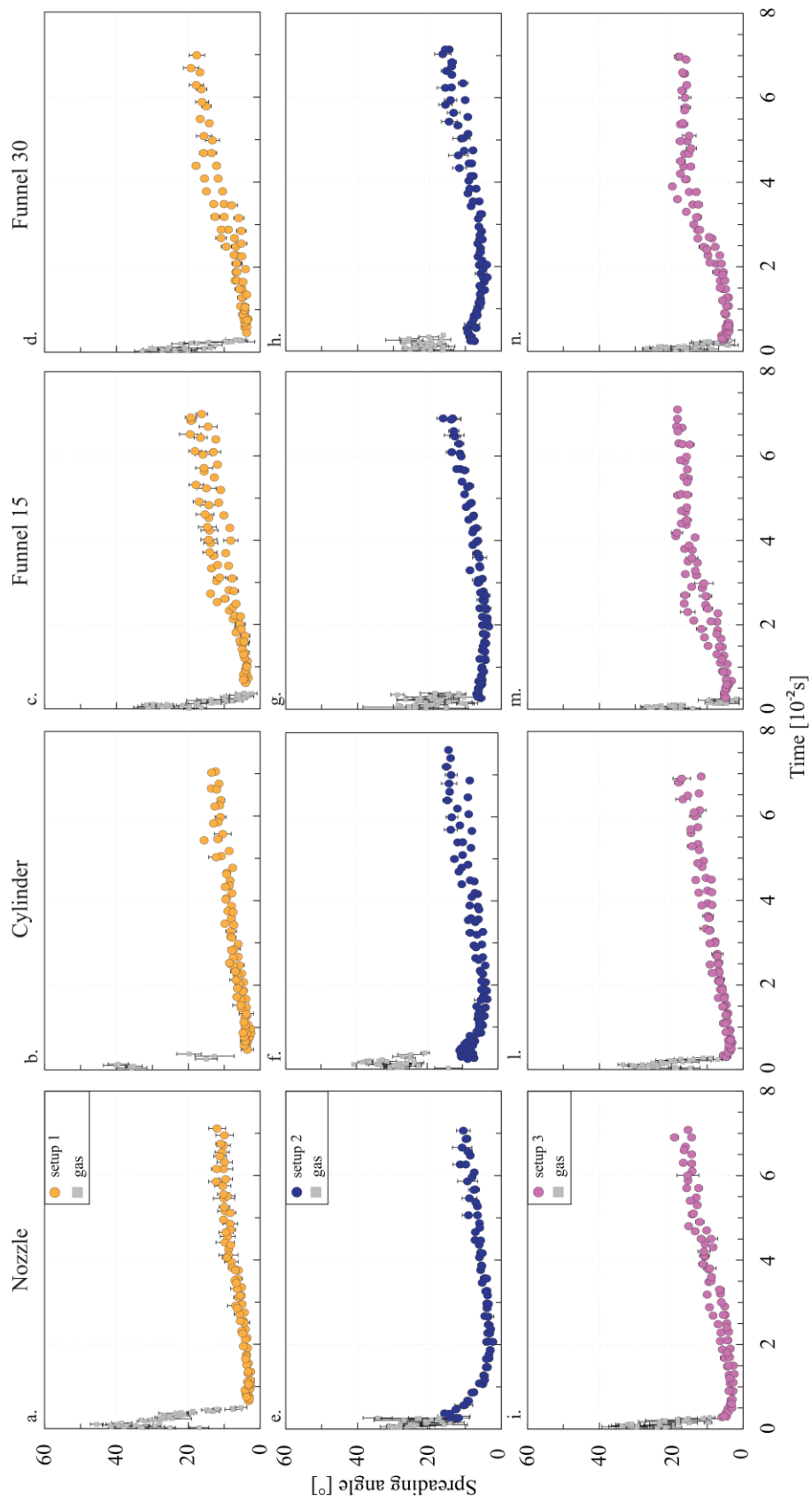


Figure B.0.2 Gas and particle spreading angle evolution with time is shown for the four different vent geometries and setups, SL 1-2 mm particles, 15 MPa, 500°C. Error bars can be smaller than related symbol.

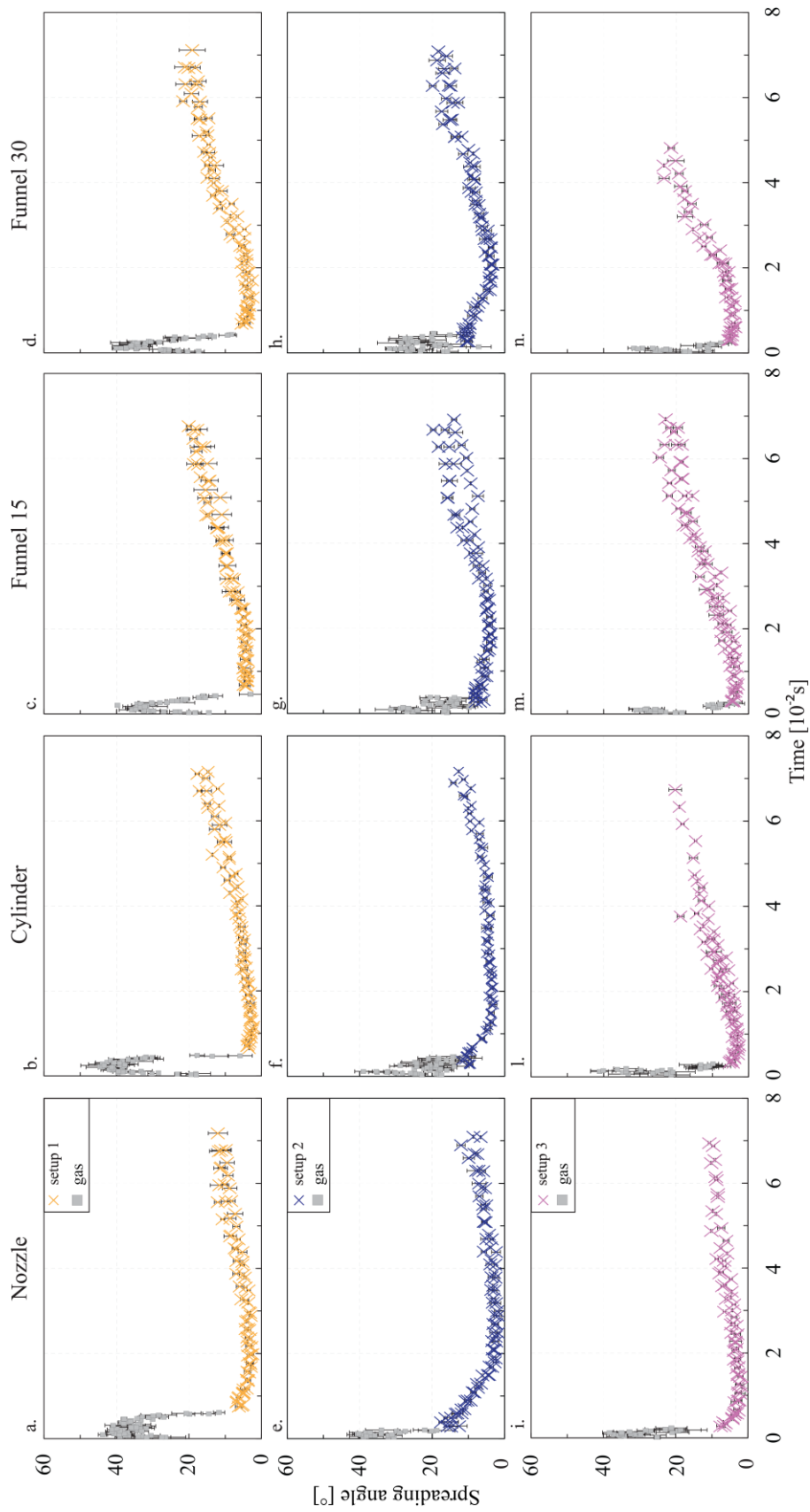


Figure B.0.3 Gas and particle spreading angle evolution with time is shown for the four different vent geometries and setups, SL 0.5-1 mm particles, 15 MPa, 25°C. Error bars can be smaller than related symbol.

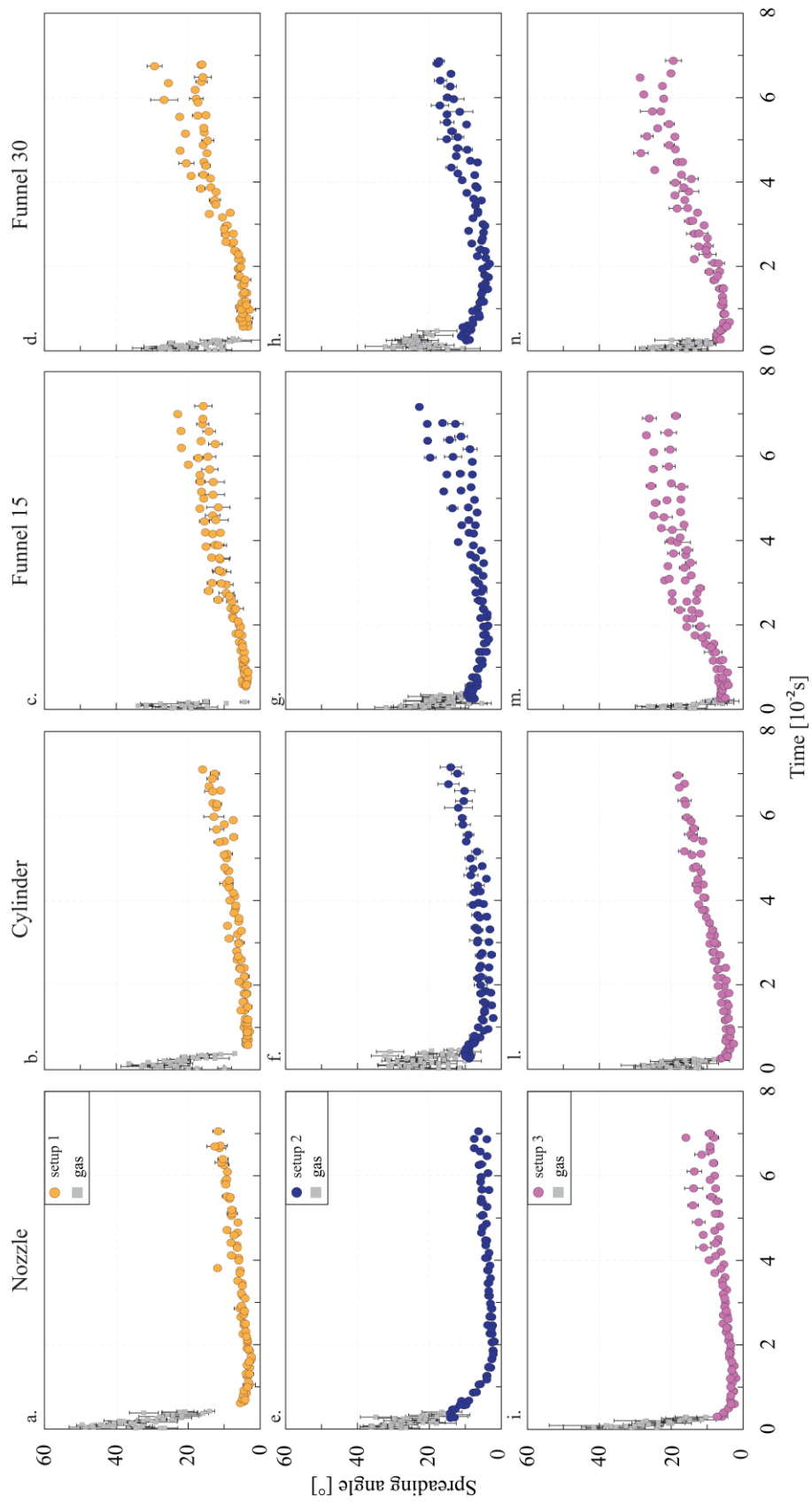


Figure B.0.4 Gas and particle spreading angle evolution with time is shown for the four different vent geometries and setups, SL 0.5-1 mm particles, 15 MPa, 500°C. Error bars can be smaller than related symbol.

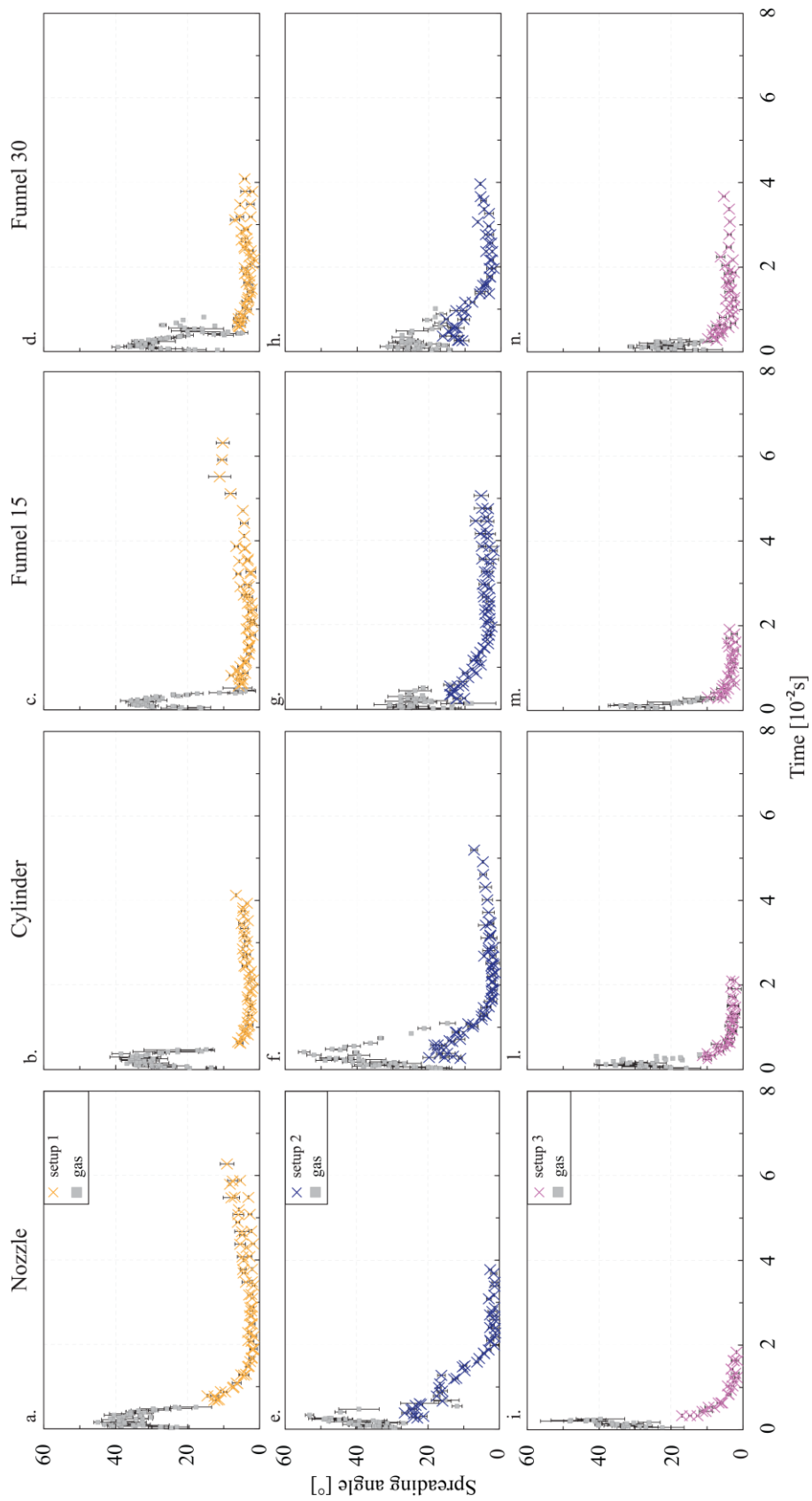


Figure B.0.5 Gas and particle spreading angle evolution with time is shown for the four different vent geometries and setups, SL 0.125-0.250 mm particles, 15 MPa, 25°C. Error bars can be smaller than related symbol.

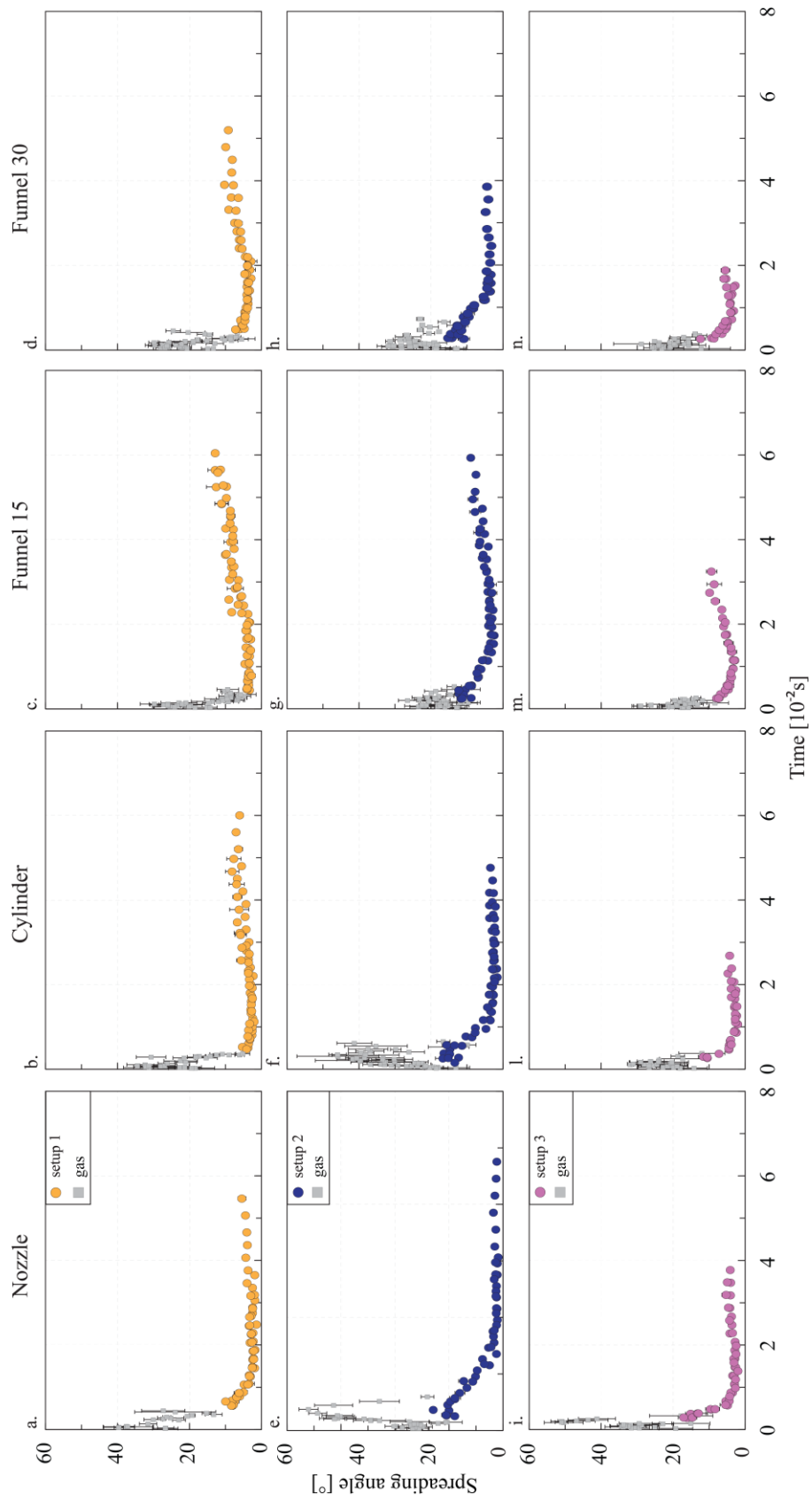


Figure B.0.6 Gas and particle spreading angle evolution with time is shown for the four different vent geometries and setups, SL 0.125-0.250 mm particles, 15 MPa, 500°C. Error bars can be smaller than related symbol.

List of references

- Agrawal, K., P.N. Loezos, M. Syamlal, and S. Sundaresan (2001), The role of meso-scale structures in rapid gas–solid flows, *Journal of Fluid Mechanics*, 445, 151–185, doi:10.1017/S0022112001005663
- Aizawa, K., C. Cimarelli, M.A. Alatorre-Ibargüengoitia, A. Yokoo, D.B. Dingwell, and M. Iguchi (2016), Physical properties of volcanic lightning: Constraints from magnetotelluric and video observations at Sakurajima volcano, Japan, *Earth and Planetary Science Letters*, 444, 45–55, doi:10.1016/j.epsl.2016.03.024
- Alatorre-Ibargüengoitia, M.A., B. Scheu, D.B. Dingwell, H. Delgado-Granados, and J. Taddeucci (2010), Energy consumption by magmatic fragmentation and pyroclast ejection during Vulcanian eruptions, *Earth and Planetary Science Letters*, 291(1–4), 60–69, doi:10.1016/j.epsl.2009.12.051
- Alatorre-Ibargüengoitia, M.A., B. Scheu, and D.B. Dingwell (2011), Influence of the fragmentation process on the dynamics of Vulcanian eruptions: An experimental approach, *Earth and Planetary Science Letters*, 302(1-2), 51–59, doi:10.1016/j.epsl.2010.11.045
- Alidibirov, M.A., and D.B. Dingwell (1996a), An experimental facility for the investigation of magma fragmentation by rapid decompression, *Bulletin of Volcanology*, 58(5), 411–416, doi:10.1007/s004450050149
- Alidibirov, M.A., and D.B. Dingwell (1996b), Magma fragmentation by rapid decompression. *Letters to Nature*, 380, 146–148, doi:10.1038/380146a0
- Anderson, R., S. Björnsson, D.C. Blanchard, S. Gathman, J. Hughes, S. Jónasson, C.B. Moore, H.J. Survilas, and B. Vonnegut (1965), Electricity in volcanic clouds, *Science*, 148(3674), pp.1179-1189
- Andronico, D., J. Taddeucci, A. Cristaldi, L. Miraglia, P. Scarlato, and M. Gaeta (2013), The 15 March 2007 paroxysm of Stromboli: video-image analysis, and textural and compositional features of the erupted deposit, *Bulletin of Volcanology*, 75(7), 733, doi:10.1007/s00445-013-0733-2
- Anilkumar, A., R. Sparks, and B. Sturtevant (1993), Geological implications and applications of high-velocity two-phase flow experiments, *Journal of Volcanology and Geothermal Research*, 56(1–2), 145–160, doi:10.1016/0377-0273(93)90056-W
- Arciniega-Ceballos, A., M. Alatorre-Ibargüengoitia, B. Scheu, D.B. Dingwell, and H. Delgado-Granados (2014), Seismological analysis of conduit dynamics in fragmentation experiments, *Journal of Geophysical Research: Solid Earth*, 119(3), 2215–2229, doi:10.1002/2013JB010646
- Arciniega-Ceballos, A., M. Alatorre-Ibargüengoitia, B. Scheu, and D.B. Dingwell (2015), Analysis of source characteristics of experimental gas burst and fragmentation explosions generated by rapid decompression of volcanic rocks, *Journal of Geophysical Research: Solid Earth*, 120(7), 5104–5116, doi:10.1002/2014JB011810
- Aubry, T.J., A.M. Jellinek, G. Carazzo, R. Gallo, K. Hatcher, and J. Dunning (2017) A new analytical scaling for turbulent wind-bent plumes: Comparison of scaling laws with

- analog experiments and a new database of eruptive conditions for predicting the height of volcanic plumes, *Journal of Volcanology and Geothermal Research*, 343, 233–251, doi:10.1016/j.jvolgeores.2017.07.006
- Behnke, S.A., R.J. Thomas, S.R. McNutt, D.J. Schneider, P.R. Krehbiel, W. Rison, and H.E. Edens (2013), Observations of volcanic lightning during the 2009 eruption of Redoubt Volcano, *Journal of Volcanology and Geothermal Research*, 259, 214–234, doi:10.1016/j.jvolgeores.2011.12.010
- Bercovici, D., and C. Michaut (2010), Two-phase dynamics of volcanic eruptions: compaction, compression and the conditions for choking, *Geophysical Journal International*, 182(2), 843–864, doi:10.1111/j.1365-246X.2010.04674.x
- Bonadonna C., and A. Costa (2013), Modelling tephra sedimentation from volcanic plumes, in *Modeling volcanic processes: The Physics and Mathematics of Volcanism*, edited by S. A. Fagents et al., pp 173-202, Cambridge
- Bonadonna, C., A. Costa, A. Folch and T. Koyaguchi (2015), Tephra dispersal and sedimentation. *The encyclopedia of volcanoes – 2nd edition*, edited by H. Sigurdsson et al., pp. 587- 598, Elsevier
- Budilarto, S.G. (2003), An experimental study on effects of fluid aerodynamics and particle size distribution in particle-laden jet flows, PhD thesis, Purdue University, West Lafayette, USA
- Burgisser, A., G.W. Bergantz, and R.E. Breidenthal (2005), Addressing complexity in laboratory experiments: The scaling of dilute multiphase flows in magmatic systems, *Journal of Volcanology and Geothermal Research*, 141(3–4), 245–265, doi:10.1016/j.jvolgeores.2004.11.001
- Cagnoli, B., A. Barmin, O. Melnik, and R.S.J. Sparks (2002), Depressurization of fine powders in a shock tube and dynamics of fragmented magma in volcanic conduits, *Earth and Planetary Science Letters*, 204(1–2), 101–113, doi:10.1016/S0012-821X(02)00952-4
- Capponi, A., J. Taddeucci, P. Scarlato, and D.M. Palladino (2016), Recycled ejecta modulating Strombolian explosions, *Bulletin of Volcanology*, 78(2), 1–13, doi:10.1007/s00445-016-1001-z
- Carcano, S., Bonaventura, L., Esposti Ongaro, T., and Neri, A. (2013). A semi-implicit, second order accurate numerical model for multiphase underexpanded volcanic jets. *Geoscientific Model Development Discussions*, 6(1), 399–452 doi:10.5194/gmdd-6-399-2013
- Carcano, S., T. Esposti Ongaro, L. Bonaventura, and A. Neri (2014), Influence of grain-size distribution on the dynamics of underexpanded volcanic jets, *Journal of Volcanology and Geothermal Research*, 285, 60–80, doi:10.1016/j.jvolgeores.2014.08.003
- Carn, S., N. Krotkov, K. Pickering, D. Allen, and E. Bucseles (2016), Satellite observations of lightning-generated NO_x in volcanic eruption clouds, in 2016 EGU General Assembly Conference Abstracts, vol. 18, p. 9606
- Cashman, K.V., and B. Scheu (2015), Magmatic fragmentation. *The encyclopedia of volcanoes – 2nd edition*, edited by H. Sigurdsson et al., pp. 257- 264, Elsevier.
- Cerminara, M., Esposti Ongaro, T., and Neri, A. (2016). Large Eddy Simulation of gas-particle kinematic decoupling and turbulent entrainment in volcanic plumes. *Journal of*

Volcanology and Geothermal Research, 326, 143–171, doi:10.1016/j.jvolgeores.2016.06.018

Chojnicki, K., A.B. Clarke, and J.C. Phillips (2006), A shock-tube investigation of the dynamics of gas-particle mixtures: Implications for explosive volcanic eruptions, *Geophysical Research Letters*, 33(15), L15309, doi:10.1029/2006GL026414

Chojnicki, K.N., A.B. Clarke, J.C. Phillips, & R.J. Adrian (2015a), Rise dynamics of unsteady laboratory jets with implications for volcanic plumes, *Earth and Planetary Science Letters*, 412, 186–196, doi:10.1016/j.epsl.2014.11.046

Chojnicki, K.N., A.B. Clarke, J.C. Phillips, and R.J. Adrian (2015b), The evolution of volcanic plume morphology in short-lived eruptions, *Geology*, 43(8), 707–710, doi:10.1130/G36642.1

Cimarelli, C., M.A. Alatorre-Ibarguengoitia, U. Kueppers, B. Scheu, and D.B. Dingwell (2014), Experimental generation of volcanic lightning, *Geology*, 42(1), 79–82, doi:10.1130/G34802.1

Cimarelli, C., M.A. Alatorre-Ibargüengoitia, K. Aizawa, A. Yokoo, A. Díaz-Marina, M. Iguchi, and D.B. Dingwell (2016), Multiparametric observation of volcanic lightning: Sakurajima Volcano, Japan, *Geophysical Research Letters*, 43(9), 4221–4228, doi:10.1002/2015GL067445

Clarke, A.B., J.C. Phillips, and K.N. Chojnicki (2009), An investigation of Vulcanian eruption dynamics using laboratory analogue experiments and scaling analysis, *Studies in Volcanology* 2, 155-166

Clarke, A.B. (2013), Unsteady explosive activity: vulcanian eruptions, in *Modeling volcanic processes: The Physics and Mathematics of Volcanism*, edited by S. A. Fagents et al., pp 129-152, Cambridge

Del Bello, E., J. Taddeucci, M. de' Michieli Vitturi, P. Scarlato, D. Andronico, S. Scollo, U. Kueppers, and T. Ricci (2017), Effect of particle volume fraction on the settling velocity of volcanic ash particles: insights from joint experimental and numerical simulations, *Scientific reports*, 7, pp. 39620

Dellino, P., M. T. Gudmundsson, G. Larsen, D. Mele, J. A. Stevenson, T. Thordarson, and B. Zimanowski (2012), Ash from the Eyjafjallajökull eruption (Iceland): Fragmentation processes and aerodynamic behavior, *J. Geophys. Res.*, 117, B00C04, doi:10.1029/2011JB008726.

de' Michieli Vitturi, M., A.B. Clarke, A. Neri and B. Voight (2008), Effects of conduit geometry on magma ascent dynamics in dome-forming eruptions. *Earth and Planetary Science Letters*, 272(3–4), 567–578, doi:10.1016/j.epsl.2008.05.025

Douillet, G.A., K.R. Rasmussen, U. Kueppers, D. Lo Castro, J.P. Merrison, J.J. Iversen, and D.B. Dingwell (2014), Saltation threshold for pyroclasts at various bedslopes: Wind tunnel measurements, *Journal of Volcanology and Geothermal Research*, 278–279, 14–24, doi:10.1016/j.jvolgeores.2014.03.011

Dubosclard, G., F. Donnadieu, P. Allard, R. Cordesses, C. Hervier, M. Coltelli, and J. Kornprobst (2004), Doppler radar sounding of volcanic eruption dynamics at Mount Etna, *Bulletin of Volcanology*, 66(5), 443–456, doi:10.1007/s00445-003-0324-8

- Dürig, T., M.T. Gudmundsson, and P. Dellino (2015), Reconstruction of the geometry of volcanic vents by trajectory tracking of fast ejecta - the case of the Eyjafjallajökull 2010 eruption (Iceland), *Earth, Planets and Space*, 67(1), 64, doi:10.1186/s40623-015-0243-x
- Elghobashi, S., and G.C. Truesdell (1993), On the two-way interaction between homogeneous turbulence and dispersed solid particles. I: Turbulence modification, *Physics of Fluids A: Fluid Dynamics*, 5(7), 1790–1801, doi:10.1063/1.858854.
- Gardner, J. E., R.M.E. Thomas, C. Jaupart, C., and S. Tait (1996), Fragmentation of magma during Plinian volcanic eruptions. *Bulletin of Volcanology*, 58(2–3), 144–162, doi:10.1007/s004450050132
- Gaudin, D., J. Taddeucci, P. Scarlato, M. Moroni, C. Freda, M. Gaeta, and D.M. Palladino (2014), Pyroclast Tracking Velocimetry illuminates bomb ejection and explosion dynamics at Stromboli (Italy) and Yasur (Vanuatu) volcanoes, *Journal of Geophysical Research Solid Earth*, 119, 5384–5397, doi:10.1002/2014JB011096
- Gaudin, D., J. Taddeucci, P. Scarlato, E. del Bello, T. Ricci, T. Orr, B. Houghton, A. Harris, S. Rao and A. Bucci (2017), Integrating puffing and explosions in a general scheme for Strombolian-style activity, *Journal of Geophysical Research: Solid Earth*, 122(3), 1860–1875, doi:10.1002/2016JB013707
- Gouhier, M., and F. Donnadieu (2011), Systematic retrieval of ejecta velocities and gas fluxes at Etna volcano using L-Band Doppler radar, *Bulletin of Volcanology*, 73(9), 1139–1145, doi:10.1007/s00445-011-0500-1
- Graettinger, A.H., G.A. Valentine, I. Sonder, P.S. Ross, and J.D.L White (2015), Facies distribution of ejecta in analog tephra rings from experiments with single and multiple subsurface explosions, *Bulletin of Volcanology*, 77(8), 66, doi:10.1007/s00445-015-0951-x
- Head, J.W., and L. Wilson (1989), Basaltic pyroclastic eruptions: Influence of gas-release patterns and volume fluxes on fountain structure, and the formation of cinder cones, spatter cones, rootless flows, lava ponds and lava flows. *Journal of Volcanology and Geothermal Research*, 37(3-4), 261–271, doi:10.1016/0377-0273(89)90083-8
- Holzmueller J. (2016). Shock-tube experiments with forced impact: Analysis of the resulting grain size distribution to reveal the contribution of secondary processes. Unpublished Bachelor Thesis. LMU Munich, Germany.
- Houghton, B.F., D.A. Swanson, J. Rausch, R.J. Carey, S.A. Fagents, and T.R. Orr (2013), Pushing the volcanic explosivity index to its limit and beyond: Constraints from exceptionally weak explosive eruptions at Kilauea in 2008, *Geology*, 41(6), 627–630, doi:10.1130/G34146.1
- Kaminski, É., and C. Jaupart (1997), Expansion and quenching of vesicular magma fragments in Plinian eruptions, *Journal of Geophysical Research: Solid Earth*, 102(B6), 12187–12203, doi:10.1029/97JB00622
- James, M.R., S.J. Lane, and B.F. Houghton (2013), Unsteady explosive activity: strombolian eruptions, in *Modeling volcanic processes: The Physics and Mathematics of Volcanism*, edited by S. A. Fagents et al., pp 107-128, Cambridge
- Jessop, D.E., and A.M. Jellinek (2014), Effects of particle mixtures and nozzle geometry on entrainment into volcanic jets. *Geophysical Research Letters*, 41(11), 3858–3863, doi:10.1002/2014GL060059

- Jessop, D.E., J. Gilchrist, A.M. Jellinek, and O. Roche (2016), Are eruptions from linear fissures and caldera ring dykes more likely to produce pyroclastic flows?, *Earth and Planetary Science Letters*, 454(October), 142–153, doi:10.1016/j.epsl.2016.09.005
- Kieffer, S.W. (1984), Factors governing the structure of volcanic jets, in *Explosive volcanism: inception, evolution, and hazards*, edited by F.R. Boyd, pp 143-157, National Academy Press, Washington
- Kieffer, S.W. (1989), Geologic nozzles, *Reviews of Geophysics*, 27(1), 3-38
- Kieffer, S.W., and B. Sturtevant (1984), Laboratory studies of volcanic jets. *Journal of Geophysical Research*, 89(B10), 8253, doi:10.1029/JB089iB10p08253
- Koyaguchi, T., and A.W. Woods (1996), On the formation of eruption columns following explosive mixing of magma and surface-water, *Journal of Geophysical Research*, 101(B3), 5561, doi:10.1029/95JB01687
- Koyaguchi, T. (2005), An analytical study for 1-dimensional steady flow in volcanic conduits, *Journal of Volcanology and Geothermal Research*, 143(1–3), 29–52, doi:10.1016/j.jvolgeores.2004.09.009
- Koyaguchi, T., Y.J. Suzuki and T. Kozono (2010), Effects of the crater on eruption column dynamics, *Journal of Geophysical Research*, 115(B7), B07205, doi:10.1029/2009JB007146
- Kueppers, U., D. Perugini, and D.B. Dingwell (2006a), “Explosive energy” during volcanic eruptions from fractal analysis of pyroclasts, *Earth and Planetary Science Letters*, 248(3-4), 800–807, doi:10.1016/j.epsl.2006.06.033
- Kueppers, U., B. Scheu, O. Spieler, and D.B. Dingwell (2006b), Fragmentation efficiency of explosive volcanic eruptions: A study of experimentally generated pyroclasts, *Journal of Volcanology and Geothermal Research*, 153(1-2), 125–135, doi:10.1016/j.jvolgeores.2005.08.006
- Kueppers, U., and F.B. Wadsworth (2015), What can pyroclastic deposits really tell us?, paper presented at the 26th IUGG conference, Prague, Czech Republic.
- Lame G., (1852), *Leçons sur la Théorie de l'Élasticité*, Gauthier-Villars, Paris.
- Lautze, N., J. Taddeucci, D. Andronico, B. Houghton, A. Niemeijer, and P. Scarlato, (2013), Insights into explosion dynamics and the production of ash at Stromboli from samples collected in real-time, October 2009, in Rose, W.I., Palma, J.L., Delgado Granados, H., and Varley, N., eds., *Understanding Open-Vent Volcanism and Related Hazards: Geological Society of America Special Paper 498*, p. 125–139, doi:10.1130/2013.2498(08)
- Mastin, L. G., M. Guffanti, R. Servranckx, P. Webley, S. Barsotti, K. Dean, A. Durant, J.W. Ewert, A. Neri, W.I. Rose, D. Schneider, L. Siebert, B. Stunder, G. Swanson, A. Tupper, A. Volentik, and C.F. Waythomas (2009), A multidisciplinary effort to assign realistic source parameters to models of volcanic ash-cloud transport and dispersion during eruptions, *Journal of Volcanology and Geothermal Research* 186, no. 1, 10-21.
- Mayer, K., B. Scheu, H.A. Gilg, M.J. Heap, B.M. Kennedy, Y. Lavallée, and D.B. Dingwell (2015), Experimental constraints on phreatic eruption processes at Whakaari (White Island volcano). *Journal of Volcanology and Geothermal Research*, 302, 150–162, doi:10.1016/j.jvolgeores.2015.06.014

- Matoza, R.S., D. Fee, T.B. Neilsen., K.L. Gee, and D.E. Ogden (2013), Aeroacoustics of volcanic jets: Acoustic power estimation and jet velocity dependence, *Journal of Geophysical Research: Solid Earth*, 118(12), 6269–6284, doi:10.1002/2013JB010303
- McNutt, S.R., and E.R. Williams (2010), Volcanic lightning: Global observations and constraints on source mechanisms, *Bulletin of Volcanology*, 72(10), 1153–1167, doi:10.1007/s00445-010-0393-4
- Méndez Harper, J., and J. Dufek (2016), The effects of dynamics on the triboelectrification of volcanic ash, *Journal of Geophysical Research: Atmospheres*, 121(14), 8209–8228, doi:10.1002/2015JD024275
- Métrich, N., A. Bertagnini, P. Landi, M. Rosi, and O. Belhadj (2005), Triggering mechanism at the origin of paroxysms at Stromboli (Aeolian Archipelago, Italy): The 5 April 2003 eruption, *Geophysical Research Letters*, 32(10), L10305, doi:10.1029/2004GL022257
- Montanaro, C., S. Scheu, K. Mayer, G. Orsi, R. Moretti, R. Isaia and D.B. Dingwell (2016), Experimental investigations on the explosivity of steam-driven eruptions: A case study of Solfatara volcano (Campi Flegrei), *Journal of Geophysical Research Solid Earth*, 121, 7996–8014, doi:10.1002/2016JB013273
- Ogden, D. (2011), Fluid dynamics in explosive volcanic vents and craters, *Earth and Planetary Science Letters*, 312(3-4), 401–410, doi:10.1016/j.epsl.2011.10.032
- Otsu, N. (1979), A threshold selection method from gray-level histograms, *IEEE transactions on systems, man, and cybernetics*, 9(1), 62-66.
- Peña Fernández, J.J., and Sesterhenn, J. (2017), Compressible starting jet: pinch-off and vortex ring–trailing jet interaction. *Journal of Fluid Mechanics*, 817, 560–589, doi:10.1017/jfm.2017.128
- Polacci, M., P. Papale, D. Del Seppia, D. Giordano, and C. Romano (2004), Dynamics of magma ascent and fragmentation in trachytic versus rhyolitic eruptions, *Journal of Volcanology and Geothermal Research*, 131(1–2), 93–108, doi:10.1016/S0377-0273(03)00319-6
- Saad, M. (1985), *Compressible fluid flow*. Prentice-Hall
- Saffaraval, F., S.A. Solovitz, D.E. Ogden, and L.G. Mastin (2012), Impact of reduced near-field entrainment of overpressured volcanic jets on plume development, *Journal of Geophysical Research*, 117(B5), B05209, doi:10.1029/2011JB008862
- Scharff, L., M. Hort, and N.R. Varley (2015), Pulsed Vulcanian explosions: A characterization of eruption dynamics using Doppler radar, *Geology*, 43(11), 995–998, doi:10.1130/G36705.1
- Scheu, B., U. Kueppers, S. Mueller, O. Spieler, and D.B. Dingwell (2008), Experimental volcanology on eruptive products of Unzen volcano. *Journal of Volcanology and Geothermal Research*, 175(1–2), 110–119, doi:10.1016/j.jvolgeores.2008.03.023
- Scheu, B., O. Spieler, and D.B. Dingwell (2006), Dynamics of explosive volcanism at Unzen volcano: an experimental contribution. *Bulletin of Volcanology*, 69(2), 175–187, doi:10.1007/s00445-006-0066-5
- Schmid, D., B. Scheu, F.B. Wadsworth, B.M. Kennedy, A. Jolly, and D.B. Dingwell (2017) A viscous-to-brittle transition in eruptions through clay suspensions, *Geophysical Research Letters*, 44(10), 4806–4813, doi:10.1002/2017GL073641

- Solovitz, S.A., D.E. Ogden, D.(D.-W.) Kim, and S.Y. Kim (2014), Coupled fluid and solid evolution in analogue volcanic vents, *Journal of Geophysical Research Solid Earth*, 119(7), 5342–5355, doi:10.1002/2014JB010993
- Sommerfeld, M. (1994). The structure of particle-laden, underexpanded free jets. *Shock Waves*, 3(4), 299–311, doi:10.1007/BF01415828
- Sparks, R.S.J. (2003), Forecasting volcanic eruptions, *Earth and Planetary Science Letters*, 210(1–2), 1–15, doi:10.1016/S0012-821X(03)00124-9
- Spina, L., C. Cimarelli, B. Scheu, D. Di Genova, and D.B. Dingwell (2016) On the slow decompressive response of volatile-and crystal-bearing magmas: An analogue experimental investigation, *Earth and Planetary Science Letters*, 433, 44-53, doi:10.1016/j.epsl.2015.10.029
- Stohl, A., A.J. Prata, S. Eckhardt, L. Clarisse, A. Durant, S. Henne, N.I. Kristiansen, A. Minikin, U. Schumann, P. Seibert, K. Stebel, H.E. Thomas, T. Thorsteinsson, K. Tørseth, and B. Weinzierl (2011) Determination of time- and height-resolved volcanic ash emissions and their use for quantitative ash dispersion modeling: the 2010 Eyjafjallajökull eruption, *Atmospheric Chemistry and Physics*, 11, 4333-4351, doi:10.5194/acp-11-4333-2011
- Taddeucci, J., M. Pompilio, and P. Scarlato (2002), Monitoring the explosive activity of the July-August 2001 eruption of Mt. Etna (Italy) by ash characterization, *Geophysical Research Letters*, 29(8), 71-1-71-4, doi:10.1029/2001GL014372
- Taddeucci, J., P. Scarlato, A. Capponi, E. Del Bello, C. Cimarelli, D.M. Palladino, and U. Kueppers (2012), High-speed imaging of Strombolian explosions: The ejection velocity of pyroclasts, *Geophysical Research Letters*, 39(2), doi:10.1029/2011GL050404
- Taddeucci, J., A. Capponi, P. Scarlato, D.M. Palladino, S. Cocomello and D., Gaudin (2013), The slug buster: an analogue experiment for the study of Strombolian explosions, paper presented at the IAVCEI Scientific Assembly 2013, Kagoshima, Japan.
- Taddeucci, J., J. Sesterhenn, P. Scarlato, K. Stampka, E. Del Bello, J.J. Pena Fernandez, and D. Gaudin (2014), High-speed imaging, acoustic features, and aeroacoustic computations of jet noise from Strombolian (and Vulcanian) explosions, *Geophysical Research Letters*, 41(9), 3096–3102, doi:10.1002/2014GL059925
- Taddeucci, J., M.A. Alatorre-Ibarguengoitia, D.M. Palladino, P. Scarlato, and C. Camaldo (2015), High-speed imaging of Strombolian eruptions: Gas-pyroclast dynamics in initial volcanic jets, *Geophysical Research Letters*, 42(15), 6253–6260, doi:10.1002/2015GL064874
- Taddeucci, J., M.A. Alatorre-Ibargüengoitia, O. Cruz-Vázquez, E. Del Bello, P. Scarlato, and T. Ricci (2017), In-flight dynamics of volcanic ballistic projectiles, *Reviews of Geophysics*, 55, doi:10.1002/2017RG000564
- Tournigand, P.Y., J.J. Peña Fernández, J. Taddeucci, D. Perugini and J. Sesterhenn (2017), Fractal analysis: A new tool in transient volcanic ash plume characterization, paper presented at the EGU 528 General Assembly 2017 conference, Vienna, Austria. Abstract number: Vol. 19, EGU2017-14643
- Tsuji, Y., Y. Morikawa, and H. Shiomi (1984), LDV measurements of an air-solid two-phase flow in a vertical pipe, *Journal of Fluid Mechanics*, 139, 417, doi:10.1017/S0022112084000422

- Tsuji, Y., Y. Morikawa, T. Tanaka, K. Karimine, and S. Nishida (1988), Measurement of an axisymmetric jet laden with coarse particles, *International Journal of Multiphase Flow*, 14(5), 565–574, doi:10.1016/0301-9322(88)90058-4
- Turner, N., B. Houghton, J. Taddeucci, J. von der Lieth, U. Kueppers, D. Gaudin, T. Ricci, K. 530 Kim, P. Scarlato (2017), Peering into Open Volcanic Vents, EOS
- Valentine, G.A. (1998), Eruption column dynamics, in *From Magma to Tephra*, edited by A. Freundt and M. Rosi, pp. 91-138, Elsevier, Amsterdam, Netherlands
- Van Eaton, A.R., Ál. Amigo, D. Bertin, L.G. Mastin, R.E. Giacosa, J. González, O. Valderrama, K. Fontijn, and S.A. Behnke (2016), Volcanic lightning and plume behavior reveal evolving hazards during the April 2015 eruption of Calbuco volcano, Chile, *Geophysical Research Letters*, 43, 3563–3571, doi:10.1002/2016GL068076
- Wadsworth, F.B., J. Vasseur, B. Scheu, J.E. Kendrick, Y. Lavallée, and D.B. Dingwell (2016), Universal scaling for fluid permeability during volcanic welding and sediment diagenesis. *Geology*, 44(3):219, doi:10.1130/G37559
- Wilson, L., R.S.J. Sparks, and G.P.L. Walker (1980), Explosive volcanic eruptions — IV. The control of magma properties and conduit geometry on eruption column behaviour, *Geophysical Journal of the Royal Astronomical Society*, 63:117–148, doi: 10.1111/j.1365-246X.1980.tb02613.x
- Wilson, L., and J.W. Head (1981), Ascent and eruption of basaltic magma on the Earth and Moon, *Journal of Geophysical Research*, 86(B4), 2971–3001, doi:10.1029/JB086iB04p02971
- Woods, A.W. (1988), The fluid dynamics and thermodynamics of eruption columns, *Bulletin of Volcanology*, 50(3), 169–193, doi:10.1007/BF01079681
- Woods, A.W. (1995), A model of vulcanian explosions, *Nuclear Engineering and Design*, 155(1–2), 345–357, doi:10.1016/0029-5493(94)00881-X
- Woods, A.W., and S.M. Bower (1995), The decompression of volcanic jets in a crater during explosive volcanic eruptions, *Earth and Planetary Science Letters*, 131(3–4), 189–205, doi:10.1016/0012-821x(95)00012-2
- Yin, S., M. Meyer, W. Li, H. Liao, and R. Lupoi (2016), Gas Flow, Particle Acceleration, and Heat Transfer in Cold Spray: A review. *Journal of Thermal Spray Technology*, 25(5), 874–896, doi:10.1007/s11666-016-0406-8
- Zimanowski, B., R., Büttner, P., Dellino, White, J.D.L., and K.H. Wohletz (2015), Magma-water interaction and phreatomagmatic fragmentation. *The encyclopedia of volcanoes – 2nd edition*, edited by H. Sigurdsson et al., pp. 257- 264, Elsevier

Valeria Cigala

Home address: Mariahilfstr. 20 81541 Munich DE

Email: valeria.cigala@min.uni-muenchen.de

Date and place of birth: 03.11.1989, Gallarate IT

Education

- **June 2014 – ongoing** Marie Curie research fellow / PhD candidate. Ludwig-Maximilians-Universität (LMU) Munich, DE.
- **2011 - 2014.** Master of Science, INVOGE - International Masters in Volcanology and Geotechniques. Double Master degree from *Università degli Studi Milano-Bicocca* (IT) and Michigan Technological University (USA).
- **June 2013 – September 2013.** *Université Blaise-Pascal*, Clermont-Ferrand, France. Erasmus.
- **2008 - 2011.** Bachelor degree, *Università degli Studi Milano-Bicocca*, Milano, Italy. Geology and Earth Science.
- **2003 – 2008.** Scientific High School, *Liceo scientifico “Leonardo Da Vinci”*, Gallarate, VA, Italy.

Work Experience

- **From June 2014:** Marie Curie research fellow, PhD candidate, LMU Munich, DE
- **October 2015 – February 2016,** Teaching assistant, exercises course of Geowissenschaften I - Geomaterialien (Geosciences I – Geo-materials) at LMU
- **April 2010 – March 2014,** Marketing agencies, Varese and Milan, IT; promoter for H-Tech products, water purification systems and food & beverage in non-continuous way while studying at university.
- **October 2008 - December 2008,** “*L'orso e il miele*” restaurant, Oggiona, Va, IT; waitress.

Munich, 11.09.2017

Valeria Cigala



LUDWIG-
MAXIMILIANS-
UNIVERSITÄT
MÜNCHEN

FORMBLATT 3
FAKULTÄT FÜR GEOWISSENSCHAFTEN



Eidesstattliche Versicherung

Ich versichere hiermit an Eides statt, dass die Dissertation von mir selbstständig und ohne Beihilfe angefertigt worden ist.

(Ort, Datum)

(Unterschrift des Doktoranden / der Doktorandin)

Erklärung

Hiermit erkläre ich, dass die Dissertation, ganz oder in Teilen, noch keiner anderen Promotionskommission vorgelegt worden ist.

(Ort, Datum)

(Unterschrift des Doktoranden / der Doktorandin)

Erklärung

Hiermit erkläre ich, dass ich mich anderweitig einer Doktorprüfung ohne Erfolg **nicht** unterzogen habe.

(Ort, Datum)

(Unterschrift des Doktoranden / der Doktorandin)